

POLITECNICO DI MILANO
Scuola di Ingegneria Industriale e dell'Informazione
Corso di Laurea Magistrale in Ingegneria Biomedica



Endovascular Abdominal Aneurysm Repair outcomes: image-based analysis of stent-graft displacements and computational fluid-dynamics

Relatore:

Prof. Christian VERGARA (MOX - Dipartimento di Matematica)

Correlatore:

Dr. Maurizio DOMANIN (Divisione di Chirurgia Vascolare Ospedale
Ca' Granda Policlinico di Milano)

Ing. Simone STELLA (MOX - Dipartimento di Matematica)

Tesi di Laurea di:

Giulia PIAZZOLI Matr. 874633

Anno Accademico 2017-2018

Contents

Abstract	II
Sommario	IV
1 Clinical problem and aims of the work	1
1.1 Anatomy and physiology of the aorta	1
1.2 Histology of the abdominal aorta	4
1.3 Abdominal Aortic Aneurysm	6
1.4 Surgical treatment of the abdominal aortic aneurysm	8
1.4.1 Open abdominal aortic aneurysm repair	8
1.4.2 Endovascular aneurysm repair	9
1.5 Possible stent-graft phenomenology after surgery	10
1.6 Aims of the work	13
2 Medical image processing	17
2.1 Dataset	17
2.1.1 Clinical cases	17
2.1.2 Type of images	18
2.2 3D geometric analysis: Stent-grafts segmentation	20
2.2.1 Vmtk	22
2.3 Computation of stent-grafts displacements	28
2.3.1 Computation of stent-graft displacements over cardiac cycle	28
2.3.2 Computation of stent-grafts displacements among follow-ups	28
3 Geometric analysis results	31
3.1 Configurations of the segmented stent-grafts	31
3.1.1 Patient I	31
3.1.2 Patient II	35
3.1.3 Patient III	37
3.2 Displacements over cardiac cycle	38
3.2.1 Patient I	39
3.2.2 Patient II and Patient III	42
3.3 Displacements between follow-ups	45
3.3.1 Patient I	45
3.3.2 Patient II	48
3.3.3 Patient III	50

4	Mathematical and numerical methods	55
4.1	Models for blood	55
4.2	The Navier-Stokes equations	57
4.3	The weak formulation	60
4.4	Numerical approximation	63
4.4.1	Space discretization by means of Finite Elements Method	63
4.5	Time discretization	65
4.6	The SUPG-PSPG stabilization	66
5	Results of the numerical simulations	69
5.1	Computational domain	69
5.1.1	Lumen extraction	70
5.1.2	Mesh generation	72
5.2	LifeV	74
5.3	Details on the numerical experiments	75
5.3.1	Boundary conditions	75
5.3.2	Simulation parameters	77
5.4	Description of blood dynamics for each patient and case	78
5.4.1	Patient I	78
5.4.2	Patient III	86
6	Relationships between blood dynamics and stent displacements	91
6.1	Patient I	91
6.1.1	WSS-Displacements within the cardiac-cycle	91
6.1.2	TAWSS-Displacements between follow-ups	94
6.2	Patient III	98
	Bibliography	109

Abstract

Background and purpose: Endovascular abdominal aneurysm repair (EVAR) is an effective alternative to conventional open repair for the treatment of abdominal aortic aneurysm (AAA). EVAR has less traumatic effects when compared with conventional surgery repair due to its minimally invasive nature. Although this technique has been shown to be successful on the short term, several post-operative complications are reported after some months, such as graft migration, endoleak, thrombus formation or device failure. The purpose of this thesis is to investigate the clinical outcomes of EVAR by quantitatively assessing the stent-graft displacements both within cardiac cycle and among several follow-ups for three different patients: Patient I, Patient II and Patient III. Moreover we try to investigate a possible relation of such displacements with the hemodynamic variables obtained by CFD simulations.

Materials and methods: The computed tomography (CT) scans of three patients who underwent EVAR was obtained during follow-up examinations thanks to the collaboration with Fondazione IRCSS Ca' Granda, Ospedale Maggiore Policlinico (Milan). For each of the follow-up ten ECG gated series were acquired at every 10 % of the R-R interval allowing the retrieval of dynamic imaging of the aorta during a complete systolic-diastolic cycle. In order to analyse the displacements, stent-graft segmentations were performed using the image processing and reconstruction software VMTK (Vascular Model Toolkit). Once the 3D stent-graft surfaces were registered by means of the ICP algorithm, we quantitatively evaluate the movements of the devices both throughout the cardiac cycle and among follow-ups. Fluid-dynamics simulations based on the Finite Elements Method (FEM) were performed with the patient-specific geometries of the endograft lumen for two patients and for each of their follow-up. Blood was considered as Newtonian, homogeneous and incompressible fluid, so that the Navier-Stokes equations were used for its mathematical description. Given the overall rigid structure of the endograft, we adopted the assumption of rigid walls. Qualitative and quantitative changes in velocity fields, wall shear stress (WSS) and time averaged wall shear stress (TAWSS) among follow-ups were analyzed, as well as the presence of disturbed flow patterns.

Results: Stent-grafts have been successfully segmented for all the three patients, however only Patient I CT images had sufficiently high contrast resolution such that an

effective analysis of the displacements within the cardiac cycle was performed. Patient I stent-graft experienced a lateral rigid translation of the whole structure during systolic-diastolic interval, specifically towards the right. Analysis of the movements among follow-ups was effective for all of the three clinical cases at our disposal. In particular, it was noticed a specific configuration of the endograft motion of Patient I, that is the dilation of the metal wires at the level of the bifurcation of the iliac legs, on the right side, where conformation initially looked like a stenotic vessel. In case of Patient II, endograft migration involved: the distal ends of iliac legs, the top and the bifurcation regions. Analysis of Patient III post-EVAR outcomes revealed a progressive significant expansion of the central portion of the device over the years.

Hemodynamic simulation results on Patient I endograft lumen highlighted a peak of WSS and TAWSS at the level of the stenotic right leg in all the follow-ups. Furthermore, blood flow analysis showed the occurrence of recirculation and helical structures, specially along the left leg. Finally, through the post-processing evaluation of Patient III fluid-dynamics, a highly disturbed flow pattern at the central portion of the device was observed, where the stent-graft angulation is present. In this region recirculation and vortices formation increase over the years.

Conclusions: In view of the above, by merging the displacements analysis and the fluid-dynamic results, we found that the lateral rigid translation towards the right of the Patient I device during the cardiac cycle is coherent with the high WSS values computed at the stenosis of the right leg. WSS in such portion seems to act as a driving force of the whole migration. In case of Patient III, the huge expansion of the central portion was correlated to the complex recirculation patterns occurring at the same level of the device, which probably could lead to a thrombus formation, causing the metal wire dilation.

In conclusion, this study is a preliminary study on a possible correlation between the stent-graft displacements and fluid-dynamic indices. Of course, more cases and analysis will be mandatory to support our thesis. These findings highlight the importance of the geometric features of the stent-graft which highly influence the hemodynamics and may play a role in research and clinical environments to support planning of EVAR.

Sommario

Introduzione e obiettivo: La riparazione endovascolare dell'aneurisma (EVAR) è un metodo efficace alternativo alla procedura convenzionale a cielo aperto per il trattamento dell'aneurisma dell'aorta addominale (AAA). Tale procedura è meno traumatica in confronto alla chirurgia convenzionale per via della sua natura minimamente invasiva. Sebbene tale tecnica si sia dimostrata efficace nel breve periodo, si annoverano numerosi casi di complicanze a partire da alcuni mesi successivi all'operazione, come ad esempio la migrazione della protesi, endoleak, formazione di trombo o addirittura il fallimento del dispositivo. L'obiettivo di questa tesi consiste nell'investigare gli esiti clinici dell'EVAR valutando gli spostamenti che subisce lo stent-graft sia durante il ciclo cardiaco che tra i diversi follow-up a cui sono stati sottoposti tre pazienti: Paziente I, Paziente II and Paziente III. Inoltre, proveremo ad indagare l'esistenza di una possibile relazione che intercorre tra gli spostamento ed i risultati emodinamici ottenuti dalle simulazioni CFD.

Materiali e metodi: Grazie alla collaborazione con Fondazione IRCSS Ca' Granda, Ospedale Maggiore Policlinico (Milano), sono state ottenute delle scansioni radiologiche tramite Tomografia Computerizzata (CT) durante gli esami di follow-up di tre pazienti precedentemente sottoposti all'EVAR. Per ognuno dei follow-up si sono acquisite 10 scansioni ECG gated (scansioni sincronizzata con il tracciato ECG) ad ogni 10 % dell'intervallo R-R consentendo la rilevazione di immagini dinamiche dell'aorta durante un ciclo completo sistole-diastole. Al fine di analizzare gli spostamenti, sono state eseguite le segmentazioni degli stent-graft usando il software VMTK (Vascular Model Toolkit) atto al processamento delle immagini e alla loro ricostruzione. Dopo aver registrato le superfici 3D in un unico sistema di riferimento, abbiamo valutato quantitativamente i movimenti dei dispositivi sia durante il ciclo cardiaco che tra un follow-up e l'altro. Si sono effettuate delle simulazioni fluido-dinamiche per due dei tre pazienti coinvolti nello studio e per ciascuno dei follow-up a cui i pazienti si sono sottoposti. Le simulazioni numeriche sono basate sul metodo agli elementi finiti (FEM) e poichè il sangue è stato considerato come un fluido newtoniano, omogeneo e incompressibile, per la sua descrizione matematica sono state usate le equazioni di Navier-Stokes. Data la complessiva rigidità dell'endograft, si è scelto di considerare le pareti come rigide. Si sono analizzati i cambiamenti qualitativi e quantitativi tra i vari follow-ups di ciascun

paziente valutando i campi di velocità, il wall shear stress (WSS) ed il wall shear stress mediato nel tempo (TAWSS), come anche la presenza di pattern disturbati del flusso.

Risultati: La segmentazione degli stent è stata effettuata con successo per tutti i pazienti, ma solo le immagini CT relative al Paziente I presentavano una qualità di risoluzione tale da permettere una valida analisi degli spostamenti all'interno del ciclo cardiaco. Si è visto che l'intera struttura dello stent-graft del caso del Paziente I sperimenta una traslazione rigida all'interno del periodo sistolico-diastolico, specialmente verso destra. L'analisi degli spostamenti avvenuti tra i vari follow-up è stata possibile per tutti e tre i pazienti studiati. In particolare, è stata notata una specifica configurazione del movimento dello stent del Paziente I, che consisteva in una dilatazione delle maglie metalliche al livello della biforcazione dei rami iliaci, dal lato destro, dove la conformazione inizialmente ricordava un vaso stenotico. Nel caso del Paziente II, la migrazione dell'endograf coinvolgeva: le regioni distali dei rami iliaci, la parte più prossimale in alto e la regione centrale. L'analisi degli esiti clinici post-operatori sul Paziente III ha rivelato una progressiva ed importante espansione della porzione centrale del dispositivo nel corso degli anni.

I risultati ottenuti dalle simulazioni emodinamiche sul lumen dell'endograf del Paziente I hanno evidenziato un picco nei valori del WSS and del TAWSS al livello della stenosi del ramo destro, in tutti i follow-up. Inoltre, l'analisi sul flusso ha mostrato l'insorgenza di ricircoli e strutture elicoidali, specialmente lungo il ramo sinistro. Infine, attraverso il post-processing della fluido-dinamica del Paziente III, si è osservato un flusso altamente disturbato nella zona centrale del dispositivo, dove si verifica la curvatura dello stent. In questa zona la formazione di ricircoli e vortici addirittura aumenta nel corso degli anni.

Conclusioni: Alla luce di quanto esposto, unendo l'analisi sugli spostamenti ed i risultati fluido-dinamici, si è riscontrato che la rigida traslazione laterale verso destra dell'endograf del Paziente I, durante il ciclo cardiaco, è coerente con gli alti valori di WSS registrati sulla stenosi del ramo destro. Sembrerebbe, quindi, che il WSS agente in questo punto agisca come forza motrice dello spostamento complessivo dello stent. Nel caso del Paziente III, l'ingente espansione della porzione centrale è stata correlata al verificarsi di numerosi ricircoli e vortici proprio nella medesima zona che probabilmente potrebbero aver dato inizio alla formazione di un trombo, causa della citata dilatazione.

In conclusione, questo è uno studio preliminare su una possibile correlazione tra gli spostamenti dello stent-graft e gli indici fluido-dinamici al fine di valutare in toto gli esiti di tre casi clinici sottoposti a EVAR. Di certo sono necessari ulteriori casi ed analisi per supportare la nostra tesi. I risultati a cui si è pervenuti evidenziano l'importanza delle caratteristiche geometriche degli stent-graft che ne influenzano significativamente l'emodinamica.

Chapter 1

Clinical problem and aims of the work

1.1 Anatomy and physiology of the aorta

The aorta, see Figure 1.1, is the largest artery of the human body which arises from the left ventricle of the heart, it ascends to become the aortic arch, it extends down in the abdomen and ends, diminished in size, by bifurcating into right and left common iliac arteries. The aorta transfers the oxygenated blood to all the tissues of the body for their nutrition through the systemic circulation. In addition to the conduit function, the aorta plays also a role in the control of systemic vascular resistance and heart rate, thanks to the pressure-responsive receptors located in its ascending tract and in the arch: if the aortic pressure increases, the heart rate and systemic vascular resistance decrease, while a decrease in the aortic pressure results in an increase in the heart rate and systemic vascular resistance.

The size depends on several factors including age, gender, height, weight, body surface area and blood pressure, but generally it reaches a diameter of 3 cm at the very beginning at the level of the aortic root while it is considerably smaller at the iliac bifurcation where it is about 1.75 cm in diameter. The aortic wall is capable of remodelling in response to hemodynamic, mechanical, and various biochemical stimuli. In anatomical sources, the aorta is subdivided into several sections. as Figure 1.2 shows:

- aortic root
- ascending aorta
- aortic arch
- descending thoracic aorta
- abdominal aorta



Figure 1.1: Graphic depiction of the aorta.

Aortic root: originates from the aortic valve annulus and extends to the sinotubular junction, i.e. the point where the aorta becomes a tubular structure. It consists of three round dilations called sinuses of Valsalva from where the right and left coronary arteries arise.

Ascending aorta: it is the segment between the sinotubular junction and the largest aortic branch vessel named brachiocephalic (or innominate) artery. The ascending aorta is contained within the pericardium, and is enclosed in a tube of the serous pericardium, common to it and the pulmonary artery. The ascending aorta measures approximately 5 cm in lengths and 2.6 cm in diameter.

Aortic arch: It is the portion of the aorta between the brachiocephalic artery and the left subclavian artery ostium, As Figure 1.2 shows, in addition to and between the two mentioned branches, also the left carotid arises from the aortic arch. The brachiocephalic artery supplies with oxygenated blood the right side of the head, the neck as well as the right arm and the chest wall. The left carotid artery carried blood to the left side of the head and brain. The last branch vessel, the left subclavian artery, supplies the left arm with blood.

Descending thoracic aorta: It is located in the thorax and begins at the level of the last branch vessel of the aortic arch, it descends in the posterior mediastinum initially on

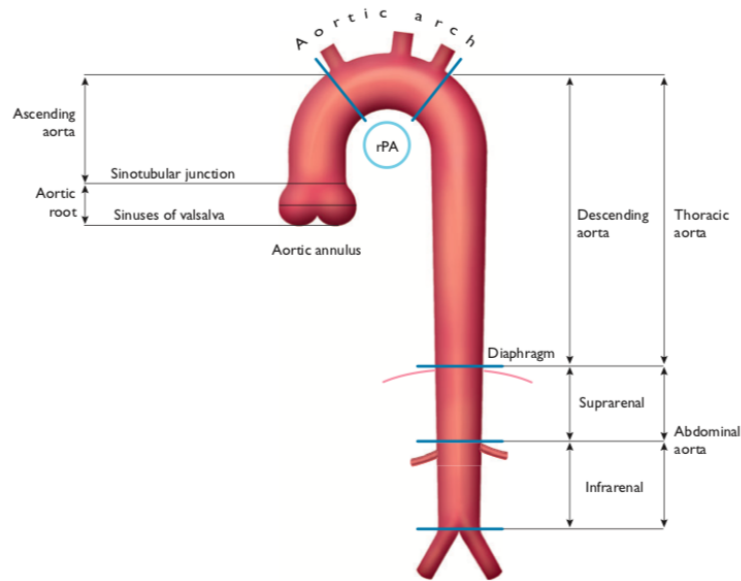


Figure 1.2: Segmental division of the aorta: aortic root, ascending aorta, aortic arch, descending thoracic aorta and abdominal aorta.

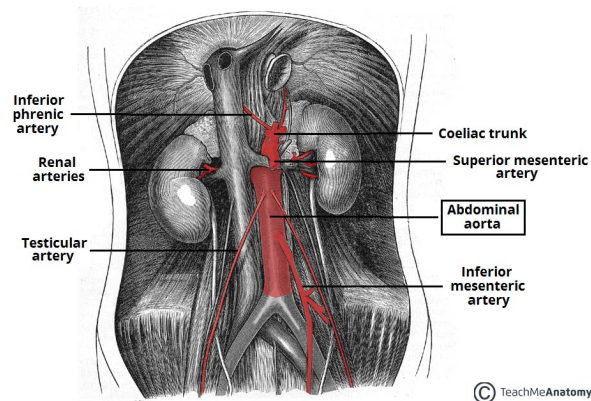


Figure 1.3: The anatomy of the human aorta.

the left of the thoracic vertebral bodies and ends at the aortic hiatus in the diaphragm where it becomes the abdominal aorta, at the level of the twelfth thoracic vertebra. It has six paired branches: bronchial arteries, mediastinal arteries, esophageal arteries, pericardial arteries, superior phrenic artery and intercostal arteries. The right branches are longer than the left ones since the descending aorta is on the left side of the vertebrae. It supplies blood to the esophagus, lungs and the chest area including the ribs and the mammary glands. The diameter of this section of the aorta ranges from about 3 cm at the proximal level to about 2.3 cm at the distal part, at the eleventh rib level.

Abdominal aorta: The abdominal aorta, see Figure 1.3(a), begins at the aortic hiatus of the diaphragm and ends in a bifurcation into the left and right common iliac arteries. From the diaphragm it descends vertically downward and to the left, in front of the

vertebral column, and ends in front of the lower part of the body of the fourth lumbar vertebra to the left of the median plane. It has a convex forward curve and the summit of its convexity corresponds to the third lumbar vertebra. The abdominal aorta supplies the following branches: three anterior unpaired branches to viscera (celiac trunk, superior mesenteric artery, inferior mesenteric artery), three lateral paired branches to viscera (suprarenal artery, renal artery, testicular/ovarian artery), five lateral paired branches to parities (inferior phrenic artery and four lumbar arteries) and three terminal branches (right common iliac artery, median sacral artery and left common iliac artery). Figure 1.4 graphically shows the subdivisions of the abdominal aorta. The size keeps diminishing rapidly due to the presence of many large branches and generally the diameter ranges from about 2 cm to less than 2 cm.

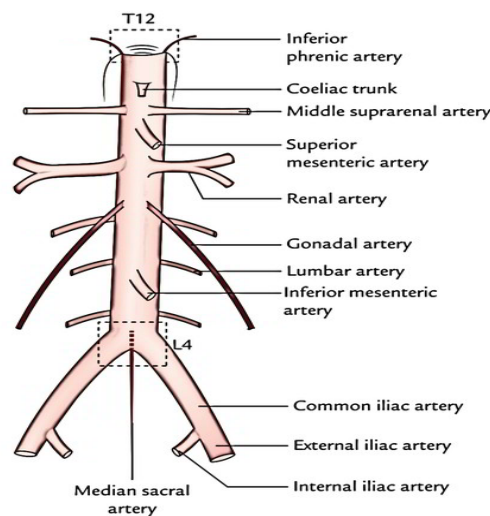


Figure 1.4: Scheme of the branches of the abdominal aorta.

1.2 Histology of the abdominal aorta

The vessel wall of the abdominal aorta consists of three layers: the intima, the media and the adventitia, see Figure 1.5.

Intima: The intima is the innermost tunic and it is directly in contact with blood. It consists of a single layer of endothelial cells embedded in extracellular matrix and supported by subendothelial layer of connective tissue and supportive cells, called basal lamina. The tunica intima plays important roles such as the maintenance of vascular tone, the formation of growth regulatory molecules, the maintenance of connective tissue matrix and it provides a non-thrombogenic surface to the blood flowing through the vessel. The intima is very thin since its thickness measures from 0.05 to 0.1 mm while

in pathological cases from 0.2 to 0.4 mm, becoming stiffer and heterogeneous. Damage to the endothelial cells initiates a chain of pathological processes with atherosclerosis and aneurism formation as final outcomes. An internal elastic membrane separates the tunica intima from the tunica media.

The tunica media: The tunica media is made of elastic fibers, collagen fibers and vascular muscle cells immersed in a matrix containing proteoglycans. The structural fibers are organized in a specific pattern: the vascular muscle cells are oriented circumferentially in concentric layers surrounded by the collagen fibers and separated by sheets of matrix containing the elastic fibers. This laminated and concentric structure provides to the media high strength and determines the mechanical properties of the whole aorta wall: the ability to carry loads in circumferential direction. The elastic fibers are highly elastic over extreme extensions providing the abdominal aorta with extensibility, elastic recoil and resilience. They also allow the origin of the residual stress and axial pre-stress, important for maintenance of arterial homeostasis. The tunica media is the thickest layer of the artery, i.e. from 0.1 to 0.5 mm. The media is separated from the adventitia by an external elastic lamella.

Adventitia: The tunica adventitia is the outermost component of the arterial wall.

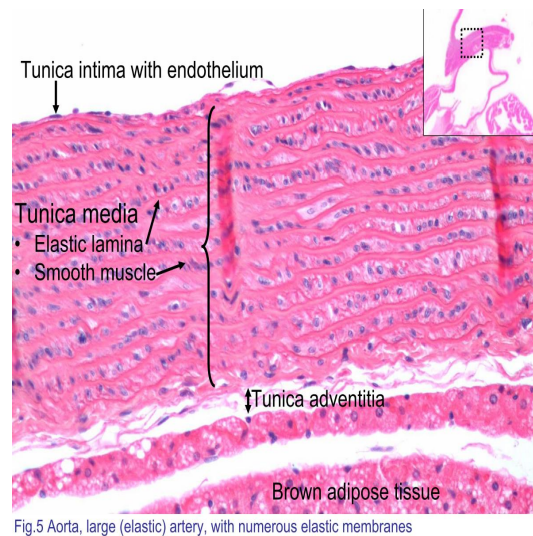


Fig.5 Aorta, large (elastic) artery, with numerous elastic membranes

Figure 1.5: Histologic section of the aorta showing the three layers: tunica intima, media and adventitia.

It consists of a network of collagen fibers, nerves, elastic fibers, fibroblasts and vasa vasorum. Collagen is distributed throughout all three layers of the abdominal aorta wall, but most in the adventitia. The collagen types in the abdominal aorta are type I and III, both of which are fibrillar collagens. The collagen fibers tend to be oriented axially and they straighten when the pressure increases to provide strength to the wall and prevent over-dilation in case of overloading, due to their high stiffness and low extension. The

thickness of the adventitia ranges from 0.25 to 0.40 mm.

1.3 Abdominal Aortic Aneurysm

Cardiovascular diseases cause more than half of all deaths across the European Region and they are the number one cause of death globally. Some of the most frequent cardiovascular pathologies occur to the aorta, such as aortic aneurysms, acute aortic syndromes including aortic dissection, intramural haematoma, penetrating atherosclerotic ulcer and traumatic aortic injury, pseudoaneurysms, aortic rupture, atherosclerotic and inflammatory affections, as well as genetic diseases and congenital abnormalities including the coarctation of the aorta.

Aneurysm is the second most frequent disease of the aorta after atherosclerosis. The

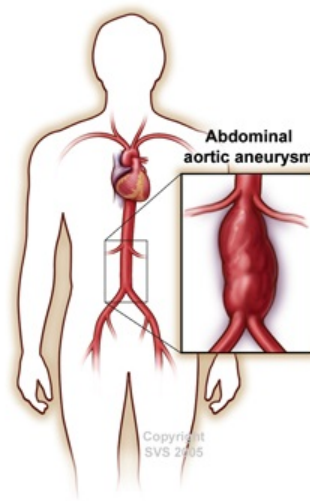


Figure 1.6: An example of AAA.

types of aortic aneurysms can be classified as Abdominal Aortic Aneurysm (AAA), see Figure 1.6, located in the abdominal part of the aorta, and Thoracic Aortic Aneurysm (TAA) located in the region of the thoracic aorta. In this work we concentrate on the first type of aneurysm, i.e. the AAA.

An aneurysm is generally defined as arterial enlargement with loss of arterial wall parallelism. More specifically, it is defined as a diameter greater than 30 mm. An alternative definition is the dilatation of an artery having at least a 50% increase in diameter compared with the expected normal diameter of the artery in question. Dilation, and eventually rupture, occur when an inflammation and proteolytic degeneration of

connective tissue proteins take place, leading to the loss of structural integrity of the aortic wall and, as a result, to the widening of the vessel.

AAAs are often asymptomatic and therefore detected accidentally. Symptomatic AAAs manifest with lower back pain, a painful pulsatile abdominal mass and hypovolemic shock. Risks factors associated with the AAA are: age, male gender, personal history of atherosclerotic cardiovascular disease, smoking and hypertension. The prevalence of AAA is around 3% in the population above 50 years and the incidence increases with ageing.

The pathogenesis of this syndrome is not completely understood and still debated, since it is a complex disease with genetic, biological and environmental factors. Aneurysms of the abdominal aorta are a particular form of atherothrombosis, whose pathogenesis is based on the role of proteases, including matrix metalloproteinases and serine proteases. The difference between AAA and the occlusive form of atherothrombosis consists, in the case of the aneurysm, in the localization in the aortic media, the presence of a chronic intraluminal thrombus (ILT) and the association with a significant adventitial reaction. The production of proteases by resident vascular wall cells (medial smooth muscle cells and adventitial fibroblasts) causes the fragmentation of the elastic fibres and a decreased concentration of elastin. In the degradation or absence of the media elastin, the collagen of the tunica adventitia is responsible for the resistance of the aorta and some researchers [1] affirm that the collagen degradation is the ultimate cause of rupture. The elastin degradation fragments and proinflammatory cytokines, chemokines and prostaglandin derivatives (produced by the resident mesenchymal cells and the inflammatory cells) promote the recruitment of leucocytes into the aortic wall. The immunoinflammatory response has been suggested to play a role in the development of AAA, due to the adventitia reaction to the centrifugal insults by accumulating macrophages in the inner part, originating a fibroblastic reaction [2].

A crucial feature of AAAs is the presence of a chronic intraluminal thrombus (ILT), see Figure 1.7: a biologically active neo-tissue described as a laminated structure, containing several layers of fibrin clot. The luminal layer, the most recent, is highly biologically active characterized by trapped red blood cells and fibrin formation after the platelet and thrombin activation. ILT determines a lower density of vascular smooth muscle cells in the media and an increase in the adventitia inflammation. This phenomenon tells us that an important part of the protease activity originates from the ILT, rather than being directly generated within the AAA wall. The role of the intraluminal thrombus in the aneurysmal development and rupture is still controversial, but it surely affects the AAA wall strength and stress. Zambrano [3] in his work shows that aneurysms with ILT record lower values of wall shear stress and higher values of diameter expansions than those AAAs free of thrombus. Although the thrombus can reduce aneurysmal wall

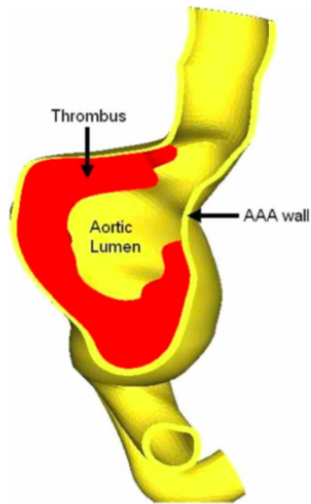


Figure 1.7: The figure shows a schematic overview of an Intraluminal Thrombus (ILT).

stress, its increasing thickness leads to local hypoxia at the inner layer of the media, which can induce increased medial neovascularisation and inflammation. The idea of the cited author is that by increasing wall shear stress levels thrombus accumulation inside AAA can be avoided.

1.4 Surgical treatment of the abdominal aortic aneurysm

The treatment of AAAs is based on the balance between risk of rupture and risk of intervention. The risk of rupture is primarily determined by analysing morphological data such as diameter and growth rate. Generally females are considered for intervention from an increase in diameter of 5 cm and males from 5.5 cm (tend to suffer AAA rupture at a smaller aortic diameter than men), unless other signs of rapid growth or particular collagen disease exist. Some researchers suggested more mechanical risk of rupture indexes, such as Vorp et al [4] the ratio of wall strength to wall stress, or Kleinstreuer et al [5] a parameter based on eight biomechanical factors (including expansion rate, stress ratio, asymmetry index) with associated weighting but the clinical gold standard remains the evaluation of a threshold diameter.

1.4.1 Open abdominal aortic aneurysm repair

The current standard surgical treatment of an aortic aneurysm is the open-chest approach, shown in Figure 1.8, since its first use by Dubost in the early 1950s. It carried a certain

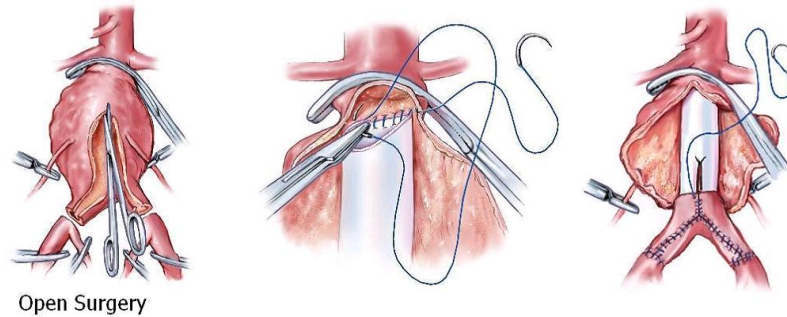


Figure 1.8: Open aortic aneurysm repair procedure.

risk of mortality that varies from 1% to 8% across centres and countries. The AAA is accessed through an incision in the abdomen of the patient and after the aorta has been exposed, the surgeon cuts the aorta close to the aneurysm and replace the weakened portion of vessel by inserting a fabric tube, called graft, made of a knitted synthetic material sealed with collagen or albumin. The artificial aorta forms a new blood vessel inside the aneurysm sac. The aneurysm sac is sewn around the graft to protect surrounding organs. Although open repair is considered the standard treatment, it is associated with some problems, such as the traumatic experience for the body that requires a long recovery period in addition to the fact that this surgery is not feasible for all patients. Specific morbidities linked to open repair are left colon ischaemia, renal failure (eventually due to thrombo-embolic events in renal arteries), postoperative paraplegia.

1.4.2 Endovascular aneurysm repair

Endovascular aneurysm repair for abdominal was introduced by Parodi in 1991 and consists in a surgery performed inside the aorta using thin long tubes called catheters, used to guide and deliver a Stent-Graft through the femoral artery to the site of the aneurysm, as shown in Figure 1.9. The deployment of the endograft is carried out in a sterile environment under x-ray fluoroscopic guidance. The stent-graft, once positioned, resumes its natural configuration either by ballooning or due to a self-expandable construction material. Its purpose is to exclude the aneurysm sac from the main stream circulation by carried the hemodynamic load and prevents rupture. Excellent results are characterised by a perfectly canalised blood flow and later by a completely retracted aneurysm wall around the endograft. A stent-graft is a fabric tube supported by metal wired struts. It consists in three parts: the main body and two extensions, one for each iliac artery.

EVAR is now widely accepted, owing to its superior short-term results, the lower

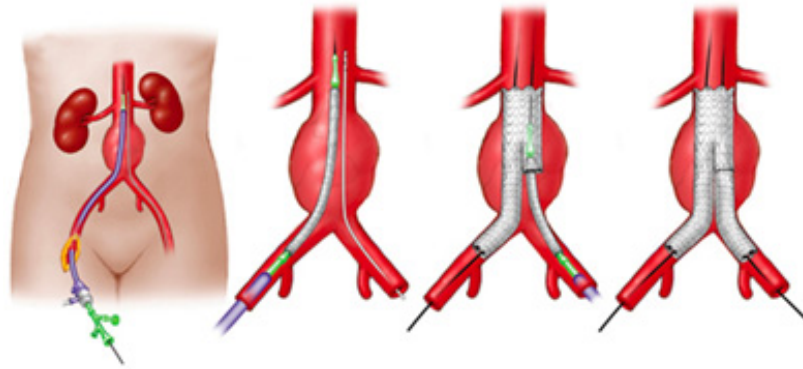


Figure 1.9: Endovascular aneurysm repair procedure.

post-operative morbidity and mortality, lower pain and risk of complications, shorter convalescence time, compared with the conventional open surgery. On the other hand, some patients result unsuitable for EVAR in case they present more complex aortic anatomy, including those aneurysms in close proximity to or involving the renal arteries. For these patients the open repair remains the standard but advanced treatment strategies exist to face address such types of aneurysms, for instance branched or fenestrated endografts that are increasingly being used besides their outcomes may lead to severe postoperative complications, including spinal and mesenteric ischaemia and renal complications.

1.5 Possible stent-graft phenomenology after surgery

In the previous paragraph we mentioned the early benefits of EVAR as compared with standard surgical repair, including less blood loss, shorter procedure times, reduced length of hospital stay, lower rates of major adverse events and dramatically quicker recovery. However, there is a lack of information on mid- and long-term results. Recent works [6], [7] investigated the long-term benefit of EVAR compared with open repair and found that endovascular repair was associated with early case survival advantage that gradually decreased over time and then definitely lost. These results suggest that specific postoperative surveillance and follow-ups are extremely important to detect and investigate the possible adverse events of EVAR, both for patient health and for stent-graft future improvement.

Possible complications after EVAR are endoleak, migration and conformational alterations, associated with secondary aortic sac rupture with high risk of death.

Endoleak

Endoleaks occur when blood leaks back into an aneurysm sac after an endovascular aneurysm repair. There are five types of endoleaks (Figure 1.10):

- type I occurs when there is a gap between the graft and the vessel wall allowing blood to flow along the side of the graft into the aneurysm sac. This creates pressure within the sac and increases the risk of sac rupture. Type I endoleak occurs when the aneurysm is unsuitable for EVAR or if the device has been inappropriately selected. It is usually treated with an endovascular procedure to adjust stent-graft placement.
- type II endoleak is the most common one and occurs when increased pressure within

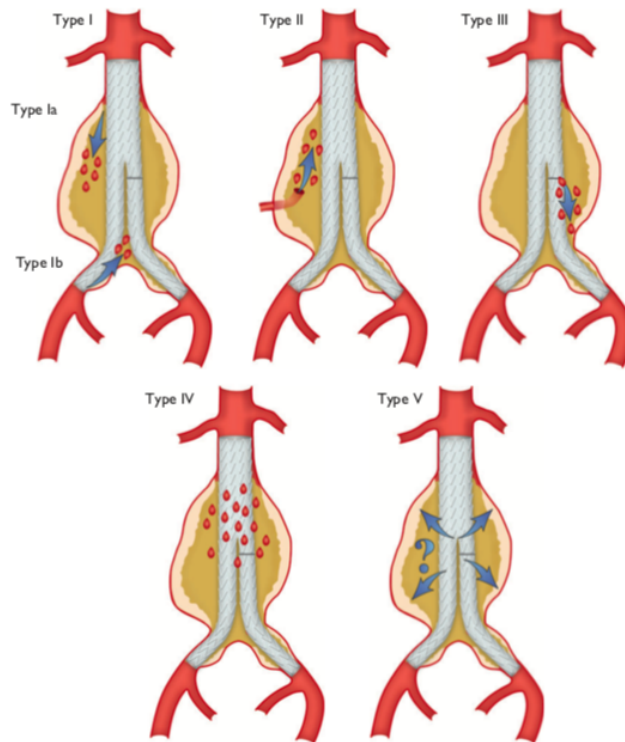


Figure 1.10: In the picture the five types of endoleaks are graphically depicted.

the side branches of the aorta forces blood to leak back into the aneurysm sac, where the pressure is lower. There are several treatment approaches for this kind of endoleak but the most common one is a translumbar embolization: the aneurysm sac is punctured with a needle and clot-inducing materials, for instance coils or glues, are injected.

- type III results from a defect or misalignment between the components of endografts. Like in the case of type I, it causes systemic pressure within the aneurysm sac that increases the risk of sac rupture. To re-line the endograft and seal the defect, additional components are inserted.
- type IV endoleak occurs soon after EVAR procedures due to the porosity of certain graft materials. This problem solves itself once blood clotting has normalized, so that

no additional procedures are needed.

- type V endoleak, also called endotension, is a not well understood phenomenon and it is thought to occur when increased graft permeability allows pressure to be transmitted through the aneurysm sac, affecting the native aortic wall. The treatment for this kind of endoleak is still debated, but endograft reinforcement procedures have been demonstrated to have promising results.

Migration

Graft migration is the movement of the stent-graft from its initial deployment site and it has been defined as movement greater than 5 mm. This is a possible complication since the stent-graft is not attached to the native aorta with any sutures. Late migration of stent-grafts is the main reason for the post-operative re-intervention since it is responsible for a large part of the late complications after EVAR, including late stent graft related endoleaks that result in aneurysm sac enlargement, and even rupture. Several researchers focused on the mechanisms leading to graft migration and reported that pulsatile forces of blood flow, referred to as migration forces, displacements forces or drag forces, are responsible for the longitudinal movement of the stent graft [8], [9], [10]. In addition to the analysis of the longitudinal migration, also the graft movement in all three spatial directions was explored [11]. The drag force magnitude is determined by parameters such as the neck diameter, neck angulation, iliac angulation, pressure waveform and neck-iliac diameter ratio. In the European Collaborators on Stent Graft Techniques for Aortic Aneurysm Repair (EUROSTAR) database, the investigators evaluated the influence of infrarenal neck angulation on clinical outcomes after EVAR. As a result, the early proximal stent-graft migration was significantly more common in patients with severe infrarenal aortic neck angulation. Spanos et al [12] investigated the relationship between migration and AAA diameter, inline with other reports suggesting that stent-graft migration occurs more frequently in AAAs with larger diameter (>60 mm).

In the last generations of endografts many refinements have been made to minimize the probability of device migration even in challenging anatomies through suprarenal fixation system, iliac bifurcation fixation system , the use of active fixation anchors system or even with inflatable sealing rings [13], [14]. However long-term follow-ups are needed to confirm this prediction on the superior performance of the new generation endografts.

Conformational alterations

Conformational alterations are visible changes in the morphology of the endograft, in particular they can be represented by kinking and bending of the device. Figure 1.11 shows an example of stent-graft kinking. These deformations can contribute to significant

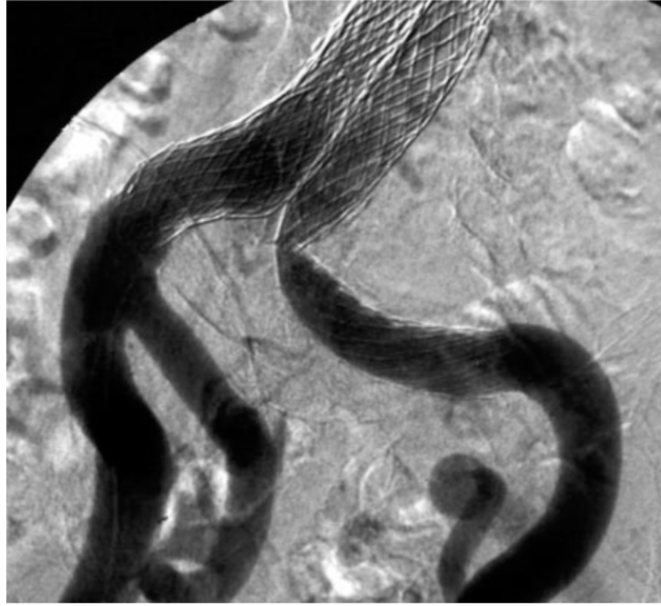


Figure 1.11: In the picture the five types of endoleaks are graphically depicted.

late clinical complications. Main problematic feature leading to these kind of complications is the fact that neither prostheses has the longitudinal elasticity of a natural vessel. Stent-graft kinks are strictly related to the aortic neck angulation: an increase in the angulation between the body of the prosthesis and its limbs may be a predictor of kinking [15]. Different theories have been put forth to explain kink formations: White et al suggested that the shortening of the stent-graft during deployment followed by the expansion to its original length determines a distortion; Harris et al. associated the occurrence of kinking with the longitudinal shrinkage of the aneurysm; finally, Umscheid et al. [16] hypothesised the migration from the proximal or distal anchoring sites as a cause of kink. For sure, kinks are potentially damaging events, inducing a stenosis of the stent frame that may lead to graft thrombosis, type I and III endoleaks, migration, graft stenosis, all complications needing an open surgery. Of vital importance are follow-ups and rigid surveillance after EVAR are of utmost importance.

1.6 Aims of the work

In the previous paragraphs we have introduced the clinical problem and its surgical treatments, i.e. open repair and endovascular aortic repair (EVAR). We also highlighted the possible phenomenology of stent-graft after EVAR. The present thesis focuses on

the clinical outcomes of EVAR by quantitatively assessing the stent-graft displacements both over cardiac cycle and between several follow-ups. Moreover we try to investigate a possible relation of such displacements with the hemodynamic variables obtained by CFD simulations. A quantitative assessment of the mechanical action of the stent-graft and of the aortic fluid-dynamics may support a correct planning of the surgical procedure, improving its clinical outcomes.

This work was developed in collaboration with Fondazione IRCSS Ca' Granda, Ospedale Maggiore Policlinico, Milan. Specifically, we collaborated with Dr. Maurizio Domanin, from the Division of Vascular Surgery and with Dott.ssa Laura Forzenigo, from the Radiology Division, who provided the diagnostic images.

The first step of the thesis consisted of patient-specific structural analysis of the EVAR device through medical image processing, while the second step consisted in the CFD simulations, after suitable mesh generation of the lumens of the aorta.

Three patients with AAA evaluated for endovascular repair were studied through the acquisition of ECG gated CTA images of the abdomen. For each patient we have two or three follow-up analyses and for each of them we have dynamic CT images: 10 images captured during one cardiac cycle in order to detect stent-graft movements.

For the geometry reconstruction and stent-graft displacements analysis, the Vascular Modeling Toolkit (VMTK) was used [17], in order to capture the possible device phenomenology after its deployment, such as migration or conformational alterations. The importance of the assessment and quantification of stent-graft displacements has been considered by several authors in the previous studies. Some authors concentrated on one-dimensional [18][7],[19] or two-dimensional [20] techniques to detect device migration. In particular, Benharash et al [7] measured longitudinal centerline distance from the superior mesenteric artery to the top of the stent graft on preoperative, postimplantation, and 1-year three-dimensional computed tomographic scans. In the work of Zarins et al [19] distance from the renal arteries to the proximal end of the stent graft and the proximal fixation length (length of the infrarenal neck covered by the stent graft) were determined. Rafii et al [20] calculated lateral movement of an aortic endograft and found out that it is associated with increased risk of late adverse events and hence was a good predictor of migration. A more recent study of Nemoto et al [21] focused on stent-graft length and curvature changes as geometric criterion to demonstrate post-operative EVAR results. In this latter work, authors calculated morphological changes of the stent-graft by developing an image-based modeling system, called V-Modeler, based on segmentation of device, centerline extraction and centerline length and curvature evaluation. However, stent-graft movement is a more complex and three-dimensional event than the simple downward displacements with respect to a fixed reference point or changes of centerline in curvature and length. Quantification of 3D positional changes

of the endograft over time was first approached by Figueroa et al [11] who assessed the non-uniform movement of the device. The latter study quantifies the graft movement by analysing the position of the centroid of the device. The 3D stent-graft movement has been evaluated more recently also by Nolz et al [10], but in this case the behaviour of type 2 endoleak in relation with surface movement of the device is the main objective. They found that type 2 endoleak may stabilize the stent-graft, which experiences a decreased device movement.

We performed the segmentation technique on the ECG gated series of axial images, reconstructed at every 10% of the R-R interval, to detect stent-graft geometry at every time-step of the cardiac cycle. By the registration of the geometries we could evaluate, when image quality was not too low, the overall 3D positional changes of the stent-grafts. Since for each of the three patients we had several follow-ups CT images, we were able to analyse both the device displacements over cardiac cycle and between two different follow-ups in order to completely understand its behaviours.

For the second step, CFD simulations to compute post-EVAR hemodynamics was performed. Numerical simulations were performed with the software LifeV, an open source library. Computational methods are considered of utmost importance in clinical field, since they allow the reproduction of almost every type of problem in which a fluid is involved. Moreover, non-invasiveness has become a major requisite, because it may allow to perform such investigation on a number of normal and pathologic real cases, and to follow the temporal evolution of the vascular pathology. To date, no in-vivo non-invasive velocimetry techniques is able to determine important measurements, such as velocity, wall shear stress, pressure distribution and so on. 3D CFD simulation allows personalized quantitative analysis with a modest invasiveness for the patient. In addition, fluid dynamic analysis can be used to accurately determine the nature of blood flow in the cardiovascular system and develop models to predict factors affecting progression of disease. CFD approaches are largely used in studies to evaluate post-EVAR outcomes. Now we describe few of the researchers who performed hemodynamic simulations on patient-specific stent-graft lumens. For instance Raptis et al [22] computed fluid-dynamic quantities, such as WSS, helicity, pressure and velocity, in order to perform statistical comparisons between physiological and postoperative flow data. The comparisons revealed that significant variations in hemodynamic properties occur in the iliac arteries part. An interesting approach is adopted by Stefanov et al [23] who conducted their study on bifurcated stent-grafts for the treatment of AAAs including the whole human aorta, i.e. ascending aorta, aortic arch, descending aorta and the associated branches. They found that the inclusion of the full aorta generates a highly skewed input flow field, which continues downstream towards the bifurcation. Beyond bifurcation the flow is very similar to the one without the inclusion of the full aorta. An example of CFD coupled

with structural analysis leading to a fluid-structure interaction problem has been reported in the study of Frauenfelder et al [24]. They simulated pulsatile flow including realistic wall deformation in order to evaluate the hemodynamic changes in AAA after stent-graft placement. An important finding of this study is the reduction of pressure inside the aneurysm sac, that is the real purpose of the stent-graft implantation, but this pressure is not zero, even if the sac is completely excluded by the stent-graft. These results highlight the complexity of the fluid-structure interactions between the blood flow, stent, and thrombus, which in some cases might lead to endotension. Numerical simulations have been performed also to assess effects of endoleak on the aneurysm intrasac pressure in case of an incompletely excluded abdominal aortic aneurysm. For instance, Wolters et al [25] Lu et al [26] employed a 3D CFD methods to analyse endoleak formation from the hemodynamic perspective. They developed a fluid-structure-interaction (FSI) method to provide detailed flow close to stent-graft wall structure.

Starting from this pioneering analysis, the further task of this study is the attempt to find a correlation between fluid-dynamic results and the 3D displacements evaluated through the image-processing briefly previously described, both over cardiac cycle and between several follow-ups, in order to have a complete evaluation of the post-EVAR outcomes.

Chapter 2

Medical image processing

In this chapter we focus on the first step of our work: the patient-specific structural analysis of the EVAR implant. To this aim, by using the Vascular Model Toolkit Library (VMTK, <http://www.vmtk.org>) we extracted stent-grafts geometry (segmentation), superposed the geometries to match the reference systems (registration) and, finally, calculated displacements both within an heartbeat and among different times of the follow-up studies. In the following paragraphs we describe specific clinical cases under investigations, the images set-up and the detailed process which generated the geometrical stent-grafts reconstructions including their positional changes over time.

2.1 Dataset

2.1.1 Clinical cases

We studied three clinical cases of post-EVAR outcomes: Patient I, Patient II, Patient III. All three patients presented an abdominal aortic aneurysm and they underwent EVAR procedure between 2007 and 2008. They were evaluated for the mini-invasive treatment because of hostile abdomen, high risks condition, advanced age or patient choice. Periodic follow-up examinations are required in order to detect complications, including blocking of the blood flow and leakage into the aneurysm sac induced by stent graft migration, fracture or kinking. Time between follow-ups is not the same in our three clinical cases. Patient I and Patient III have three follow-up images: the first one after one month (PI-T1), one year (PI-T12) and four years (PI-T48); the second one after one month (PIII-T1), one year (PIII-T12) and 60 months (PIII-T60). For Patient II we have two follow-ups: one after one year (PII-T12) and the other one after 60 months (PII-T60).

2.1.2 Type of images

The input of the framework is a set of medical images, in DICOM format, acquired by 4-dimensional computed tomography with Siemens SOMATOM Definition AS scanner (Siemens Medical Solutions, Erlangen, Germany). Ten ECG gated series of axial images were reconstructed at every 10% of the R-R interval from the aortic arch to the common femoral arteries. This approach allows the retrieval of dynamic imaging of the aorta during a complete systolic-diastolic cycle.

Computed Tomography (CT) is based on the computer-processed combination of many X-ray images taken from different angles to produce cross-sectional images of specific areas of a scanned object, see Figure 2.1. The CT captures images by detecting the attenuation that ionizing radiations undergo when they pass through body tissues and attenuation depends on the tissue capability of absorbing radiations. The X-ray source rotates around the object while the object is moved through the scanner in longitudinal direction. This enables scanning the complete object in one continuous motion. Three important factors contributing to the detector efficiency are geometric

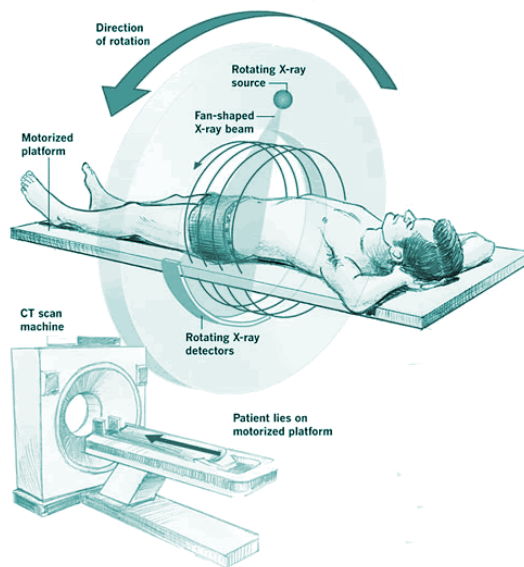


Figure 2.1: Illustration of how CT works: the scanner consists of an X-ray emitter situated opposite the detectors. As the scan begins, the patients bed slowly moves through the tunnel and stops; the scanner then circles the patient, emitting X-rays, which are beamed through the patient and detected along the circumference of the tunnel; each time the bed moves the scanner circles again. After the area of interest has been scanned, a computer analyses the information received and constructs a transverse image of the body.

efficiency, quantum (also called capture) efficiency, and conversion efficiency. Geometric

efficiency refers to the efficiency with which the detector intercepts radiation emitted from the source and it is determined mostly by detector size and the distance from the source to the detector. Quantum efficiency refers to the fraction of incident x-rays on the detector that are absorbed and contribute to the measured signal. Conversion efficiency refers to the ability to accurately convert the absorbed x-ray signal into an electrical signal. The product of the above three efficiency is called overall efficiency or, rarely, dose efficiency [27]. Data-acquisition system (DAS) interfaces the x-ray detectors to the system computer in order to encode the acquired results into digital values. In the continuous space an image can be defined as a function $I(\mathbf{x}) : \mathbb{R}^3 \rightarrow \mathbb{R}$; i.e. to any point \mathbf{x} in the domain \mathbb{R}^3 (the spatial coordinates) I associates a scalar value called the intensity or grey level of the image at that point. In the discrete space, a digital image is a function $I(m,n)$ where I is the intensity of the pixel and m and n define the position of the pixels in the image grid composed by M rows and N columns.

In our case ECG-gated CT images have been acquired. The technique of ECG gating enables investigation to temporal behaviour of the scanned object, since patient's ECG signal is measured during scan and data is captured synchronously with the patient's heart beat. CT reconstructions were made at 10 equidistant time points over a single cardiac cycle and other motions, such as those caused by breathing result in motion artifacts [28]. This type of CT is extensively used in cardiac exams but the goal is generally to limit the effect of motion rather than examine the motion itself. However, we used ECG-gated CT to study the pulsatility motion of the stent-grafts during the cardiac cycle, in addition to inter-follow-ups motion. All CT images are in DICOM format. Digital Imaging and Communications in Medicine (DICOM) is a standard developed by ACR (American College of Radiology) and NEMA (National Electrical Manufacturer's Association). It combines visual information of medical exams (compressed or in raw data), in our case CT scans, to other technical information about patient (date of birth, diagnosis, name of the doctor and so on), machines, the exam. By using this format, hospitals are able to easily communicate among each other. We used a DICOM viewer software, called RadiAnt, to examine both CT scans and alphanumeric information, including the following technical characteristics:

- **Patient I:**

PI-T1: reconstruction matrix: 512 x 512 x 926, slice thickness 1.5 mm
 PI-T12: reconstruction matrix: 512 x 512 x 715, slice thickness 1.5 mm
 PI-T48: reconstruction matrix: 512 x 512 x 717, slice thickness 1.5 mm

- **Patient II:**

PII-T12: reconstruction matrix: 512 x 512 x 1006, slice thickness 0.6 mm
 PII-T60:

reconstruction matrix: 512 x 512 x 616, slice thickness 1.5 mm

- **Patient III:**

PIII-T1: reconstruction matrix: 512 x 512 x 1002 pixels, slice thickness 0.6 mm

PIII-T12: reconstruction matrix: 512 x 512 x 1001, slice thickness 1.5 mm

PIII-T60: reconstruction matrix: 512 x 512 x 607, slice thickness 1.5 mm.

In Figure 2.2 examples of CT scans are depicted.

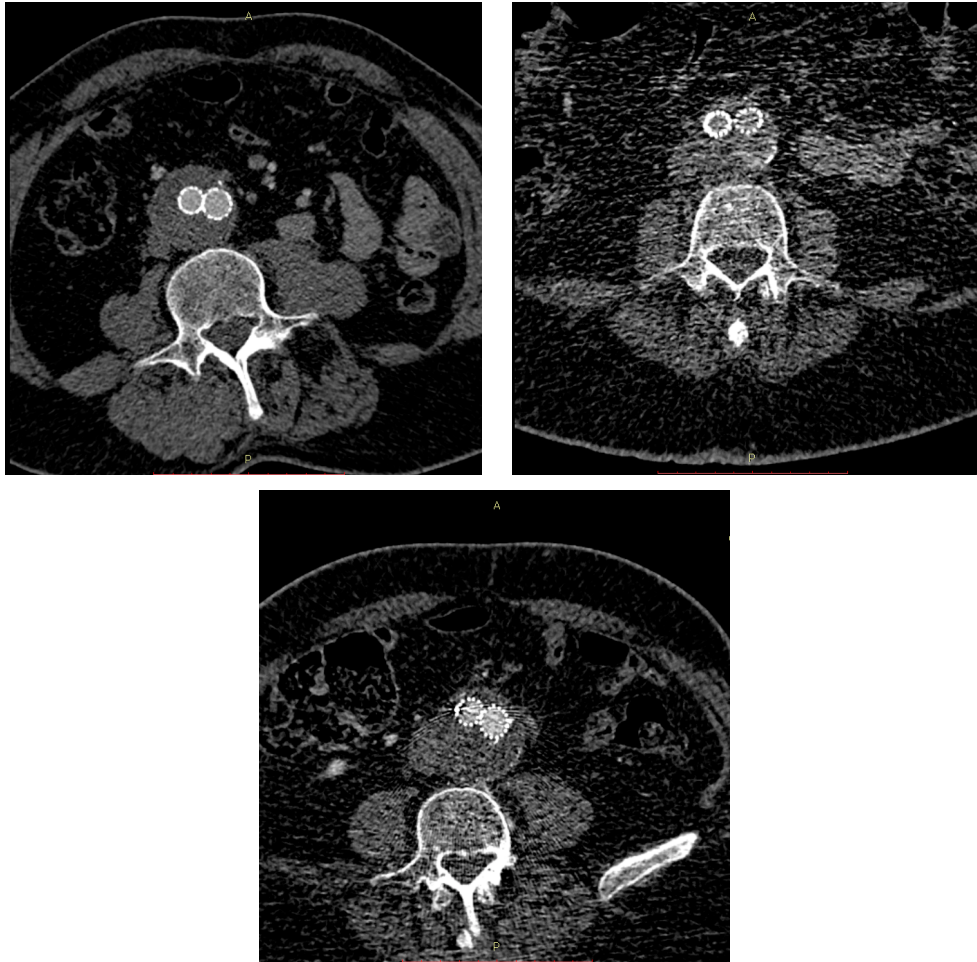


Figure 2.2: Examples of single CT scans of each patient at the first follow-up examination, i.e. T1. Top, left: PI-T1; top, right: PII-T1; bottom: PIII-T1.

2.2 3D geometric analysis: Stent-grafts segmentation

The procedure of the extraction of an area of interest from an image volume is called segmentation. The segmentation result is of utmost importance in many biomedical applications: study of anatomical structure, treatment planning, diagnosis, quantification

of tissue volumes, localization of pathology, assess of treatment outcomes. More precisely, image segmentation is the process of assigning a label to every pixel in an image such that pixels with the same label share certain characteristics. Each of the pixels in a region are similar with respect to some characteristic or computed property, such as colour, intensity, or texture. The image partitioning level depends of the problem considered and segmentation should end when the object of interest has been found.

There are different existing techniques which are used for image segmentation. They all can be approached from three basic methods of segmentation: thresholding, region-based methods and edge-based methods. Latter one is the method we decided to exploit.

Thresholding: In thresholding pixels are allocated to categories according to the range of values in which pixels lies. It is the simplest and most commonly used method of segmentation. Given a single threshold, t , the pixel located at position (i,j) , with greyscale value f_{ij} , is allocated to category 1 (object to detect) if $f_{ij} \leq t$, otherwise the pixel is allocated to category 2 (background). Threshold t is often chosen manually by the operator who is performing image segmentation, by trying a range of values of t and seeing which one identifies better the object to detect. A number of thresholding techniques have been proposed so far using global and local techniques. Global methods apply one threshold to the entire image while local thresholding methods apply different threshold values to different regions of the image [29].

Region-based method: This approach is based on algorithms operating by grouping together pixels which are neighbours and have similar values and splitting groups of pixels which are dissimilar in value. They are more immune to noise with respect to edge-based techniques, on the other hand they are expensive in terms of time and memory.

Edge-based method: This techniques is based on the identification of image edges. All edges are connected together to form the object boundaries required to segment wanted regions. Edge detection is a series of actions whose purpose is to recognise points in an image where clear and defined changes occur in the intensity [30]. There exists many algorithms able to detect edges and they can be groups into two categories: search-based and zero-crossing based. In case of search-based methods first directional derivative of image intensity function is computed and then its local maxima (or minima) are identified, i.e. peaks (or valleys) of the image function. Since a digitalised image is not a continuous function of the spatial variables but rather a discrete function of the integer spatial coordinates, algorithms performing search-based edge detection can only be seen as approximations to the true spatial derivatives of the original spatially-continuous image. These algorithms only differ in type of filtering used to compute the first derivatives at each pixel of the image. Some examples of such operators are reported in Robert, Prewitt and Sobel [31]. Crossing-based methods are based on searching a zero

crossing in the second derivative of the image. A zero crossing at a certain pixel implies that the signs of at least two opposite neighboring pixel are different. Both methods have advantages and disadvantages: search-based algorithms have the advantage of having a very simple implementation and run extremely fast but they have problems such as noise and discontinuity of the edges. Crossing-based methods involve more operations but they allow a better quality in results.

Several studies have been published on the segmentation of blood vessels in 3D. For example, Antiga et al [32] studied an efficient methodology to reconstruct, analyze and discretize patient-specific models of vascular structure from medical images. The reconstruction of vessel of interest was based on a gradient-based deformable algorithm implemented with the level set approach. Other authors, such as Beck et al [33], proposed methods that segment the contour in slices perpendicular to the vessel centerline. Their algorithm is divided into two consecutive steps: in the first one a section of the vessel tree is mapped to the model so that the desired centerline is entirely included, while in the second step the centerline is extracted.

Aim of our work is detection of stent wires. Since stent-grafts are characterized by sharp corners of the wire, small wire diameter, leaks and gaps due to artifacts which blood vessels do not feature, methods developed for vascular elements segmentation are not suitable for stent graft wires reconstruction. Several methods to specifically obtain the geometric model of the stent wires from volumetric CT data were implemented. For instance, Langs et al [34] found stent frame by the use of a statistical deformation model. This model is able to adapt to the deformation behaviour of the endograft. Klein, in his PhD dissertation [35], proposed a highly innovative geometric model to represent wire frames of the stent as an undirected graph, with nodes placed at the corners and crossings of the frame, and the edges between the nodes representing the wires.

2.2.1 Vmtk

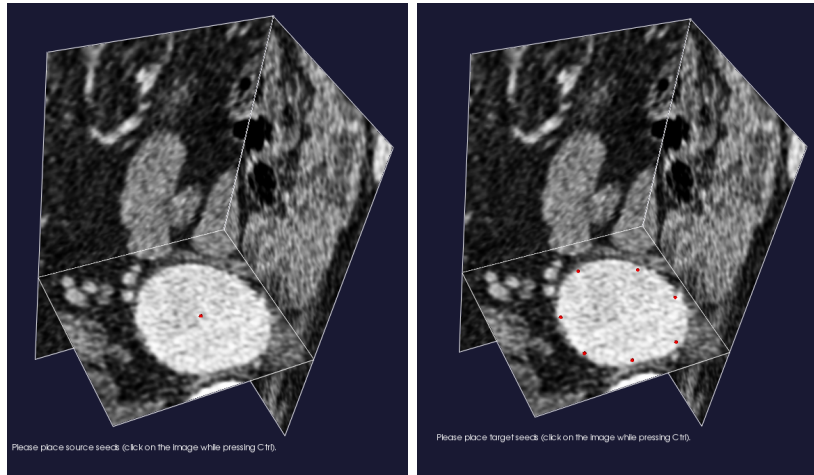
We performed segmentation of stent-graft by using the Vascular Modeling Toolkit (VMTK, <http://www.vmtk.org>). It is a collection of scripts and classes for image segmentation, geometric characterisation and processing, mesh generation and post-processing for vascular modeling. This tool allows to obtain a segmented 3D surface by using level set algorithms. Level sets are a kind of deformable model in which the deformable surface is not presented by a set of points and triangles but rather described by a 3D function, i.e. another image whose contour at level zero is the surface in question. In practice, the output of level set segmentation is an image. The advantage of using a deformable model is that the location of the surface will not depend on the chosen level, but instead it will locally conform to the peaks of the gradient modulus of the image

levels. In order to use level sets in VMTK, we ran the `vmtklevelsetsegmentation` script. First step is the choice of the way in which deformable model has to be initialized. There are different initialization strategies to choose the level set zero:

- **Isosurface:** initial level sets will correspond to an isosurface of the image with sub-pixel precision.
- **Threshold:** pixels comprised within two specific thresholds will be selected as initial level sets.
- **Fast marching:** this initialization type consists of placing a set of seeds and a set of targets on the image. A front is then propagated from the seed until the first target is met at which point the region covered by the front is the initial deformable model. This method is suitable for objects with a round shape, such as aneurysms. As shown in Figure 2.3(a), a seed point is put in the centre of, for instance, aneurysmatic sac, and target seeds at aneurysmatic wall.
- **Colliding fronts:** it consists of placing two seeds on the image. Two fronts will be propagated from the seeds (one front from each) with their speeds proportional to the image intensity (see Figure 2.4). Region where the two fronts cross or collide is then the initial deformable model. Seeds selection is a crucial step since it depends on user's experience. This method is highly effective in case of blood vessels reconstruction [36].

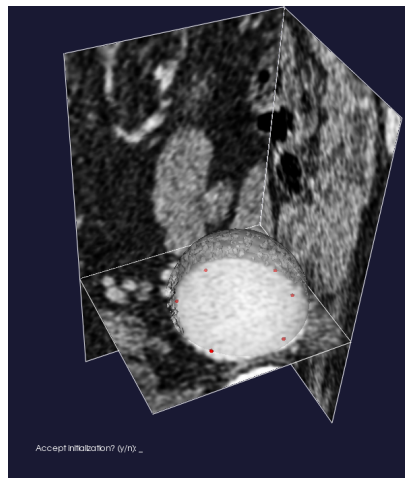
It is possible to reconstruct the object by using different initialization types and then merge the results into a single final model. For our purpose, threshold initialization was used, since other initialization methods are more suitable for vascular reconstruction. Once type of initial deformable model is chosen, software guides the operator into level set initialization procedure that in case of threshold strategy consists of setting lower and upper image intensity thresholds. As shown in Figure 2.5, wires of the stent-grafts are highly visible in CT scans since they are often made of nitinol, a radiopaque material. Sometimes additional radiopaque markers are used in order to better analyse device behaviour in post-EVAR follow-ups. In our patient's CT exams, image intensity of stent-grafts ranges between 500 to 2000 Hounsfield Units (HU), much higher values with respect to all surrounding tissues.

The results of the level set procedure described above are improved by setting number of iterations, propagation scaling, curvature scaling and advection scaling. We always



(a)

(b)



(c)

Figure 2.3: Fastmarching initialization of Patient II aneurysm: (a) selection of source seed, (b) selection of target seeds, (c) resulting initial level set.

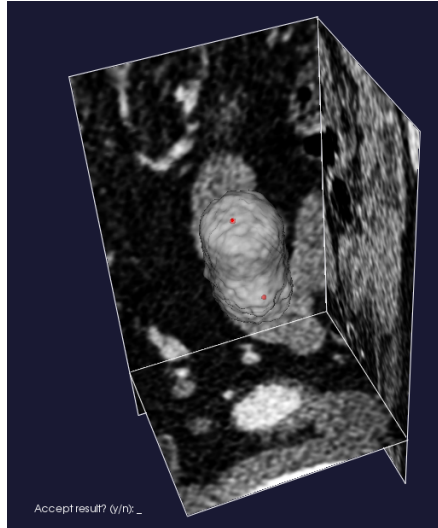


Figure 2.4: Colliding fronts initialization of part of Patient II aorta. Two seeds are located in two points along the vessel and level set algorithm reconstructs the surface.

chose 100 as number of iterations and left default settings for remaining parameters, i.e. 0 for propagation and curvature scaling and 1 for advection scaling. The level sets then evolve until the maximum iterations are reached and the surface generated is the zero level of input image. By using the command `vmtkmarchingcubes` a polygonal surface, i.e. a triangulated surface, is extracted from the zero level.

In some cases some problems may occur if there exist other tissues characterised by high radio-density or CT image artifacts. For example, in Figure 2.6(a) geometrical reconstruction is shown of both the device of Patient I and parts of vertebral bones, whose intensity values are in the interested range, while Figure 2.7(a) is a demonstration of CT scans artifacts occurred in Patient II and III cases.

In order to eliminate all structures that are not strictly the stent-graft, the command `vmtksurfaceconnectivity` is used. It extracts the largest connected region, the closest point-connected region or the scalar-connected region from a surface. Patient I stent-graft is a single whole surface, much larger than the erroneously reconstructed vertebrae so that Surface Connectivity algorithm is able to extract device 3D geometry as we wanted. In Figure 2.6(b) final segmentation is shown. In case of Patient II and III, the implanted endograft consists in several circular wires sewed to the tissue in order to maintain an overall tubular shape but divided one from each other. For this reason the Surface Distance algorithm recognize as the largest connected region one of the metal wire or one of the vertebrae. Hence, we used a step by step strategy consisting in:

- `vmtksurfaceclipper`: we used this command in VMTK in order to isolate every single circular struct. Hence, we obtained one output surface for each struct.

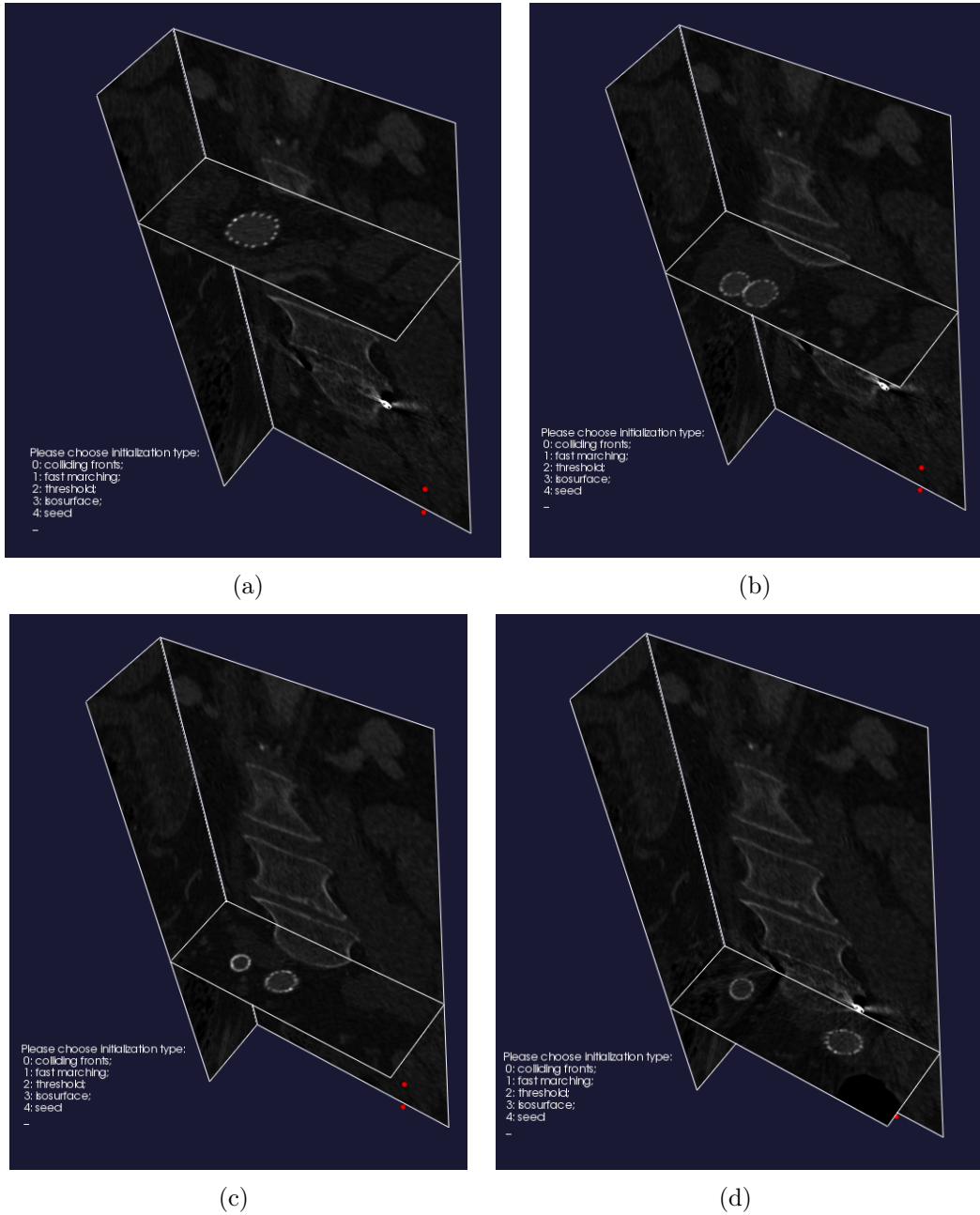


Figure 2.5: Stent-graft is easy to detect in our CT images since it is characterised by significantly higher values of radiodensity.

- **vmktsurfaceconnectivity**: this step was applied to each of the single circular wire in order to get rid of segmentations of the little artifacts and vertebral bones.
- **vmktsurfaceconnectivity**: by applying this command, all wires previously separated were connected together in a single output file, as shown in Figure 2.7(b).

We performed segmentation procedure for each of the ten time instants of dynamic follow-up CT scan, for each patient.

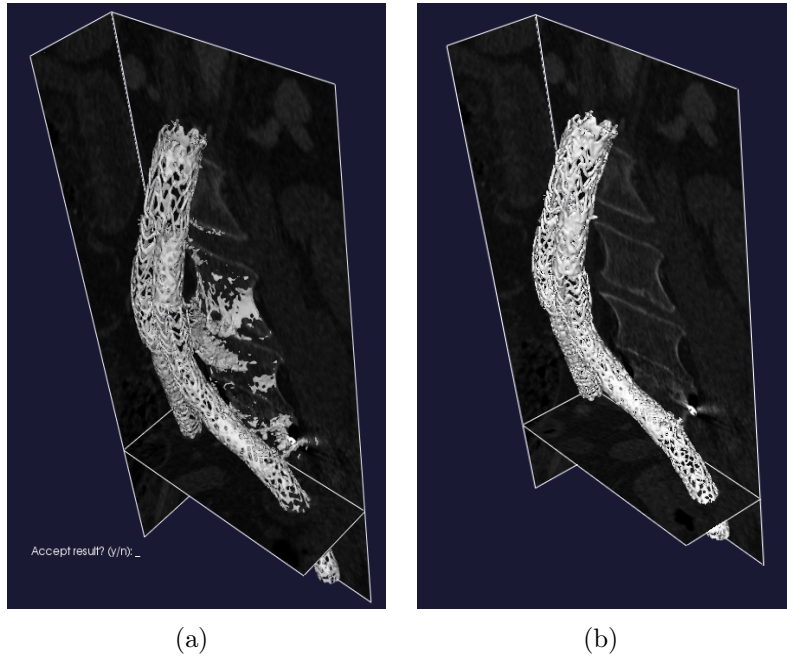


Figure 2.6: Example of 3D geometrical reconstruction of the stent by using threshold level set initialization. (a) Since intensity level of vertebrae is similar to the one of stent-graft's wires, resulting output of level set procedure revealed both structures. (b) If surface connectivity algorithm is used, only stent-graft geometry can be obtained.

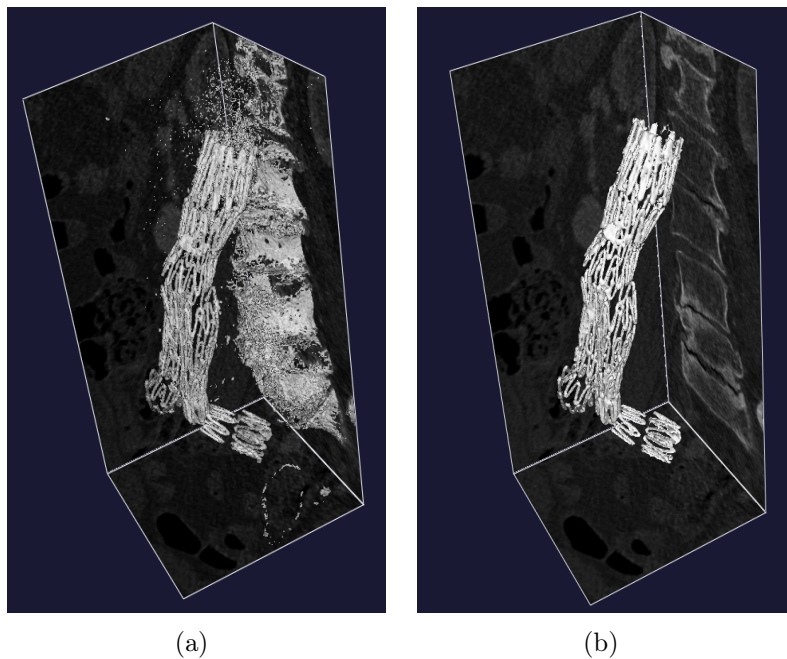


Figure 2.7: Reconstruction of stent-graft of Patient III by using threshold level set initialisation. (a) Artifacts and vertebral bones are segmented in addition to our wanted surface. (b) By applying `vmtksurfaceconnectivity` command for each of the separated circular wires and `vmtksurfaceappend` to create a single surface, the whole clean stent-graft is correctly segmented.

2.3 Computation of stent-grafts displacements

In this work we focused on the assessment and quantification of displacements experienced by stent-grafts over cardiac cycles as well as during a time interval of several months. To this aim, we reconstructed geometric surfaces of the endograft of each patient, as described in the previous sections. In Sections 2.3.1 and 2.3.2 we illustrate how we used algorithms implemented in VMTK library in order to achieve our aim.

2.3.1 Computation of stent-graft displacements over cardiac cycle

To quantitatively evaluate the movement of the stent-grafts over cardiac cycle, we computed displacements of each point of the reconstructed surface with respect to the diastolic instant, i.e. the 7th time frame. We compute the point-wise minimum distance between two surfaces, current and reference one, using the module `vmtksurfacelistance`. Euclidean distance is computed from each point of the current surface to the closest triangle on the reference surface. In particular, we calculated the so called Signed Distance: distance is positive if distance vector and normal to the reference surface have negative dot product, i.e. if the input surface is outer with respect to the reference surface. In this way nine colored maps of stent-grafts displacements are obtained. In Chapter 3, we will discuss the corresponding results.

2.3.2 Computation of stent-grafts displacements among follow-ups

In this section we describe procedure to compute displacements of patients' stent-grafts over cardiac cycle. To this aim registration is needed. Registration is the process of transforming different sets of data into one coordinate system. This task is of utmost importance since all stent-graft geometric reconstruction have different reference systems. Algorithm we used is the Iterative Closest Point (ICP) proposed by Besl [37]. One point cloud, the reference, is kept fixed, while the other one, the source, is transformed to best match the reference. The algorithm needs to find for each point in the source point cloud the nearest point in the reference point cloud, so that all 3D source coordinates can be correctly matched and overlapped. In VMTK this rigid transformation is performed by using the command `vmtkicpregistration` and by selecting reference and source surface. We chose to register all geometric reconstructions of the stents in coordinate system of the most recent follow-up, i.e. T48 for Patient I and T60 for Patient II and III. See Figure 2.8, Figure 2.9 and Figure 2.10 for ICP registration application on

Patient I, II and III, respectively.

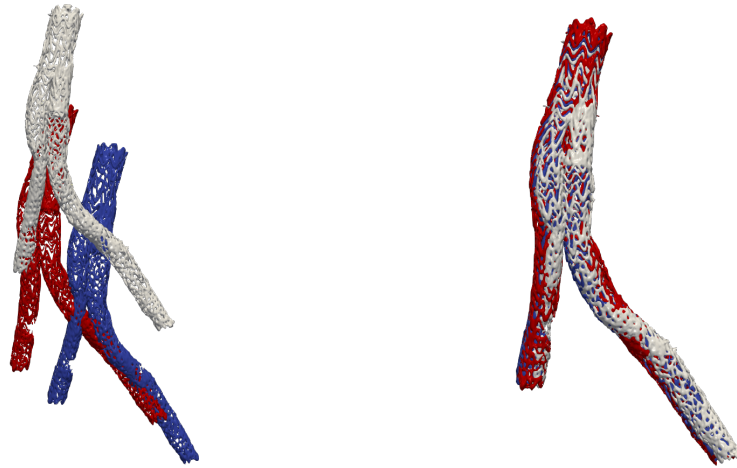


Figure 2.8: By applying ICP algorithm to endograft of Patient I we obtained PI-T1 and PI-T12 graft surfaces translated into PI-T48 coordinate system.

Once registration is performed for all the three patients, displacements of stent-grafts among follow-ups were computed. As in case of displacements over cardiac cycle, we used the `vmksurfacelistance` command in VMTK. In Chapter 3, we will describe the corresponding results in details.

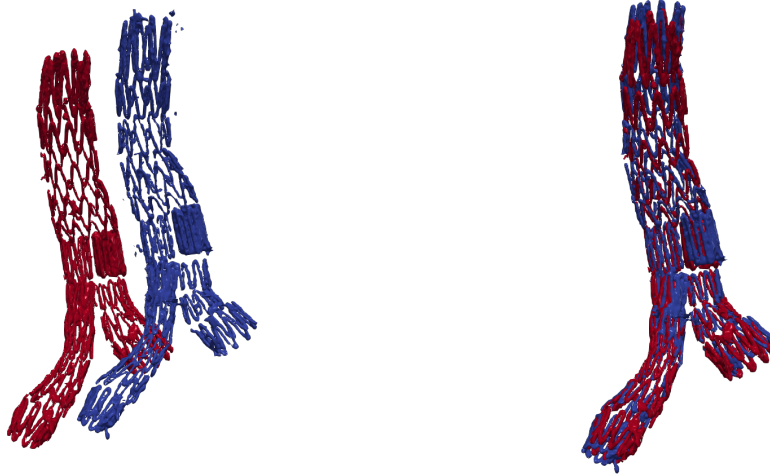


Figure 2.9: Result of registration procedure applied to stent graft of Patient II in order to translate PII-T12 surface into coordinate system of PII-T60.

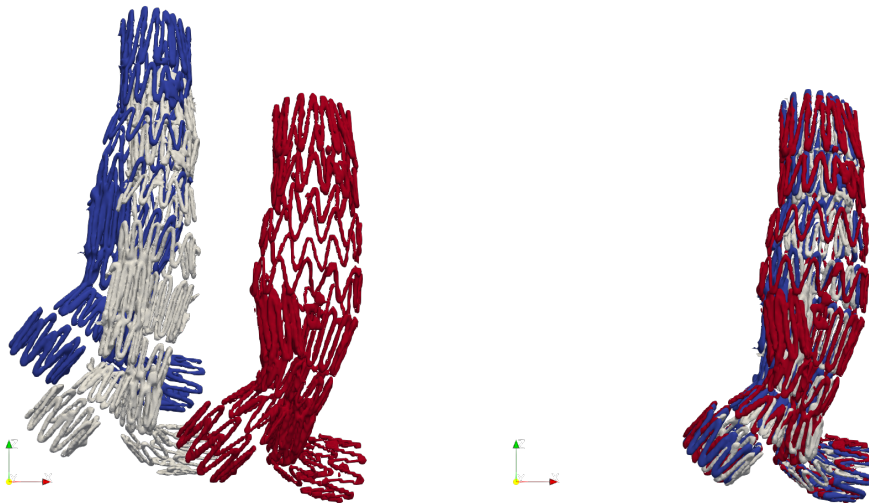


Figure 2.10: On the left segmentations PIII-T1 (white), PIII-T12 (blue) and PIII-T60 (red) have different coordinate systems. On the right the result of Iterative Closest Point registration: PIII-T1 surface and PIII-T12 are set, in separately procedures, as source point clouds while PIII-T60 surface is the reference one, so that PIII-T1 and PIII-T12 surfaces are rigidly transformed to have the same coordinate system of PIII-T60.

Chapter 3

Geometric analysis results

In the previous chapter we described the procedure used to obtain stent-grafts 3D geometric reconstruction and how we computed displacements over cardiac cycles and among several follow-ups. In this chapter we present the resulting segmentations and endograft displacements.

3.1 Configurations of the segmented stent-grafts

By using VMTK we could reconstruct geometries of stent-grafts of the three patients. Since each patient underwent post-operative surveillance twice or three times, we performed device reconstructions for all available follow-ups. Dynamic CT scans, i.e. a series of axial images every 10% of the R-R interval, allowed us to detect stent-graft position at several times during cardiac cycle, so that we segmented endografts ten times for each follow-up. In the following subsections results of the segmentation procedure are illustrated for the three patients. For the reason that in Section 3.2 we will show all ten stent-graft geometries of the cardiac cycle, whereas in what follows we present stent-graft segmentations at the seventh time instant, i.e. at diastolic peak considered here as the reference one with respect to which the displacements are calculated.

3.1.1 Patient I

We have at our disposal three follow-ups of Patient I: after one month (PI-T1), twelve months (PI-T12) and forty-eight months (PI-T48) post-EVAR. In order to check if reconstruction is done properly, segmentation is compared with 3D rendering of CT images provided by RadiAnt, a DICOM files viewer. In Figure 3.1 an example of this comparison is shown, from which we can state the segmentation procedure described in the previous chapter was effective.

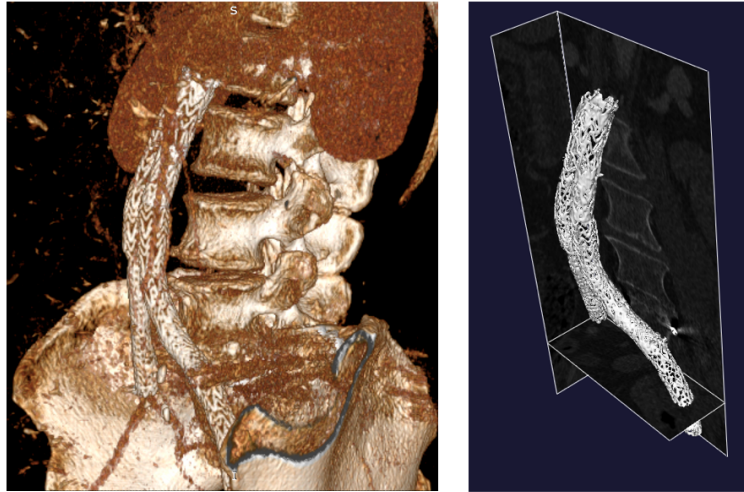


Figure 3.1: Comparison between 3D rendering of PI-T1 stent-graft from CT scans in RadiAnt and PI-T1 stent-graft segmentation we performed.

More in detail PI-T1 stent-graft, see Figure 3.2, resulted to be well reconstructed except for part of the right iliac branch, which seems to lose metal wire features of the rest the device. This artefact is probably due to a more narrowed network of stent-graft struts that CT scan was not able to properly detect.



Figure 3.2: PI-T1 stent-graft segmentation.

In Figure 3.3 3D geometry is depicted of stent-graft after 12 months from EVAR

procedure. Some specific issues about migration, deformations and displacements with respect to PI-T1 will be discussed in section 3.3.1. Here we observe that, compared to segmentation of the device after one month from deployment, this reconstruction exhibits missing parts, as shown in the box of Figure 3.3. Same artifacts occur in case of last follow-up geometric analysis, see Figure 3.4. This problem could be due to the fact that Patient I had hip prostheses at both sides, which determined artifacts in the CT images. They occur because the density of the material of hip replacements is beyond the normal range that can be handled by the CT detector. This problem is relevant in distal regions, i.e. near hips, where lights and shadows prevented to detect some of the stent-graft wires (see Figure 3.5).



Figure 3.3: PI-T12 segmented stent-graft. A detail of the missing wires of the device is shown in the box.

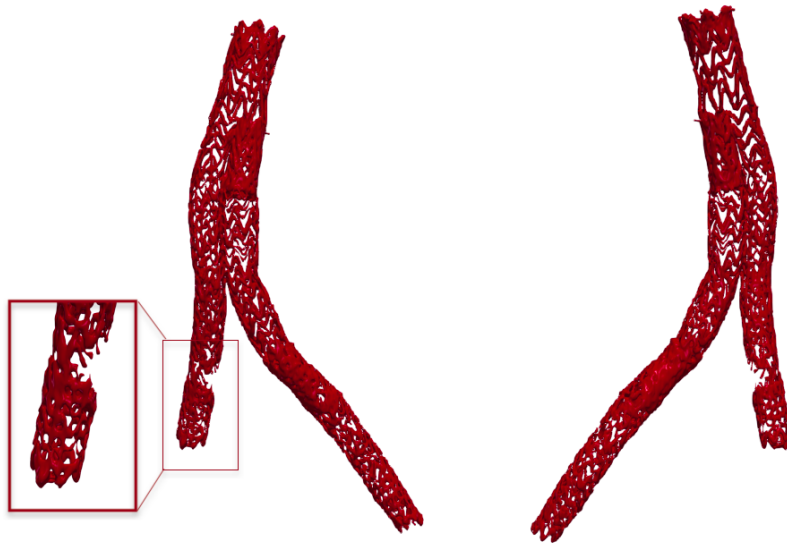


Figure 3.4: PI-T48 segmented stent-graft. As in case of PI-T12, missing metal structures are zoomed in the box.

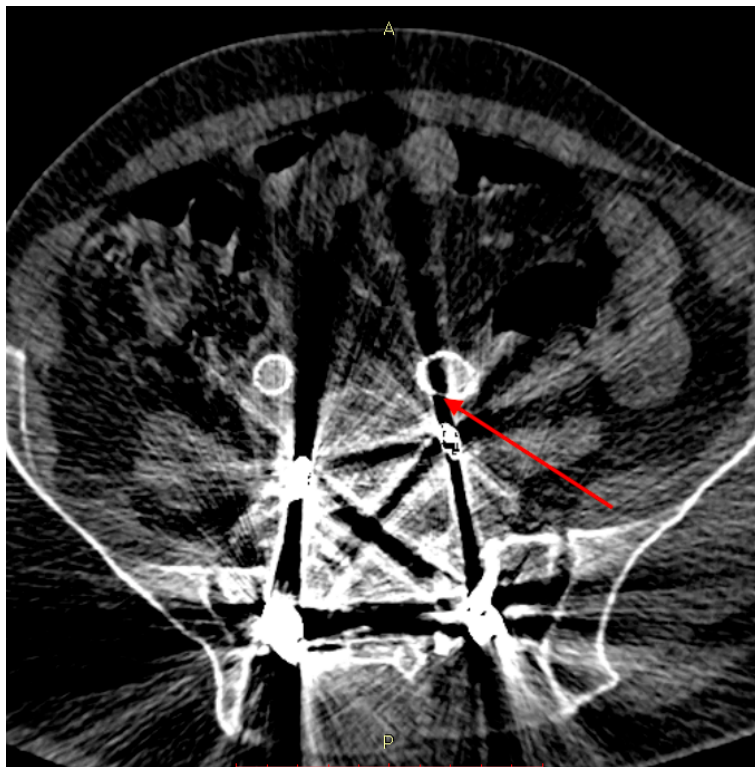


Figure 3.5: Metal artifacts arising from hip prostheses of Patient I. Red arrow denotes region where stent-graft falls in a blind zone so that it can be segmented.

3.1.2 Patient II

We reconstructed Patient II stent-graft from CT images acquired after one year (PII-T12) and sixty months (PII-T60). 3D geometric reconstructions exhibit some problems. In case of PII-T12, see Figure 3.6, surface of the endograft is not perfectly smooth but presented many bumps and wires show several artifacts. Figure 3.7 illustrates segmentation of stent-graft PII-T60 characterised by artifacts similar to the PII-T12 ones. Origin of this bumpy surface may be the poor quality of CT images. In fact, they exhibited a low contrast resolution which prevented us to properly detect endograft wires.

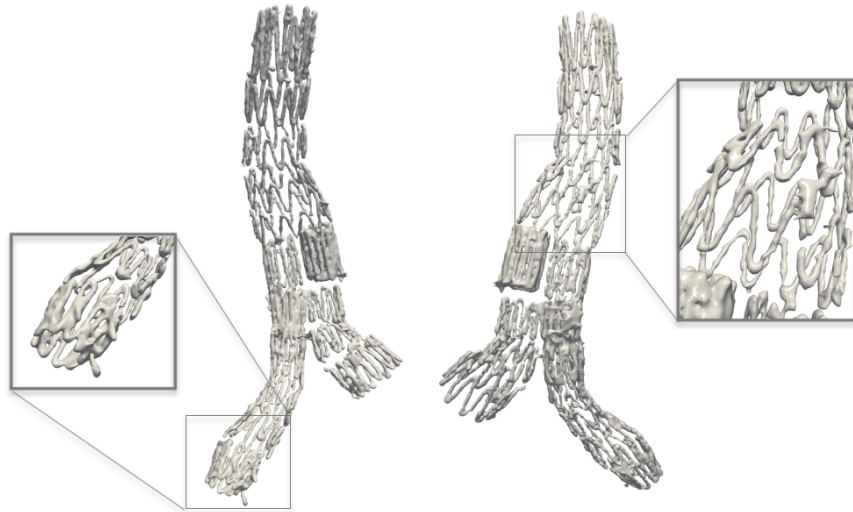


Figure 3.6: PII-T12 segmented stent-graft. Reconstruction shows a surface not properly similar to a metal stent, as we should expected. Zoomed portions of the surface allow a detailed detection to these artifacts.

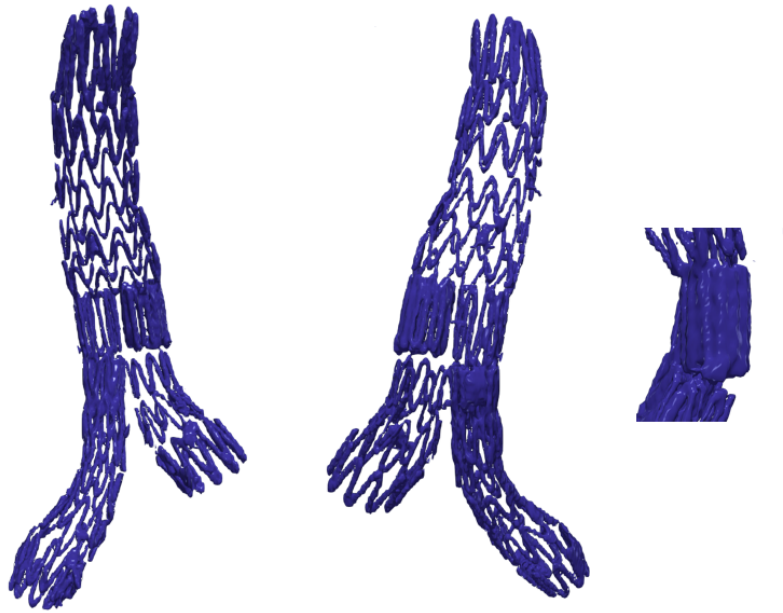


Figure 3.7: PII-T60 segmented stent-graft.



Figure 3.8: Patient II CT images were characterised by a low resolution.

3.1.3 Patient III

Segmentation of Patient III endograft was actuated for the three available follow-up examinations: PIII-T1, PIII-T12 and PIII-T60. As in case of Patient II, endograft reconstruction was not as effective as we hoped. Segmentation of PIII-T1 device is shown in Figure 3.9. A non-satisfying result of PIII-T1 segmentation was probably caused by the presence of noise in CT images, as we illustrated in Figure 3.8 in the previous subsection.

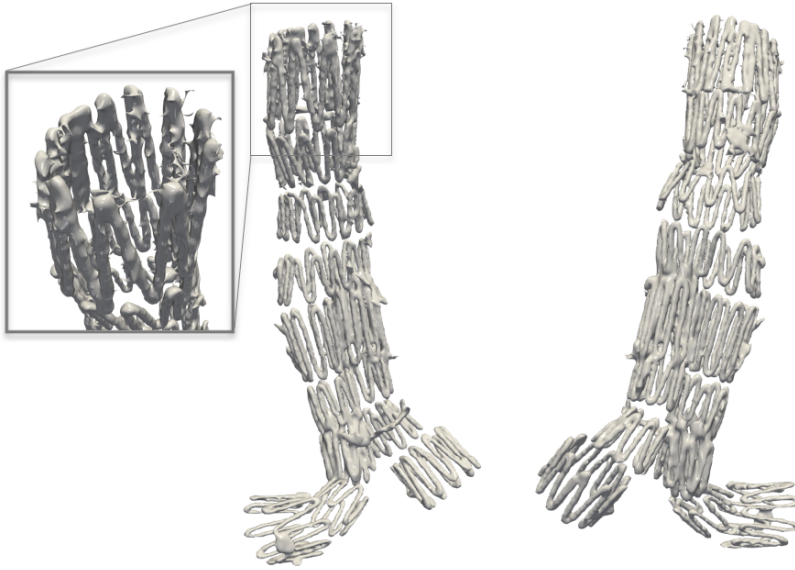


Figure 3.9: PIII-T1 segmented stent-graft.

Segmentation of stent-graft of PIII-T12 and PIII-T60 follow-ups, see Figure 3.10 and 3.11 respectively, provided a better result compared to PIII-T1 one, since no particularly relevant artifacts emerged.

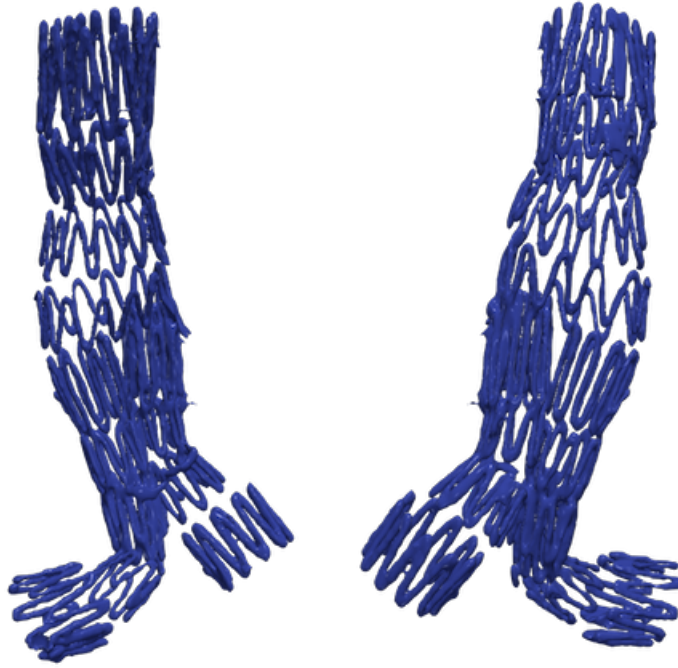


Figure 3.10: PIII-T12 segmented stent-graft.

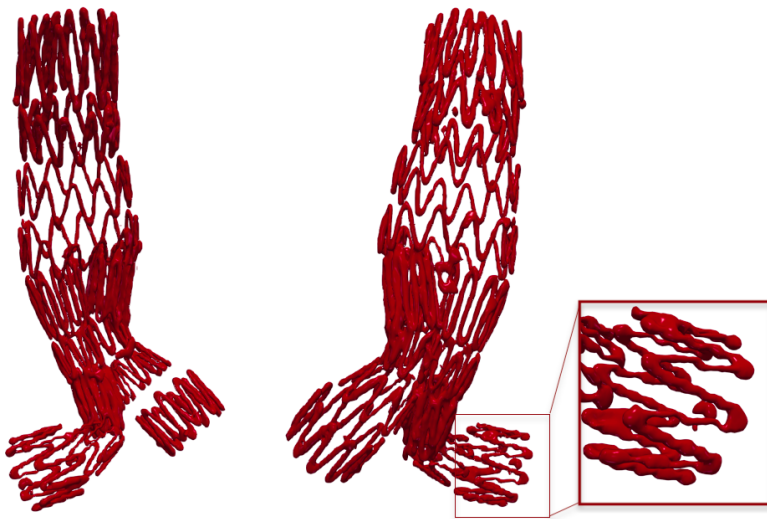


Figure 3.11: PIII-T60 segmented stent-graft.

3.2 Displacements over cardiac cycle

In this section we report results provided by applying Surface Distance algorithm available in VMTK to the ten 3D reconstruction of stent-graft for each patient and for

each follow-up. The computed displacements are graphically visualized through rainbow color maps. Rainbow color map is a standard in scientific visualization. The rainbow passes through five distinct colors (blue, cyan, green, yellow and red) and the colors visually separate the field into regions. We are specifically interested in portions of the surfaces where values are very high (low), i.e. red (blue) regions. As mentioned in Section 2.3.1, displacements are computed by applying the Signed Surface Distance algorithm implemented in VMTK: computed distance is positive if distance vector and normal to the reference surface have negative dot product, i.e. if the input surface is outer with respect to the reference surface. Therefore, positive values represent an outward stent-graft motion with respect to the reference position, whereas negative values an inward one.

3.2.1 Patient I

Patient I underwent three follow-up CT examinations (PI-T1, PI-T12 and PI-T48) so that we analysed dynamic behaviour of stent-graft for each of them. Figure 3.12 illustrates how endograft changes his position over cardiac cycle in PI-T1. We computed displacements between each of the nine time-instants graft surface and the reference surface, i.e. the seventh one representing diastolic peak. Systolic peak is reached at the third time instant. Our results are consistent with physiologic pulsation since higher values of displacements arised from movement analysis between diastolic and systolic peak, as qualitatively shows Figure 3.12. We highlight that endograft moved rigidly since opposite sides of the device are characterised by an opposite sign of displacements, i.e. posterior side is blue and anterior side is red. This proves that the stent-graft was not distorted or deformed in shape but it underwent to a rigid traslation.

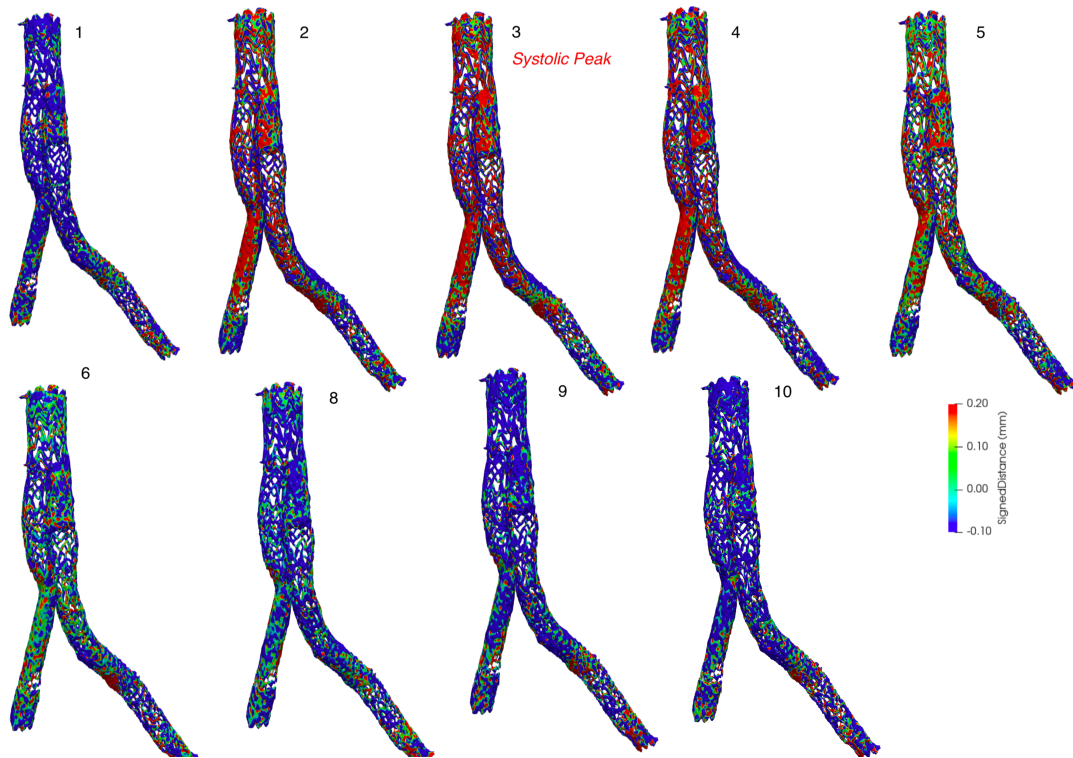


Figure 3.12: Nine displacements maps of Patient I endograft. Reference position is the seventh time-step corresponding to diastolic peak. We highlighted that third time-step is the systolic peak. Red color means that current surface is outer with respect to reference one, blue color represents inward surface motion.

Similar considerations may be applied to dynamic displacements occurred in PI-T12 and PinstantsI-T48 follow-up, see Figure 3.13 and 3.14 respectively.

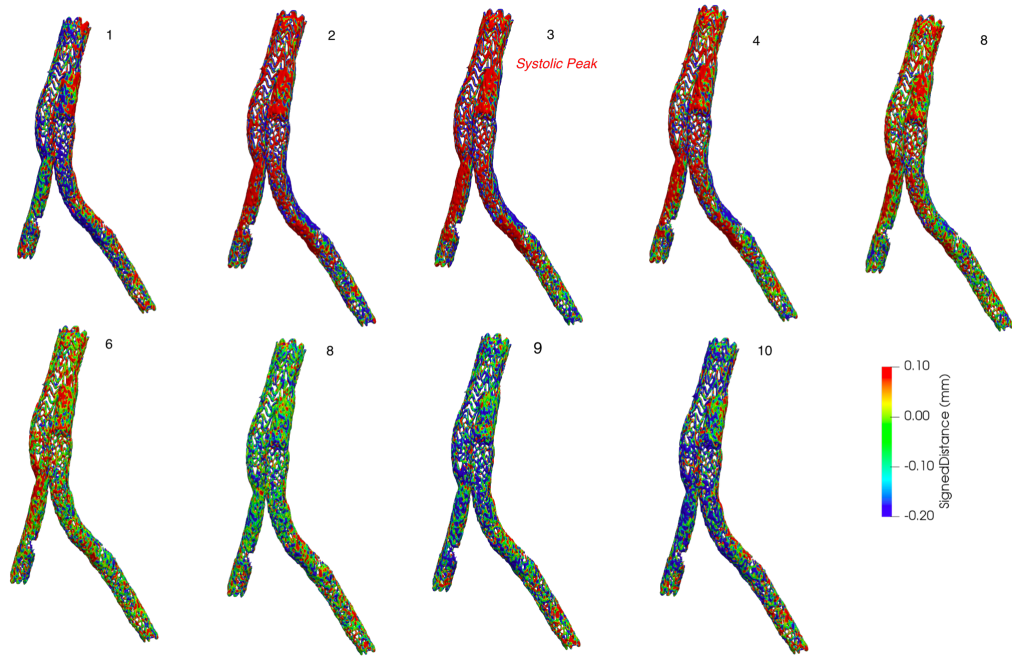


Figure 3.13: Dynamic motion of Patient I stent-graft during one heart beat.

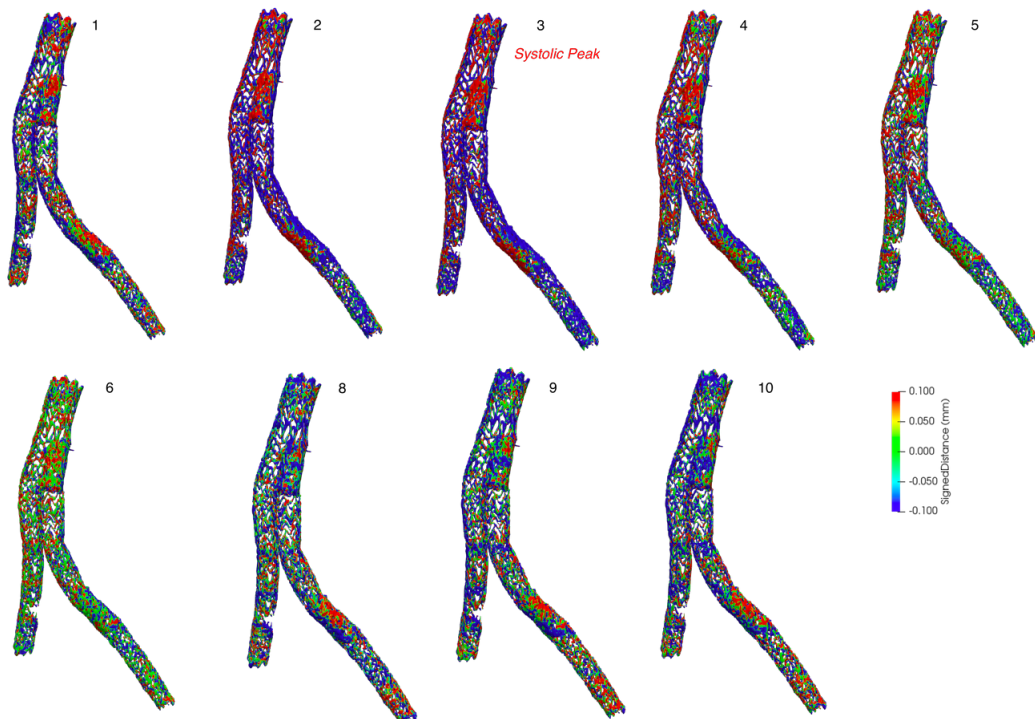


Figure 3.14: Nine color maps of PI-T48 graft displacements.

Table 3.1: Measurements of displacements peaks at four stent-graft portions.

	<i>Top</i>	<i>Mid</i>	<i>Bif</i>	<i>L.i.</i>
PI-T1	0.717mm	0.766mm	0.812mm	0.807mm
PI-T12	0.753mm	0.764mm	0.835mm	0.897mm
PI-T48	0.647mm	0.916mm	0.726mm	0.886mm

We could qualitatively assess that stent-graft displacements showed an anisotropic distributions. The highest positive values, describing outward motions with respect to diastolic configuration, are concentrated in four different parts, as Figure 3.15 shows: the most upper part on the device (*Top*), the bifurcation level at the right iliac side (*Bif*), the portion at the middle at right side (*Mid*) and an area of the left iliac leg (*L.i.*). At the systolic peak, displacements increase to lead maximum values. In Table 3.1 we report peaks of displacements occurred at systolic peak and concerning the four crucial regions in terms of displacements. We highlight that *L.i.* portion exhibits large outward motions (ranging from 0.807mm to 0.886mm) for all the three follow-ups PI-T1, PI-T12 and PI-T48 but the highest change in position concerns PI-T48 at *Mid* part (0.916mm).

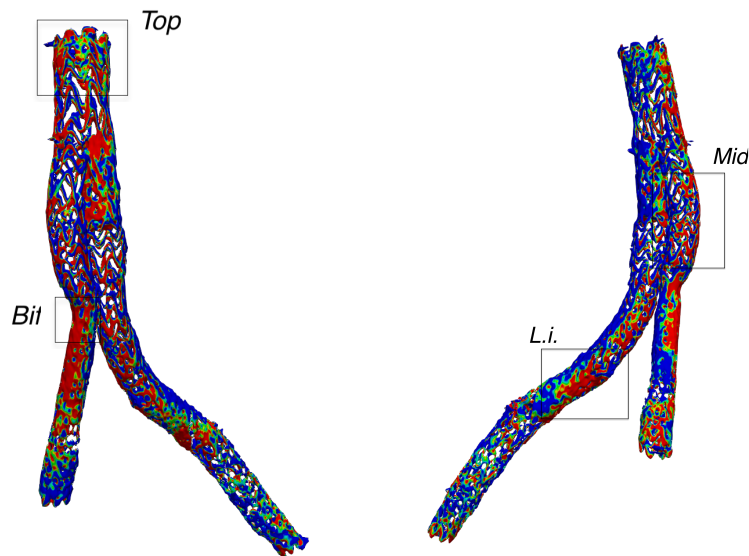


Figure 3.15: Definition of regions where we calculated displacements peaks.

3.2.2 Patient II and Patient III

Detection of endograft movements during cardiac cycle for Patient II Patient III did not provide effective results. Since low image resolution prevented to reconstruct smooth surfaces (see Section 3.2.1), displacements computation rendered a random dotted color

map. We may qualitatively assess that the order of magnitude of the displacements is similar to bumps dimensions resulted from the segmentation. For this reason an acceptable displacements distribution was not possible. Best result we could achieve concerns displacements between systolic and diastolic peak, as higher motion values occurred. Figure 3.16 shows PII-T12 dynamic case, where it is possible to notice that it is not easy to describe how device behaved. Another example of similar difficulties is

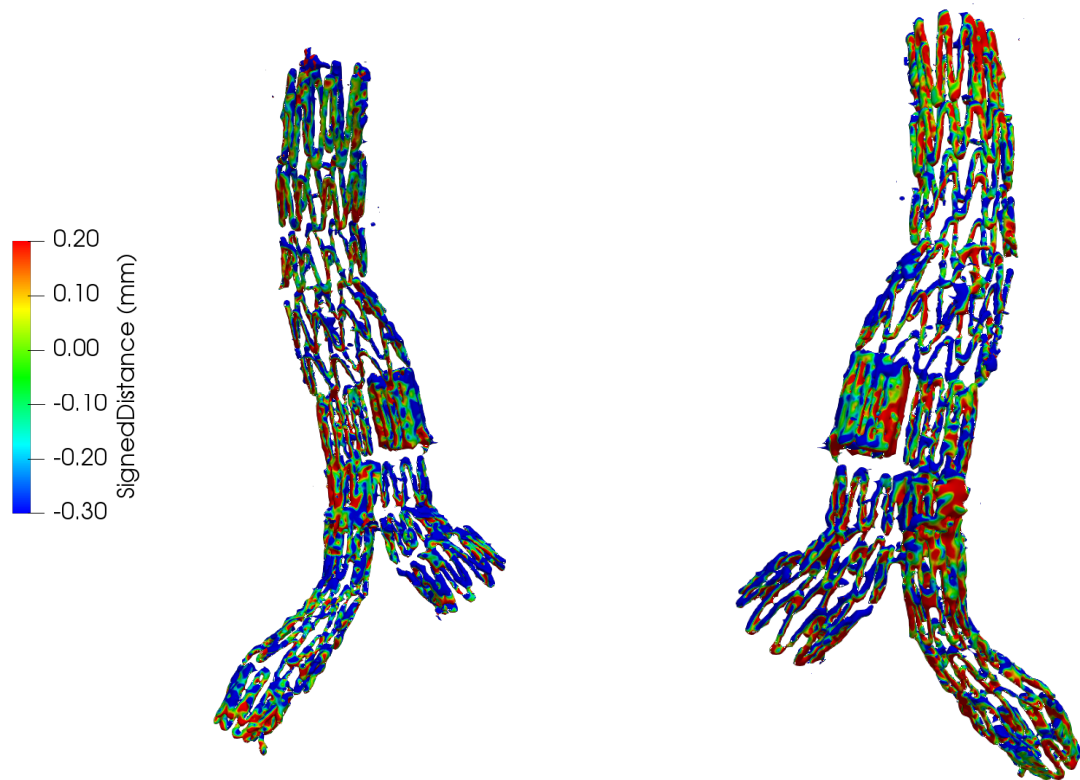


Figure 3.16: Dotted color map of PII-T12 displacements occurred between systolic and diastolic peak.

given in Figure 3.17. We highlight that the latter results are the products of several procedures aimed to improve surface quality. In VMTK we used `vmtksurfaceremeshing` and `vmtksurfacesmoothing` commands in order to have a less coarse triangularisation and a smoother surface. Therefore, not a significant improvement was obtained. In Figure 3.18 we show comparison between the original surface on the right and the smoothed surface with the increased number of cells on the left. It is possible to observe that after the improvement procedure we obtained a better detailed surface (from 280k cells to 447k) but this was not enough to find more reasonable displacements color map. In fact, before and after surfaces exhibited the same displacements distribution, i.e. the same color maps.

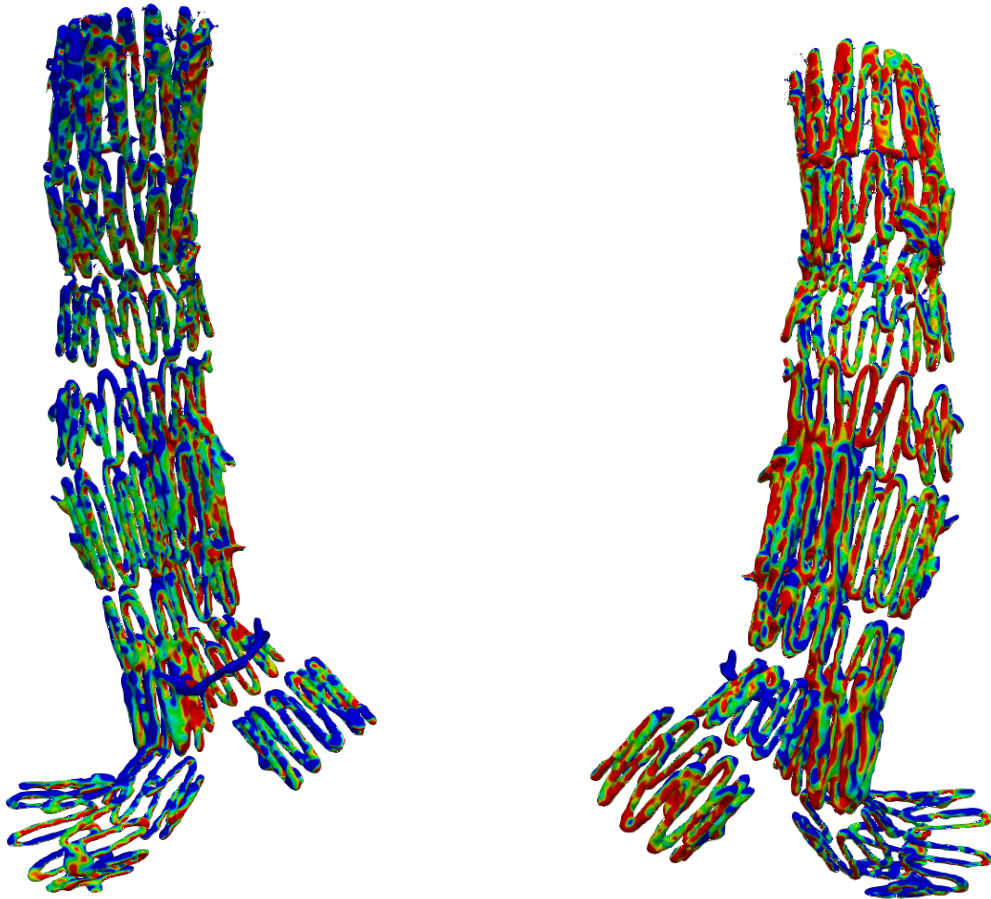


Figure 3.17: Dotted color map of PIII-T1 displacements occurred between systolic and diastolic peak.

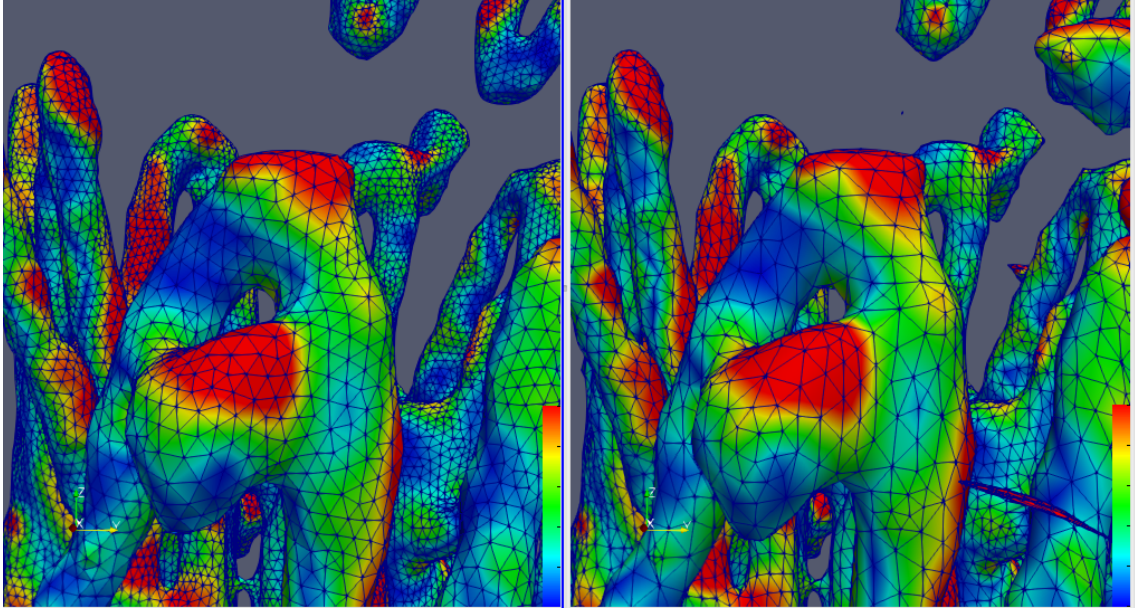


Figure 3.18: Comparison between PIII-T1 surfaces graft before and after remeshing and smoothing procedure. Number of cells increased from 280k to 447k, but color map did not significantly change.

3.3 Displacements between follow-ups

In this section we illustrate results of displacements analysis between two of the two or three available follow-up reconstructions for each patient. Distance between two surfaces are computed by applying the procedure described in the previous chapter.

3.3.1 Patient I

We computed displacements occurred between PI-T1 and PI-T12, PI-T12 and PI-T48 and between the first and the last follow-up, i.e. between T1 and T48. In Figure 3.19 the result of migration analysis performed in the first case is depicted. In particular, we reported stent-graft at T12 showing displacements with respect to PI-T1 graft, as well as both surfaces (PI-T1 in white and PI-T12 in blue). Overlapped setting is analysed in those portions where the color mapping revealed crucial behaviours. We highlighted that these peculiarities resulted to be at the higher part of the graft (*Top*), in the middle at bifurcation (*Bif*) and at the end of both of the iliac legs (*R.i.*, *Li.*). As done in case of displacements over cardiac cycle, we computed displacements peaks at the crucial stent-graft regions where the largest motions occurred. In Table 3.2 measurements obtained from this analysis are summed up. Changes in positions the two time intervals PI-T1-T12 and PI-T12-T48 are comparable for all the four sectors. The two iliac legs experienced larger motions, ranging between 3.18mm to 3.56mm, with respect to *Top*

(2.93mm in PI-T1-T12 and 2.49mm in PI-T12-T48) and *Bif* (2.43mm in PI-T1-T12 and 2.69mm in PI-T12-T48 regions. In particular, *L.i.* displacements revealed that this is the part mostly subjected to position variations, specially in PI-T1-T12 where we evaluated a motion of 3.56mm.

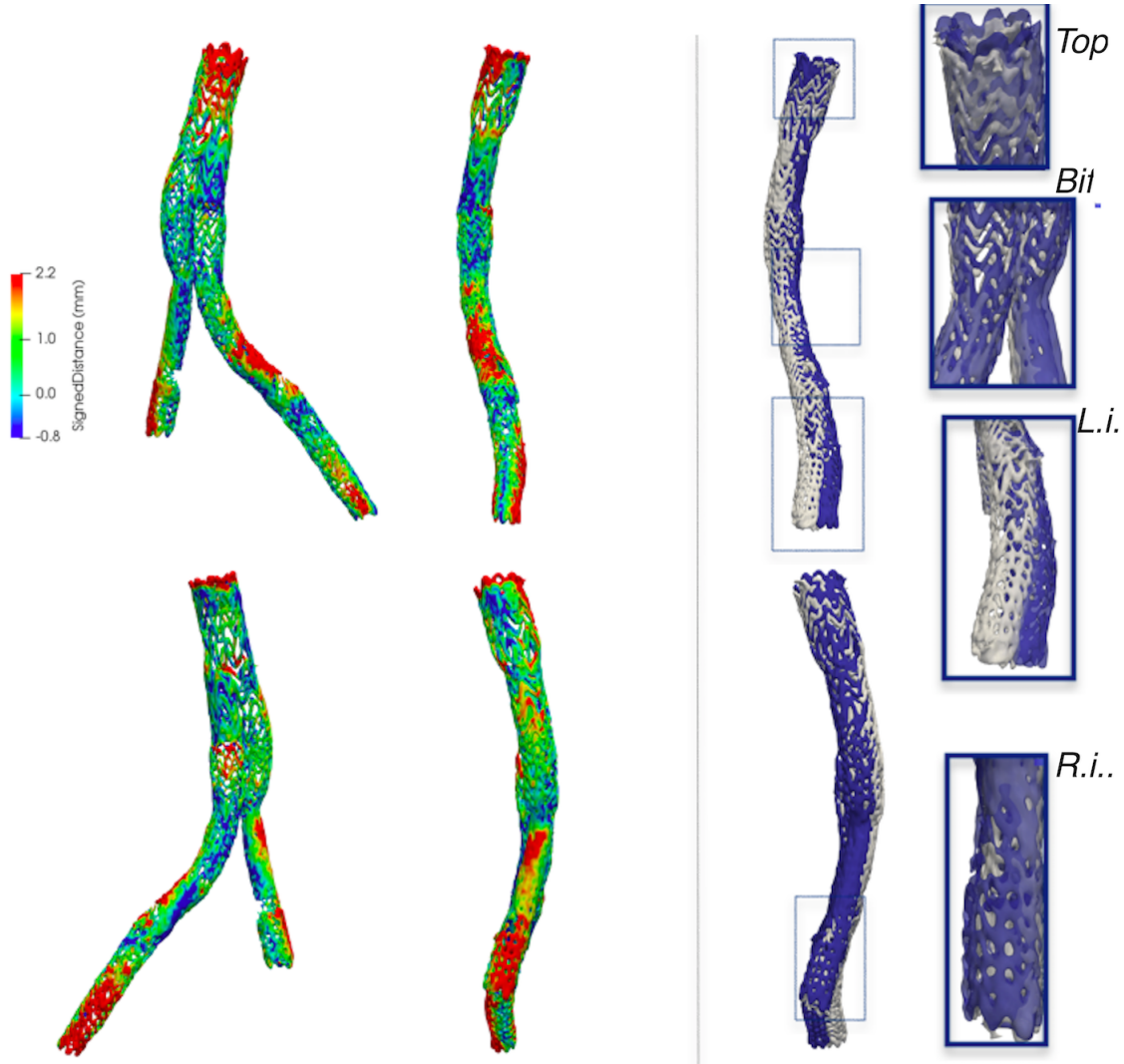


Figure 3.19: On the left, different views of the Patient I stent-graft showing the displacements occurred between PI-T1 and PI-T12 (antero-posterior and left views at the top, postero-anterior and right views on the bottom). Displacements were computed by using the Signed Surface Distance algorithm of VMTK. We considered PI-T12 as current surface and PI-T1 as reference surface. On the right, PI-T1 (white) and PI-T12 (blue) surfaces are overlapped in order to visualize both the endografts in the two follow-up analysis. Boxes enable a better observation of portions where displacements are higher.

Displacements computed between PI-T12 and PI-T48 are shown in Figure 3.19. Results are similar to those found in PI-T1-T12 case: bifurcation area (*Bif*) and distal part of both the iliac legs (*L.i.*, *R.i.*) are the portions characterised by higher values of

Table 3.2: Measurements of displacements peaks at four stent-graft portions, defined in Figure 3.19.

	<i>Top</i>	<i>Bif</i>	<i>L.i.</i>	<i>R.i.</i>
PI-T1-T12	2.93mm	2.43mm	3.56mm	3.19mm
PI-T12-T48	2.49mm	2.60mm	3.50mm	3.18mm
PI-T1-T48	3.91mm	5.72mm	8.01mm	5.02mm

displacements.

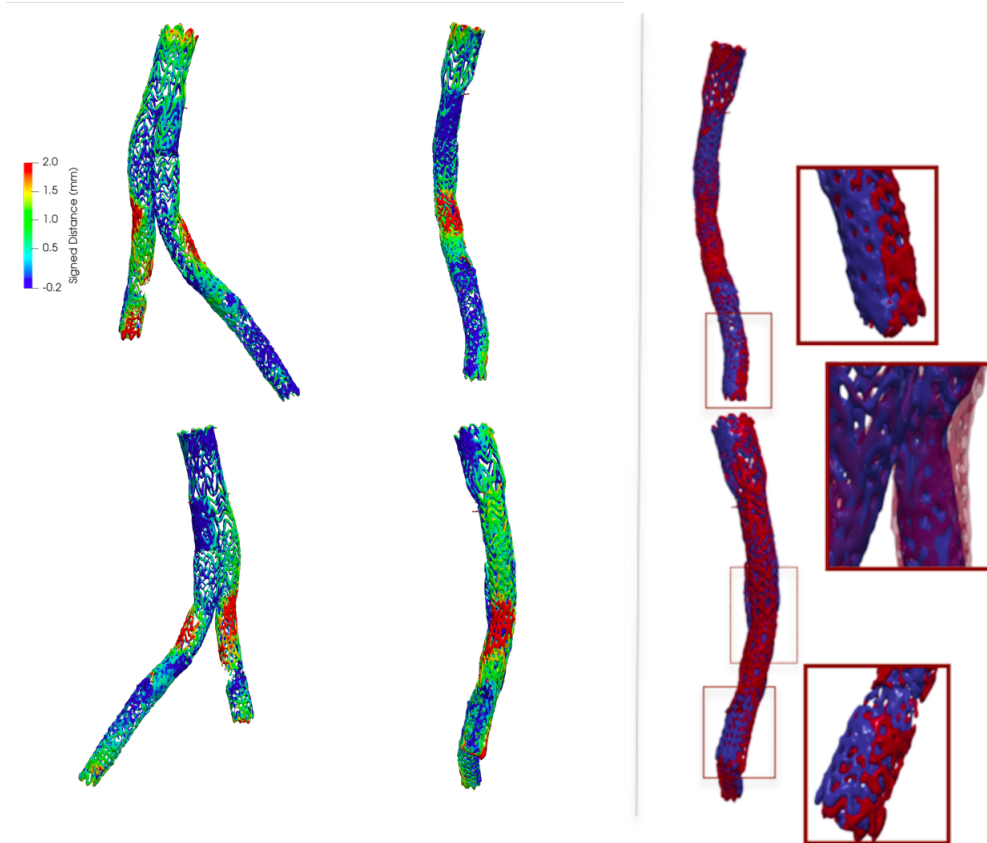


Figure 3.20: On the left, different views of the displacements occurred between PI-T12 and PI-T48 (antero-posterior and left views at the top, postero-anterior and right views on the bottom). Surface in PI-T48 configuration is shown and colors describe graft movement with respect to PI-T12 surface. On the right, overlapped surfaces, PI-T12 in blue and PI-T48 in red, enable to visualize at one blank both surfaces where color maps revealed peculiarities.

An overall view of how Patient I endograft behaved over the whole period of four years under surveillance has been analysed by computing displacements between first follow-up after EVAR, i.e. PI-T1, and the last one, i.e. PI-T48, see Figure 3.21. As shown by the scale, values of positive displacements are higher compared with the previous ones, as we could aspected. Portions where endograft exhibits higher values of displacements are coherent with ones detected in the two sub-steps (PI-T1-T12 and

PI-T12-T48). As we previously anticipated, right iliac leg at the level of graft bifurcation exhibited a significant dilation, but the highest values of displacements are located in correspondence of left iliac leg end, where we measured a motion of 8.01 mm.

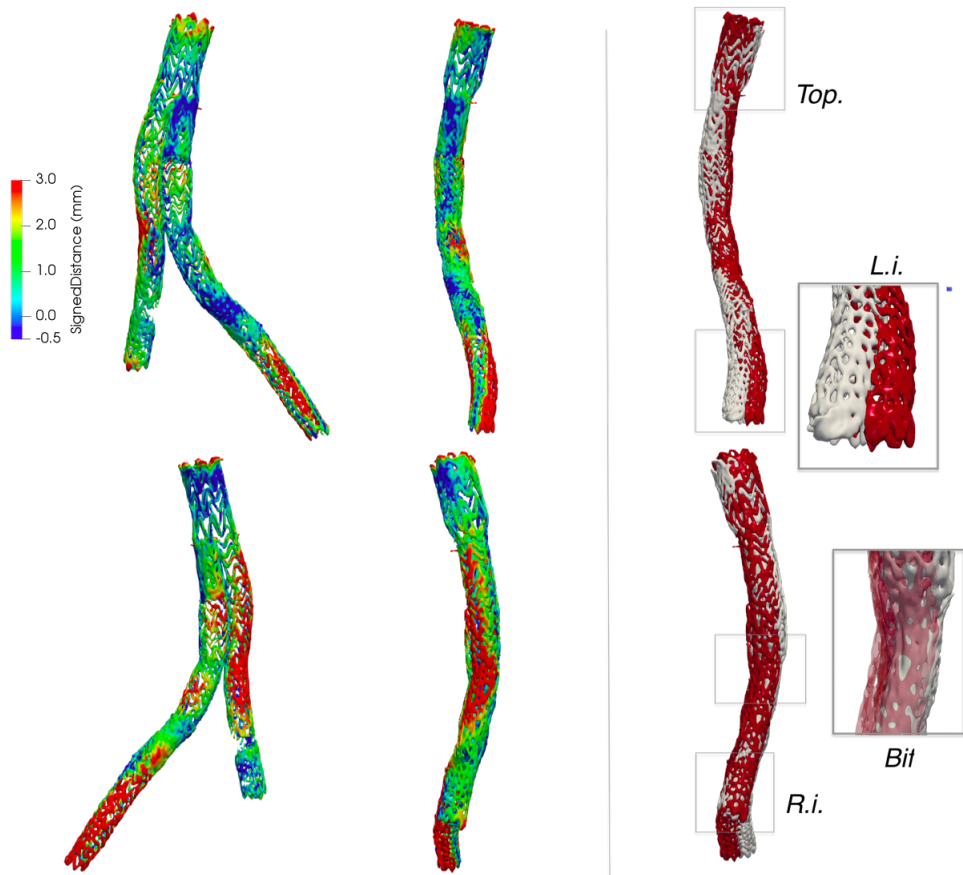


Figure 3.21: Overall displacements of endograft after four years from its deployment, namely displacements between PI-T1 and PI-T48. On the left, different views of the color mapped stent-graft (antero-posterior and left views at the top, postero-anterior and right views on the bottom), while on the right lateral views of PI-T1 (in white) overlapped over PI-T48 (in red) in order to better visualize the regions where the largest displacements occurred.

3.3.2 Patient II

In Section 3.2.2 we discussed the problems we faced to compute displacements of stent-graft over cardiac cycle in case of Patient II and III due to the combination of low contrast resolution of CT images and small displacements. The latter were characterised by an order of magnitude similar to the bumps of the surface. However, changes in position of the device occurring over time-intervals of several months are significantly larger and larger motion ranges make the artifacts insignificant. We had available two follow-up examinations, one year (PII-T12) and sixty months (PII-T60) post-EVAR.

Table 3.3: Measurements of displacements peaks at three Patient I stent-graft portions for PII-T12-T60 time interval. Location of *Top*, *Bif* and *Li* are visualized in Figure 3.22

	<i>Top</i>	<i>Bif</i>	<i>Li</i>
PIIT12-T60	3.89mm	3.76mm	3.64mm

Hence, in this case, we had to analyse only one time interval. We applied Surface Distance algorithm, as described in the previous chapter, and computed the stent-graft displacements. In Figure 3.22 resulting surfaces are shown. By using a proper scale, we detect several regions where endograft underwent greater movements. These are located at the distal ends of iliac legs, at the top part and at bifurcation. in Table 3.3 measurements of stent-graft displacements are reported for three portions where motion was believed significant in the light of color maps. By observing bifurcation and top sites, we noticed that upper part of the stent slid down, while both iliac branches did not exhibit such downwards migration, but a dilation.

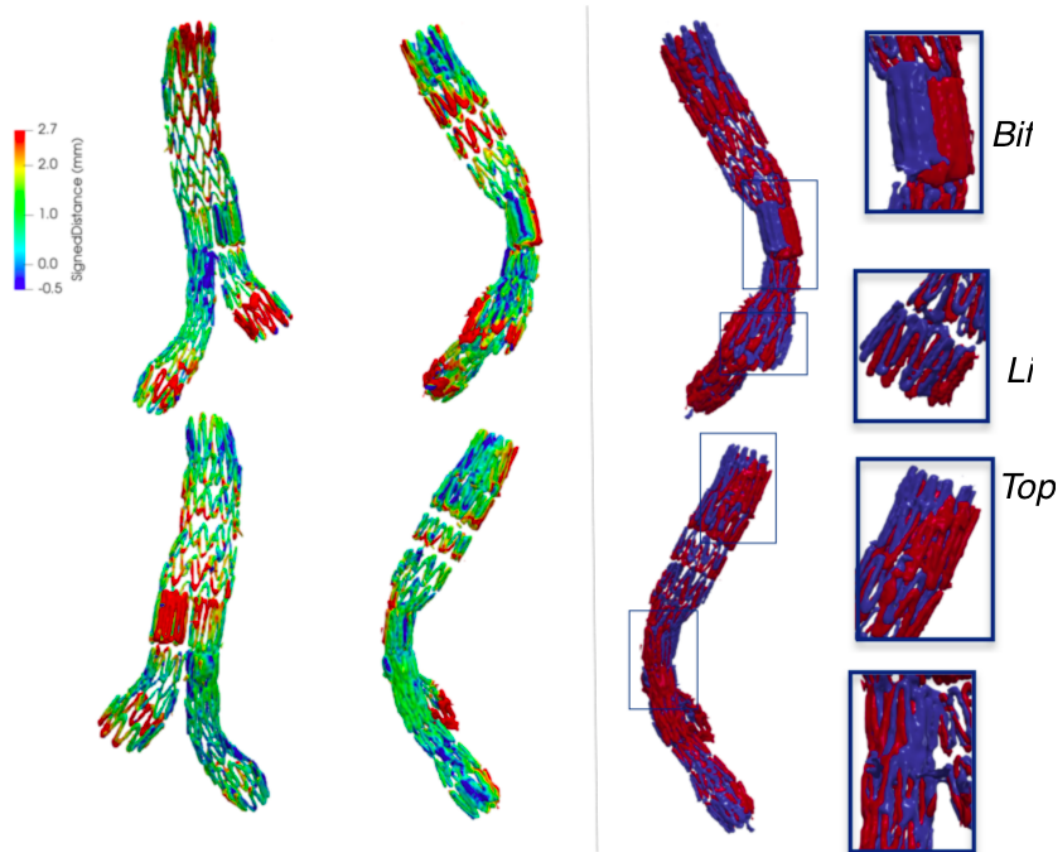


Figure 3.22: Different views of Patient II color mapped device revealing the distance computed from each point of PII-T12 surface to corresponding points of PII-T60. On the right we highlighted the regions where displacements are higher by overlapping PII-T12 surface (blue) and PII-T60 surface (red) in order to easily visualize changes in position.

Table 3.4: Measurements of displacements peaks at three Patient III stent-graft portions for each follow-up, defined in Figure 3.23.

	<i>Bif</i>	<i>Li1</i>	<i>Li2</i>
PIII-T1-T12	6.48mm	1.50mm	4.38mm
PIII-T12-T60	5.57mm	6.70mm	3.52mm
PIII-T1-T60	8.15mm	5.16mm	6.08mm

3.3.3 Patient III

Even if we did not achieve effective results in the analysis of displacements over cardiac cycle, we were able to identify stent-graft displacements of Patient III between the different follow-ups, as for Patient II (see the previous section). Patient III underwent three follow-up exams after stent-graft deployment: after one month (PIII-T1), twelve months (PIII-T12) and sixty months (PIII-T60). Hence, we computed stent-graft displacements occurred between PIII-T1 and PIII-T12, PIII-T12 and PIII-T60, as well as the total migration from PIII-T1 to PIII-T60. In Figure 3.23 results about how endograft behaved during first time interval, that is from PIII-T1 and PIII-T12, are reported. Distance point-to-point was computed considering PIII-T12 graft as current surface and PIII-T1 as the reference one. From these results we could noticed a considerable change in graft conformation at bifurcation area: in this part wires opened and dilated, mostly in the posterior side. In Table 3.4 we reported displacements for each time interval concerning three portions of the endograft, evaluated as the most interesting in terms of position variations. Endograft tendency to open up and expand kept even in the second time interval from PIII-T12 to PIII-T60, see Figure 3.25 where PIII-T60 graft is depicted with color map concerning displacements with respect to PIII-T12 surface. It is important to notice that overall change in position of stent wires occurred axially, especially towards dorsal side, and did not lead to a downward migration.

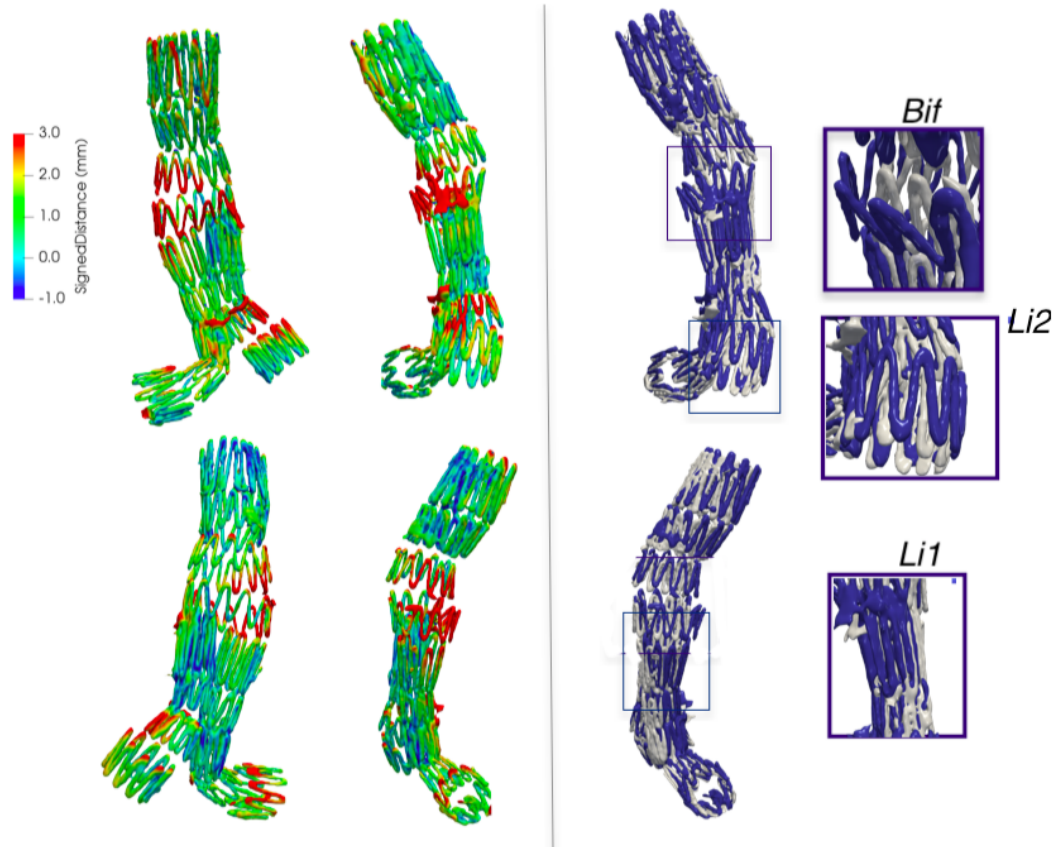


Figure 3.23: Stent-graft showing displacements occurred from PIII-T1 to PIII-T12. On the left, colour mapped surfaces, represented from different points of view (postero-anterior and right views at the top, antero-posterior and left views on the bottom), result from Surface Distance algorithm of VMTK, while on the right PIII-T1 (white) and PIII-T12 (blue) surfaces are overlapped in order to visualize both of the endografts in the two follow-up analysis.

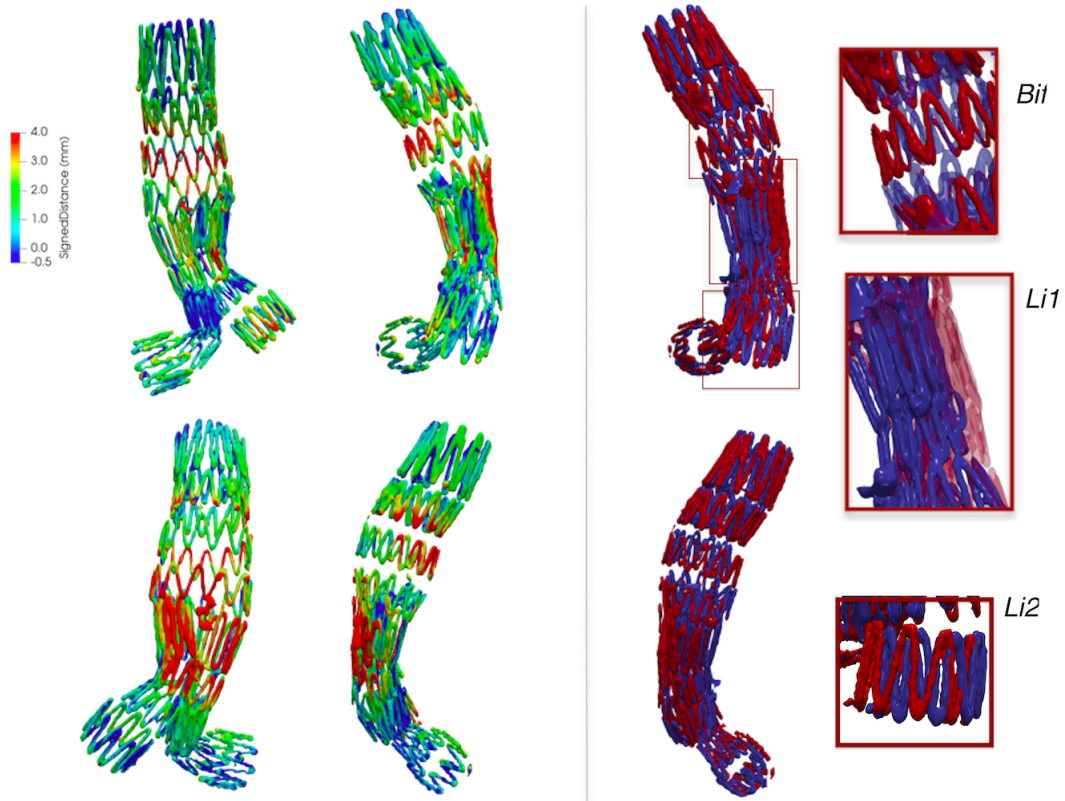


Figure 3.24: Displacements of stent-graft between second and third follow-up, i.e. between PIII-T12 and PIII-T60. On the left, coloured surfaces represent stent-graft in PIII-T60 configurations from different points of view (postero-anterior and right views at the top, antero-posterior and left views on the bottom), and describe displacements computed with respect to PIII-T12 surface. On the right, overlap of both configurations, PIII-T12 in blue and PIII-T60 in red, enables to analyse stent-graft portions which resulted to be critical in the coloured visualization.

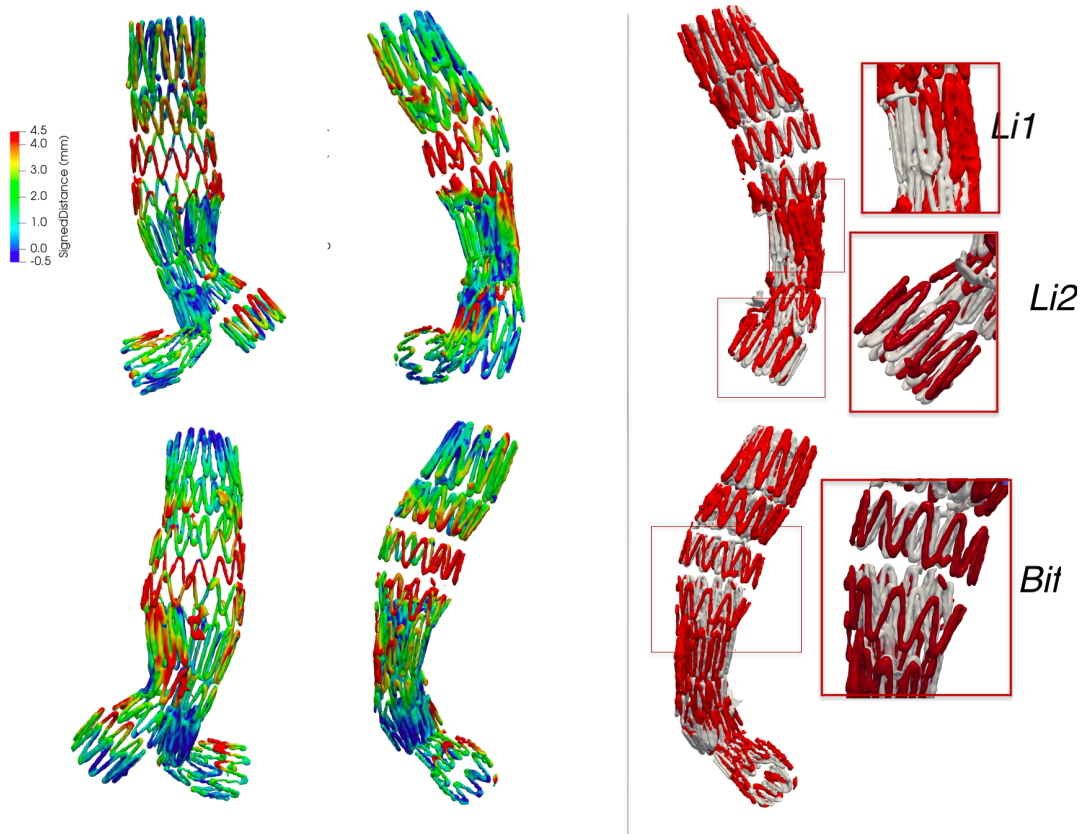


Figure 3.25: Overall displacements stent-graft between PIII-T1 and PIII-T60. Coloured surfaces represent stent-graft in PIII-T60 configurations from different points of view (postero-anterior and right views at the top, antero-posterior and left views on the bottom) and describe displacements computed with respect to PIII-T1 surface.

Chapter 4

Mathematical and numerical methods

4.1 Models for blood

In this section we want to exploit the rheological properties of blood in order to provide a suitable mathematical modelization of blood flow and its numerical approximation.

Firstly, we briefly describe the classification of fluids on the basis of the different behaviour of the shear stress-shear rate relation (see Figure 4.1):

- Newtonian fluid: the relationship between shear rate and shear stress is linear and the slope of the line describing this relation is equal to 2μ , where μ is the fluid viscosity.
- Dilatant fluid: non-Newtonian fluid in which the apparent viscosity, i.e. the ratio between shear stress and shear rate, increases with the shear rate. The resulting curve is convex.
- Pseudoplastic fluid: non-Newtonian fluid in which the apparent viscosity decreases when the shear rate increases. The shear stress-shear rate curve is concave.
- Bingham plastic fluid: the shear stress and shear rate are linearly dependent as in case of Newtonian fluid. however a Bingham plastic fluid does not exhibit any shear rate until a certain value of shear stress is achieved.

Blood is a two-phase suspension of formed elements, i.e. red blood cells, white blood cells (RBCs), platelets suspended in an aqueous solution of organic molecules, proteins and salts called plasma. Physical properties of blood depend on hematocrit, plasma viscosity, RBCs aggregation and their mechanical properties. Since RBCs compose about 40 to 45 % of the blood volume, they are the most important factor for the mechanical properties of blood. RBCs are biconcave disks about $8 \mu\text{m}$ in diameter and $2 \mu\text{m}$ thick. Applied forces make cells changing their shape and since they behave as elastic bodies,

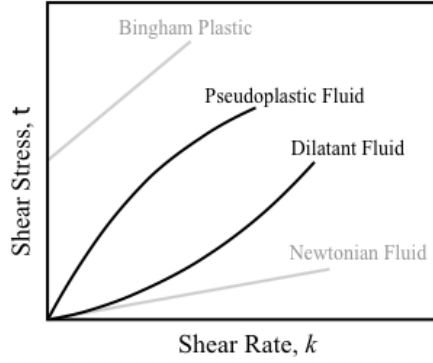


Figure 4.1: The shear stress-shear rate relations of Newtonian, dilatant, pseudoplastic and Bingham pseudoplastic fluids.

the shape change is reversible when deforming forces are removed. High deformability is due to the absence of a nucleus, to the elastic and viscous properties of their membrane and to the geometric factors. RBCs tend to aggregate into linear arrays, called rouleaux, at low shear forces conditions. These 3D structures resist flow until a finite level of force is applied. The developed aggregates are dispersed with increasing shear forces. This phenomena is the major determinant of blood viscosity. RBC aggregation tendency can be modified by alterations of RBC surface properties because of aging, oxygen-free radicals or proteolytic enzymes. For all the discussed phenomena, blood behaves as a non-Newtonian fluid, particularly at low shear stress rates. However, since large arteries, such as the abdominal aorta, have a diameter dimension which differs of more than two order of magnitude with respect to the dimension of RBCs, we can consider blood as a Newtonian fluid. In addition, even if in a real scenario deformability of RBCs induce blood density changes. we assume blood as an incompressible fluid, i.e. with a constant density. A further assumption we make is to consider blood solid components with a negligible dimension so to assume blood as an homogeneous fluid.

In order to better analyse blood flow behaviours we now define the Reynold's number:

$$Re = \frac{\text{inertial forces}}{\text{viscous forces}} = \frac{uD\rho}{\mu} \quad (4.1.1)$$

where u is the velocity of the fluid, D is the characteristic dimension of the vessel (such as the diameter), ρ is the density of the fluid and μ the viscosity. This number allows to predict the flow pattern of the fluid: the flow is laminar if Re is below 2000 while the flow is turbulent if it is greater than 2000. Reynold's number in the case of abdominal aorta is greater than 2000, as we will report in the Chapter 5 in Table 5.2, hence transition to turbulence could occur, see [38]. However, in our mathematical modeling we always assume a laminar flow for the sake of simplicity.

In the following subsections we will discuss the mathematical model of a Newtonian, incompressible and homogeneous fluid and its numerical approximation.

4.2 The Navier-Stokes equations

Blood fluid dynamics in large vessels is modeled with the incompressible Navier-Stokes equations. They were developed by Navier in 1831 and more rigorously by Stokes in 1845. The equations can be derived from the basic conservation and continuity equations applied to properties of fluids.

First basic assumption is that of **Reynold's Transport Theorem**. Let f be a differentiable function and call \mathbf{u} the velocity of the area element of V_t and

$$\frac{Df}{Dt} := \partial_t f + \mathbf{u} \cdot \nabla f$$

its Lagrangian derivative. Then we denote with Ω_t the domain occupied by the fluid at time t and with $V_t \subset \Omega_t$ the material volume at time t . Then Reynolds theorem states that

$$\begin{aligned} \frac{d}{dt} \int_{V_t} f(x) dx &= \int_{V_t} \left(\frac{Df}{Dt} + \mathbf{u} \cdot \nabla f \right) = \int_{V_t} (\partial_t f + \nabla \cdot (f\mathbf{u})) \\ &= \int_{V_t} \partial_t f + \int_{\partial V_t} f(z)\mathbf{u}(z) \cdot \mathbf{n}(z) d\Sigma(z) , \end{aligned}$$

where the second equality just follows from Leibniz formula and the third one from divergence theorem that we briefly recall: if $f : \Omega \rightarrow \mathbb{R}$ and $\mathbf{g} : \Omega \rightarrow \mathbb{R}^d$ are smooth functions,

$$\int_{\Omega} \mathbf{g} \cdot \nabla f = - \int_{\Omega} f \nabla \cdot \mathbf{g} + \int_{\partial\Omega} f \mathbf{g} \cdot \mathbf{n} .$$

A consequence of this is **continuity equation**: this will reflect the principle that matter may neither be created nor destroyed. In particular, from its definition, mass in V_t is constant, so that, by denoting $\rho : \mathbb{R}_+ \times \Omega_t \rightarrow \mathbb{R}_+$ the density of the fluid, we have that

$$0 = \partial_t \int_{V_t} \rho = \int_{V_t} (\partial_t \rho + \nabla \cdot (\rho\mathbf{u})) .$$

We may now take V_t arbitrarily small and centered about an arbitrary point to localize the last integral equation to the pointwise one

$$0 = \partial_t \rho + \nabla \cdot (\rho\mathbf{u})$$

which is the well known continuity equation. As we said in the previous section we

consider blood as incompressible, hence density is constant, giving

$$\nabla \cdot \mathbf{u} = 0$$

One may also notice that we could reach this property by simply applying Reynolds theorem to $f \equiv 1$, but we wanted to show the derivation of the classical continuity equation.

Let us now try to extend **Newton's second law**

$$\mathbf{F} = m\mathbf{a}$$

to a continuous medium as our fluid: the generalization of the right hand side we give is time derivative of the momentum, that is,

$$\frac{d}{dt} \int_{V_t} \rho \mathbf{u} ,$$

while forces may be decomposed in forces acting on the volume and those acting on the surface:

- *Body forces*: these are the forces proportional to the mass, such as the gravity force. If $\mathbf{f}_V : I \times \Omega_t \rightarrow \mathbb{R}^3$ is the specific body force, the overall body force acting on a volume V_t is given by

$$\int_{V_t} \rho \mathbf{f}_V dV \tag{4.2.1}$$

- *Applied surface forces*: they are forces applied on the surface and represented by means of the vector field called applied stresses $\mathbf{f}_\Sigma : I \times \Gamma_t^n \rightarrow \mathbb{R}^3$ where $\Gamma_t^n \subset \delta\Omega_t$. Therefore the surface force is defined as

$$\int_{\Gamma_t^n} \mathbf{f}_\Sigma d\Sigma \tag{4.2.2}$$

giving rise to

$$\frac{d}{dt} \int_{V_t} \rho \mathbf{u} = \int_{V_t} \rho \mathbf{f}_V + \int_{\partial V_t} \mathbf{f}_\Sigma .$$

We now assume that external forces may be written as

$$\mathbf{f}_\Sigma = \mathbf{t} : \mathbb{R}_+ \times \Omega \times S^2 \rightarrow \mathbb{R}^3 ,$$

where the last argument is the outer unit vector lying on the sphere S^2 . Also, Cauchy

stress tensor theorem makes sure that there exists a C^1 symmetric matrix field

$$\mathbf{T} : \mathbb{R}_+ \times \bar{\Omega} \rightarrow \mathbb{R}^{3 \times 3}$$

such that

$$\mathbf{t}(t, x, n) = \mathbf{T}(t, x) \cdot n, \quad t > 0, \quad x \in \Omega, \quad n \in S^2.$$

By combining continuity and momentum equations we may therefore write

$$\begin{aligned} \int_{V_t} \partial_t(\rho \mathbf{u}) + \int_{V_t} \mathbf{u} \cdot \nabla(\rho \mathbf{u}) &= \int_{V_t} \partial_t(\rho \mathbf{u}) + \nabla \cdot (\rho \mathbf{u} \otimes \mathbf{u}) = \partial_t \int_{V_t} \rho \mathbf{u} \\ &= \int_{V_t} \rho \mathbf{f}_V + \int_{\partial V_t} \mathbf{T} \cdot n = \int_{V_t} \rho \mathbf{f}_V + \int_{V_t} \nabla \cdot \mathbf{T} \end{aligned}$$

thanks to \mathbf{u} being divergence-free in the first equality and to divergence theorem – applied to $f \equiv 1$ – in the last one. This is clearly an equality of vectors, and it is easy to prove it component by component by applying usual tools. In our notation scalar operators such as gradient are to be thought as naturally extended to their vector version, and by $\mathbf{u} \otimes \mathbf{u}$ we mean the tensor product $(\mathbf{u} \otimes \mathbf{u})_{ij} := u_i u_j$. As previously done when proving continuity equation, this integral equation may be localized into

$$\partial_t(\rho \mathbf{u}) + \mathbf{u} \cdot \nabla(\rho \mathbf{u}) = \rho \mathbf{f}_V + \nabla \cdot \mathbf{T}.$$

By relabelling \mathbf{f}_V into \mathbf{f} and reminding that the fluid is incompressible, we yield

$$\rho \partial_t \mathbf{u} + \rho \mathbf{u} \cdot \nabla \mathbf{u} - \rho \mathbf{f} = \nabla \cdot \mathbf{T}. \quad (4.2.3)$$

We now just need to know the following fact: since the fluid is Newtonian incompressible, the matrix field \mathbf{T} has the form

$$\mathbf{T} = -P\mathbf{I} + \mu(\nabla \mathbf{u} + (\nabla \mathbf{u})^T)$$

for some smooth scalar function $P : \Omega \rightarrow \mathbb{R}$ called pressure and real constant μ . Of course the last term is the transposed matrix of the Jacobian of \mathbf{u} , which gives rise to the symmetrization of the matrix itself. Let us now deal with the divergence: when on each single component it acts on the gradient of a scalar component of \mathbf{u} it gives rise to a Laplacian, while when it acts on a partial derivative of \mathbf{u} it gives rise to a partial derivative of $\nabla \cdot \mathbf{u}$, that we know to be null. More formally

$$\begin{aligned} \nabla \cdot \mathbf{T} &= -\nabla \cdot (P\mathbf{I}) + \mu(\nabla \cdot \nabla \mathbf{u} + \nabla \cdot (\nabla \mathbf{u})^T) \\ &= -\nabla P + \mu(\Delta \mathbf{u} + \nabla(\nabla \cdot \mathbf{u})) = -\nabla P + \mu \Delta \mathbf{u}, \end{aligned}$$

which when plugged in Eq. (4.2.3) gives

$$\rho \partial_t \mathbf{u} + \rho \mathbf{u} \cdot \nabla \mathbf{u} - \rho \mathbf{f} = -\nabla P + \mu \Delta \mathbf{u} .$$

The sought equation is basically achieved; we just divide it by ρ and call $p := \frac{P}{\rho}$, $\nu := \frac{\mu}{\rho}$, which is the kinematic viscosity, to yield the more classical writing

$$\partial_t \mathbf{u} + \mathbf{u} \cdot \nabla \mathbf{u} + \nabla p - \nu \Delta \mathbf{u} = \mathbf{f} .$$

The system of continuity equation and this last momentum equation gives Navier-Stokes equations for an incompressible fluid:

$$\begin{cases} \partial_t \mathbf{u} + \mathbf{u} \cdot \nabla \mathbf{u} + \nabla p - \nu \Delta \mathbf{u} = \mathbf{f} \\ \nabla \cdot \mathbf{u} = 0 \end{cases}$$

for $t > 0$, $x \in \Omega$ where $\Omega \subset \mathbb{R}^d$ is some given domain – in our case $d = 3$. \mathbf{f} is given and the two unknowns are $\mathbf{u} : \Omega \rightarrow \mathbb{R}^3$ and $p : \Omega \rightarrow \mathbb{R}$. In hemodynamics we suppose $\mathbf{f} = 0$, since the only external force acting on blood is gravity, which is negligible. Let us now focus on well-posedness of the problem: such issue is existence and uniqueness of a solution, at least for short time. In our case unknowns are four – three components of \mathbf{u} and the scalar function p . As often done with time-dependent partial differential equations, we shall prescribe behaviour at initial time: given $\mathbf{u}_0 : \Omega \rightarrow \mathbb{R}^3$, we ask for

$$\mathbf{u}(0, x) = \mathbf{u}_0(x) , \quad x \in \Omega .$$

Concerning boundary conditions, we shall partition $\partial\Omega$ in Γ_D and Γ_N on which we pose respectively Dirichlet and Neumann condition: given $\phi : \mathbb{R}_+ \times \Gamma_D \rightarrow \mathbb{R}^3$ and $\psi : \mathbb{R}_+ \times \Gamma_N \rightarrow \mathbb{R}^3$ we ask for

$$\begin{cases} \mathbf{u}(t, x) = \phi(t, x) & (t, x) \in \mathbb{R}_+ \times \Gamma_D \\ \nu \frac{\partial \mathbf{u}}{\partial \mathbf{n}}(t, x) - p \mathbf{n}(x) = \psi(t, x) & (t, x) \in \mathbb{R}_+ \times \Gamma_N \end{cases} .$$

4.3 The weak formulation

Well-posedness of this system is still an open problem in \mathbb{R}^3 , so we shall revert to its weak formulation: while the former Navier-Stokes equations are expressed in terms of pointwise value of the solution – giving rise to the so-called classical solutions – weak formulation of a problem is just asking the solution to only meet some requirements which are properties of classical solutions. Of course weak solutions do not need to be

classical solutions, but they retain main properties of the equation even though they need less regularity properties than classical solutions. Namely we pick the equation satisfied by a classical solution \mathbf{u} , multiply it times an arbitrary function \mathbf{v} and integrate it over space. \mathbf{v} will be required from step to step to have further properties, but for the moment it will just be asked to be smooth – and decaying rapidly enough, if on an unbounded domain. We therefore have

$$\begin{aligned} 0 &= \int_{\Omega} \partial_t \mathbf{u} \cdot \mathbf{v} - \nu \int_{\Omega} \Delta \mathbf{u} \cdot \mathbf{v} + \int_{\Omega} \mathbf{u} \cdot \nabla \mathbf{u} \cdot \mathbf{v} + \int_{\Omega} \nabla p \cdot \mathbf{v} \\ &= \int_{\Omega} \partial_t \mathbf{u} \cdot \mathbf{v} + \nu \int_{\Omega} \nabla \mathbf{u} \cdot \nabla \mathbf{v} - \nu \int_{\partial\Omega} \mathbf{v} \cdot \nabla \mathbf{u} \cdot \mathbf{n} + \int_{\Omega} \mathbf{u} \cdot \nabla \mathbf{u} \cdot \mathbf{v} \\ &\quad - \int_{\Omega} p \nabla \cdot \mathbf{v} + \int_{\partial\Omega} p \mathbf{v} \cdot \mathbf{n} \quad . \end{aligned}$$

Now let us be more precise on the choice of the test function \mathbf{v} ; namely we shall ask it to have the first weak gradient integrable and to be null on Γ_D . More precisely the function space is $H_{\Gamma_D,0}^1(\Omega)$, where

$$H_{\Gamma_D,\phi}^1(\Omega) := \{ \mathbf{v} \in [L^2(\Omega)]^3 : \nabla \mathbf{v} \in [L^2(\Omega)]^{3 \times 3}, \mathbf{v}|_{\Gamma_D} = \phi \} , \quad (4.3.1)$$

where the gradient is to be meant weakly. The previous equation therefore becomes

$$\begin{aligned} 0 &= \int_{\Omega} \partial_t \mathbf{u} \cdot \mathbf{v} + \nu \int_{\Omega} \nabla \mathbf{u} \cdot \nabla \mathbf{v} - \nu \int_{\Gamma_N} \mathbf{v} \cdot \nabla \mathbf{u} \cdot \mathbf{n} + \int_{\Omega} \mathbf{u} \cdot \nabla \mathbf{u} \cdot \mathbf{v} \\ &\quad - \int_{\Omega} p \nabla \cdot \mathbf{v} + \int_{\Gamma_N} p \mathbf{v} \cdot \mathbf{n} \\ &= \int_{\Omega} \partial_t \mathbf{u} \cdot \mathbf{v} + \nu \int_{\Omega} \nabla \mathbf{u} \cdot \nabla \mathbf{v} + \int_{\Omega} \mathbf{u} \cdot \nabla \mathbf{u} \cdot \mathbf{v} - \int_{\Omega} p \nabla \cdot \mathbf{v} - \int_{\Gamma_N} \psi \cdot \mathbf{n} \end{aligned}$$

by applying Neumann condition. Concerning continuity equation, we shall argue rather easily: pick $w \in L^2(\Omega)$ and multiply times the equation, yielding

$$\int_{\Omega} w \nabla \cdot \mathbf{u} = 0 .$$

We now just have to impose Dirichlet condition and initial data: to this scope we shall simply look for \mathbf{u} such that $\mathbf{u}(t, \cdot)|_{\Gamma_D} = \phi(\cdot)$ for all t and $\mathbf{u}(0, \cdot) = \mathbf{u}_0(\cdot)$. We may summarize everything by stating that the weak formulation of Navier-Stokes equations for an incompressible fluid in $\Omega \subset \mathbb{R}^3$, with initial data $\mathbf{u}_0 \in H^1(\Omega)$, Dirichlet condition of ϕ on Γ_D and Neumann condition of ψ on Γ_N amounts to finding \mathbf{u} , such that for almost every t , $\mathbf{u} \in [H_{\Gamma_D,\phi}^1(\Omega)]^3$, accordingly to the definition in (4.3.1), and $p : \mathbb{R}_+ \rightarrow L^2(\Omega)$

such that

$$\left\{ \begin{array}{l} \int_{\Omega} \underbrace{\partial_t \mathbf{u} \cdot \mathbf{v}}_{\langle \partial_t \mathbf{u}, \mathbf{v} \rangle} + \nu \int_{\Omega} \underbrace{\nabla \mathbf{u} \cdot \nabla \mathbf{v}}_{a(\mathbf{u}, \mathbf{v})} + \int_{\Omega} \underbrace{\mathbf{u} \cdot \nabla \mathbf{u} \cdot \mathbf{v}}_{c(\mathbf{u}, \mathbf{u}, \mathbf{v})} - \int_{\Omega} \underbrace{p \nabla \cdot \mathbf{v}}_{b(\mathbf{v}, p)} = \int_{\Gamma_N} \boldsymbol{\psi} \cdot \mathbf{n} \\ \int_{\Omega} w \nabla \cdot \mathbf{u} = 0 \end{array} \right.$$

for all $\mathbf{v} \in [H_{\Gamma_D, 0}^1(\Omega)]^3$ and $w \in L^2(\Omega)$ and such that $\mathbf{u}(0, \cdot) = \mathbf{u}_0(\cdot)$. The reason why we have decided to label each multi-linear operator lies in the linear nature of the numerical approach that we are going to expose.

4.4 Numerical approximation

In order to find an approximate solution of the problem, a discretization both in space and time is needed. In this section we illustrate the finite elements method to discretize in space while a semi-implicit Euler scheme.

4.4.1 Space discretization by means of Finite Elements Method

We first perform a space discretization of the weak formulation. To this aim we want to substitute the Hilbert spaces $V = [H_{\Gamma_D}^1(\Omega)]^3$ and $Q = L^2(\Omega)$ with two families of spaces V_h and Q_h depending on a positive parameter h , such that

$$V_h \subset V, \dim V_h = N_h < +\infty \quad \forall h > 0,$$

$$Q_h \subset Q, \dim Q_h = M_h < +\infty \quad \forall h > 0.$$

Assuming $\psi = 0$ on Γ_N , we now expose the new semi-discrete problem, called the Galerkin problem, as:

for each $t > 0$ find $(\mathbf{u}(t), p_h(t)) \in V_h \times Q_h$ such that

$$\begin{cases} (\partial_t \mathbf{u}_h(t), \mathbf{v}_h) + a(\mathbf{u}_h(t), \mathbf{v}_h) + c((\mathbf{u}_h(t), \mathbf{u}_h(t), \mathbf{v}_h) + b(\mathbf{v}_h, p_h(t)) = \mathbf{0} & \forall \mathbf{v}_h \in V_h, \\ b(\mathbf{u}_h(t), q_h) = 0 & \forall q_h \in Q_h \end{cases} \quad (4.4.1)$$

with $\mathbf{u}_h|_{\Gamma_D} = \phi_h$ and $\mathbf{u}_h|_{t=0} = \mathbf{u}_{0h}$, where ϕ_h and u_{0h} are appropriate approximations of ϕ and u_0 in V_h , respectively.

Now we discuss the Finite Element Method (FEM) in order to construct the two spaces V_h and Q_h . To do that, let us take a regular triangulation T_h of the domain Ω . The discretized domain made of tetrahedra K is defined as

$$\Omega_h = \bigcup_{K \in T_h} K.$$

The triangulation is characterised by the parameter h which defines the refining level of such triangulation

$$h = \max_{K \in T_h} h_K.$$

where h_T is a characteristic length of the element T of triangulation. Such mesh is called regular if, defined ρ_K as the diameter of the largest sphere inscribed in a tetrahedron, for a certain quantity $\delta > 0$

$$\frac{h_K}{\rho_K} \leq \delta \quad \forall K \in T_h.$$

Remembering our aim to properly choose the spaces V_h and Q_h , we introduce the space \mathbb{P}_r which is the space of polynomials of global degree less than or equal to r , with $r=1,2,\dots$:

$$\mathbb{P}_r = \left\{ p(x, y, z) = \sum_{0 \leq i+j+k \leq r} a_{ijk} x^i y^j z^k, \quad a_{ijk} \in \mathbb{R} \right\}$$

The spaces of finite elements we will use for numerical solution of our problem are:

$$V_h^r = \{v_h \in C^0(\Omega_h) : v_h|_K \in \mathbb{P}_r \quad \forall K \in T_h\} \cap V$$

$$Q_h^r = \{q_h \in C^0(\Omega_h) : q_h|_K \in \mathbb{P}_r \quad \forall K \in T_h\}$$

They are the spaces of continuous functions which are polynomial of degree r on each element T of the triangulation.

It is worthy to note that problem 4.4.1 is well posed only if the spaces V_h and Q_h satisfy the discrete inf-sup condition: there exists a positive constant β such that

$$\inf_{q_h \in Q_h} \sup_{\mathbf{v}_h \in V_h} b(q_h, \mathbf{v}_h) \geq \beta \|\mathbf{v}_h\|_{[H^1(\Omega)]^3} \|q_h\|_{L^2(\Omega)} \quad (4.4.2)$$

This crucial condition is satisfied by, for instance, the finite element couples $\mathbb{P}_2 - \mathbb{P}_1$ or $\mathbb{P}_{1bubble} - \mathbb{P}_1$, while equal order finite elements, such as $\mathbb{P}_2 - \mathbb{P}_2$ or $\mathbb{P}_1\mathbb{P}_1$ do not satisfy the inf-sup condition, so that instabilities of the discrete pressure arise. If equal orders are used in the simulations, a suitable stabilization must be added, such as Streamline Upwind Petrov-Galerkin with a Pressure-Stabilizing Petrov-Galerkin term (SUPG-PSPG) [39] (see Section 4.7).

Now, in order to obtain the algebraic formulation of the problem, we need to consider a basis function for each one of the two discrete spaces V_h^r and Q_h^r . We define $\{\beta_j\}_{j=1}^{M_h}$ the basis of Q_h^r and $\{\alpha_j\}_{j=1}^{N_h}$ the basis of V_h^r . In particular:

$$\alpha_j = \begin{cases} (\alpha_j, 0, 0) & \text{for } j = 1, \dots, L_h \\ (0, \alpha_j, 0) & \text{for } j = L_h + 1, \dots, 2L_h \\ (0, 0, \alpha_j) & \text{for } j = 2L_h + 1, \dots, 3L_h \end{cases} \quad (4.4.3)$$

where $3L_h = N_h = \dim V_h$. All functions of V_h and Q_h can be written as linear combination of the basis functions:

$$\mathbf{v}_h(\mathbf{x}) = \sum_{j=1}^{N_h} v_j \alpha_j(\mathbf{x}),$$

$$q_h(\mathbf{x}) = \sum_{k=1}^{M_h} q_k \beta_k(\mathbf{x}).$$

Similarly, since even the unknowns \mathbf{u}_h and p_h of the Glaerkin problem belongs to the subspaces, we can decompose them on their respective basis:

$$\mathbf{u}_h(\mathbf{x}, t) = \sum_{j=1}^{N_h} u_j(t) \boldsymbol{\alpha}_j(\mathbf{x}),$$

$$p_h(\mathbf{x}, t) = \sum_{k=1}^{M_h} p_k(t) \beta_k(\mathbf{x}).$$

We may then use the basis functions as the semi-discrete test function $\mathbf{v} = \boldsymbol{\alpha}_k$ for all $k = 1, \dots, 3L_h$ in momentum equation, and $w = \beta_k$ for all $k = 1, \dots, M_h$ in continuity equation. By collecting all such equations in vectors we obtain

$$\begin{cases} M \frac{d\mathbf{U}^h}{dt} + A\mathbf{U}^h + C(\mathbf{U}^h)\mathbf{U}^h - B\mathbf{P}^h = 0 \\ B^T\mathbf{U}^h = 0 \end{cases},$$

where

- $\mathbf{U}^h : \mathbb{R}_+^t \rightarrow \mathbb{R}^{3L_h}$ is the vector of coefficients of \mathbf{u} in the basis $\{\boldsymbol{\alpha}_j^h\}_j$
- $\mathbf{P}^h : \mathbb{R}_+^t \rightarrow \mathbb{R}^{M_h}$ is the vector of coefficients of p in the basis $\{\beta_j^h\}_j$
- $M \equiv M^h$ is the mass matrix with $M_{ij} = (\boldsymbol{\alpha}_i, \boldsymbol{\alpha}_j)$, $1 \leq i, j \leq 3L_h$
- $A \equiv A^h$ is the stiffness matrix with $A_{ij} = a(\boldsymbol{\alpha}_i, \boldsymbol{\alpha}_j)$, $1 \leq i, j \leq 3L_h$
- $C(\mathbf{U}_h)$ is a matrix such that $C_{ij} = c(\mathbf{U}^h, \boldsymbol{\alpha}_j, \boldsymbol{\alpha}_i)$
- B is a matrix with $B_{ij} = b(\boldsymbol{\alpha}_i, \beta_j)$. $1 \leq i \leq 3L_h, 1 \leq j \leq M_h$.

4.5 Time discretization

We have now to discretize in time: given $[0, T]$, we split it into N equi-spaced points $\{t_j\}_j$. Each sub-interval has length $\Delta t := \frac{T}{N}$, called time step, and we denote with \mathbf{U}_n^h the approximation of $\mathbf{U}^h(t_n)$ and with \mathbf{P}_n^h the approximation of $\mathbf{P}^h(t_n)$. In this work we consider the second order method BDF2 [40]. This implicit method leads to a system of equations that is still nonlinear due to the convective term, hence a higher computational cost is required. The choice usually made in hemodynamics is to use a

semi-implicit method with a second order extrapolation of the convective term:

$$C(\mathbf{U}_{n+1}^h)\mathbf{U}_{n+1}^h \simeq C(\mathbf{U}^{h,*})\mathbf{U}_{n+1}^h$$

where

$$\mathbf{U}^{h,*} = 2\mathbf{U}_n^h - \mathbf{U}_{n-1}^h \quad (4.5.1)$$

Hence the linear system in the unknowns \mathbf{U}_{n+1}^h and \mathbf{P}_{n+1}^h can be written as:

$$\begin{cases} \frac{M}{2\Delta t}(3\mathbf{U}_{n+1}^h - 4\mathbf{U}_n^h + \mathbf{U}_{n-1}^h) + A\mathbf{U}_{n+1}^h + B^T\mathbf{P}_{n+1}^h + C(\mathbf{U}^{h,*})\mathbf{U}_{n+1}^h = \mathbf{0} \\ B\mathbf{U}_{n+1}^h = \mathbf{0} \end{cases}$$

Under a matrix form,

$$\begin{bmatrix} K & B^T \\ B & 0 \end{bmatrix} \begin{bmatrix} \mathbf{U}_{n+1}^h \\ \mathbf{P}_{n+1}^h \end{bmatrix} = \begin{bmatrix} \frac{M}{2\Delta t}(4\mathbf{U}_n^h - \mathbf{U}_{n-1}^h) \\ 0 \end{bmatrix}$$

where

$$K = \frac{3}{2\Delta t}M + A + C(\mathbf{U}_n^{h,*}) \quad (4.5.2)$$

The condition for stability of a semi-implicit method is the existence of a constant $C > 0$ such that

$$\Delta t \leq C \frac{h}{\max_{x \in \Omega} |\mathbf{U}_n^h|}$$

which in this case is not too restrictive since Δt , for accuracy purposes, should be taken smaller than that required by the stability condition.

4.6 The SUPG-PSPG stabilization

Stabilization techniques prevent numerical oscillations and other instabilities in solving problems with advection-dominated flows and when using equal-order interpolation functions for velocity and pressure which do not satisfy the inf-sup condition (4.4.2), as mentioned in Section 4.4.1. In our work we considered finite elements of order $\mathbb{P}_2 - \mathbb{P}_2$ because of high accuracy and their availability in the LifeV library (see Chapter 5 for the details) but they are inf-sup unstable. We used Streamline-Upwind Petrov-Galerkin (SUPG) and Pressure-Stabilizing Petrov-Galerkin (PSPG) techniques in order to control the numerical instabilities. This approach consists in adding the residual of the momentum equation computed on each element of the mesh, producing a strongly consistent method. Hence, the discretized-in-time weak formulation with SUPG stabilization reads:

Find $\mathbf{u}_{n+1}^h \in V_{g,h}$ and $p_{n+1}^h \in Q_h$ such that:

$$\begin{aligned} & \left(\frac{3\mathbf{u}_{n+1}^h - 4\mathbf{u}_n^h + \mathbf{u}_{n-1}^h}{2\Delta t}, \mathbf{v}^h \right) + a(\mathbf{u}_{n+1}^h, \mathbf{v}^h) - b(p_{n+1}^h, \mathbf{v}^h) + c(\mathbf{u}^{h,*}, \mathbf{u}_{n+1}^h, \mathbf{v}^h) \\ & + b(q^h, \mathbf{u}_{n+1}^h) + s(\mathbf{u}_{n+1}^h, p_{n+1}^h, \mathbf{v}^h, q^h) = \mathbf{0} \quad \forall \mathbf{v}^h \in V_h, \forall q^h \in Q_h \end{aligned} \quad (4.6.1)$$

where

$$\begin{aligned} s(\mathbf{u}_{n+1}^h, p_{n+1}^h; \mathbf{v}^h, q^h) = & \\ & \sum_{K \in T_h} \delta_{SUPG-PSPG} \left(\left[\frac{3\mathbf{u}_{n+1}^h - 4\mathbf{u}_n^h + \mathbf{u}_{n-1}^h}{2\Delta t} + \nabla \cdot (\mathbf{u}^{h,*} \otimes \mathbf{u}_{n+1}^h) \right. \right. \\ & \left. \left. + \nabla p_{n+1}^h - \nabla \cdot (2\nu \mathbf{S}) \right], \left[\mathbf{u}^{h,*} \cdot \mathbf{v}^h + \frac{\nabla q^h}{\rho} \right] \right) \end{aligned}$$

is the SUPG-PSPG stabilization term with

$$\delta_{SUPG-PSPG} = \left(\left(\frac{2}{\Delta t} \right)^2 + \left(\frac{2 \|\mathbf{u}_h^n\|_\infty}{h} \right) + \frac{4\nu}{h^2} \right)^{-\frac{1}{2}} \cdot \delta,$$

being h the element length, $\mathbf{u}_h^* = 2\mathbf{u}_h^n - \mathbf{u}_h^{n-1}$ accordingly to the (4.5.1) and $S = \frac{\nabla \mathbf{u} + \nabla \mathbf{u}^T}{2}$.

Such new bilinear form (4.6.1) leads to a new Finite Element Matrix which is obtained from the previous K defined in (4.5.2) by considering the modification given by s .

Chapter 5

Results of the numerical simulations

This work aims at investigating a possible relation of stent-graft displacements, examined in Chapter 3, with hemodynamic variables obtained by CFD simulations. In Chapter 4 we hence described all theoretical aspects necessary for CFD simulations. In this chapter we initially present procedure we adopted to extract our computational domain for two of the three clinical cases at our disposal. Then we give some details about the tool we used and how we performed numerical simulations. Finally, we show results obtained from our study.

5.1 Computational domain

CFD analyses require the definition of a suitable mesh describing the fluid-domain. Since our purpose is to simulate blood flow through the stent-graft, we have to deal with the extraction of such domain. Firstly, we assume that no endoleak occurred in all of the clinical cases we examined, so that blood entirely flows through the implanted device. Since aneurismatic sac is completely excluded from the aortic circulation, in our computational model we did not consider the aneurism walls. Abdominal aortic stent-grafts are fabric tubes supported by a metal framework on the outside wall. Therefore blood is directly in contact with the inner fabric instead of metal struts of the device. Finally, the present study adopted the assumption of rigid walls neglecting the stent-graft compliance. However, this approximation is not too restrictive since the stent-graft materials are not as elastic as the physiological aorta. Starting from these assumptions, we reconstructed stent-graft lumen, i.e. our computational domain, from CT images of each follow-up examination of patient, as described in the following subsection. In subsection 5.1.2 generation of the respective meshes is reported.

5.1.1 Lumen extraction

The procedure to reconstruct stent-graft lumen required the use of ITK-Snap (<http://www.itksnap.org>). We did not use VMTK software, as in stent-graft segmentation case, since the high intensity of stent-graft in CT images prevented to precisely detail surface contours. Input of the program is a DICOM series, as in VMTK case. The interface allows visualization of axial slices and reconstructions of sagittal and coronal reconstruction. A fourth windows shows the 3D reconstruction resulting from segmentation. Segmentation by using this software may be performed in two different modes: manual segmentation and semi-automatic segmentation. As in VMTK, semi-automatic method is not suitable for lumen reconstruction, hence we used manual segmentation. It consists in highlighting in each CT slice anatomical structures we want to reconstruct, see 5.1.

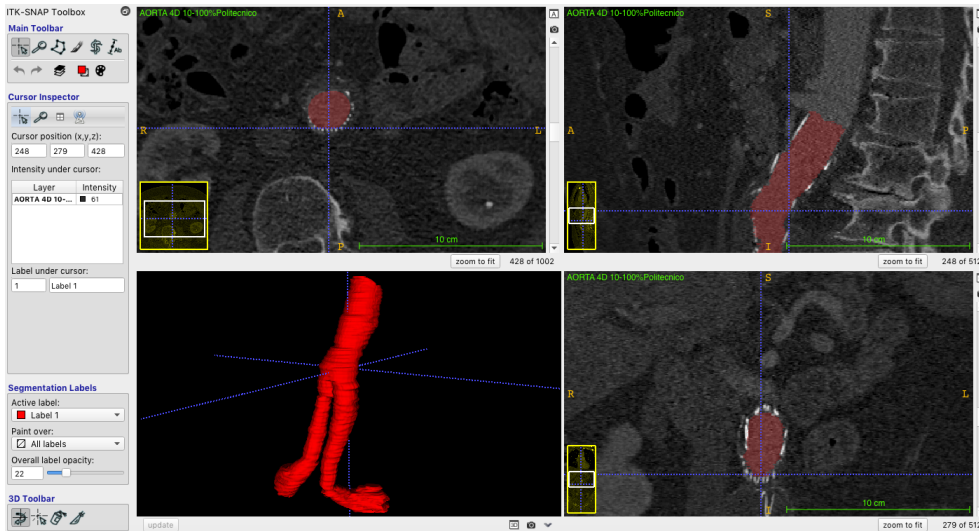


Figure 5.1: ITK-Snap software was used to segment stent-graft lumens. Manual segmentation allowed to reconstruct, slice by slice, geometric lumen contours. Here an example concerning Patient III at T1.

However, resulting 3D reconstruction is highly rough. To obtain a surface suitable for CFD simulations we applied a step-by-step procedure in VMTK which substantially consists in the following commands:

- **vmkicpregistration**: as we discussed in Chapter 2, image registration is always needed in order to align surfaces of the same patient. For both Patient I and Patient III, we registered all lumens in the most recent coordinate system, that is T48 for Patient I and T60 for Patient III.
- **vmtksurfaceclipper**: in order to be able to perform numerical simulations we had to open the model in correspondence of the boundaries through which blood

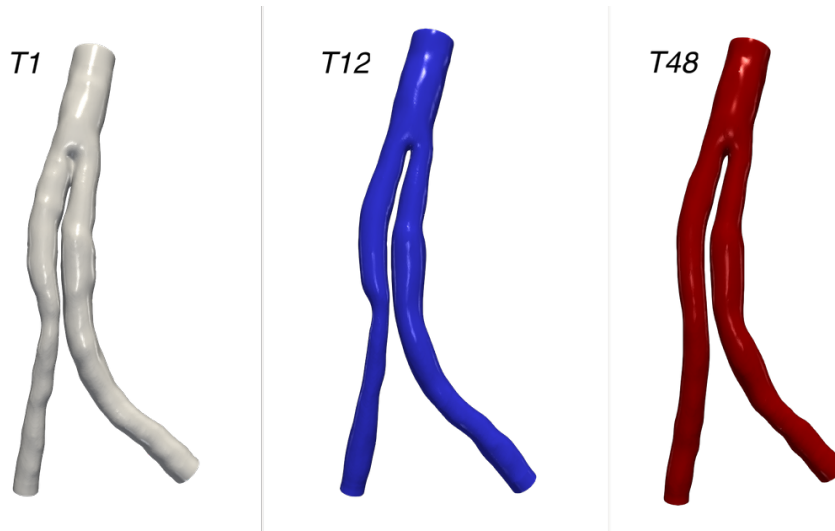


Figure 5.2: Patient I lumen reconstructions. From left to right, lumen from T1, T12 and T48 follow-up images.

flows. In fact, from the reconstruction procedure, these boundaries are closed. We cut the original surface by planes perpendicular to lumen longitudinal axis.

- **vmtkflowextensions:** the 3D surface is artificially extended by inserting at the boundary sections cylindrical regions called flow extensions. The flow extensions are designed to extend the inflow and the outflows and their role is to reduce the impact of modeling choices and uncertainties in the boundary conditions on the numerical results.
- **vmkssurfacesmoothing:** we applied a global smoothing filter based on the algorithm described by Taubin et al. [41] so to obtain a smoother surface with no visible slices.

Resulting lumen reconstruction are illustrated in Figure 5.2 and 5.3, for Patient I and Patient III respectively.

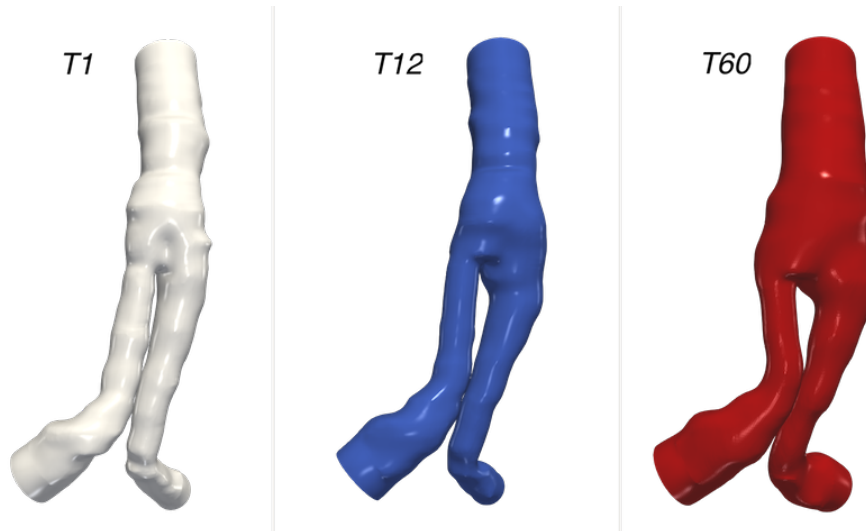


Figure 5.3: Patient III lumen reconstructions. From left to right, lumen from T1, T12 and T60 follow-up images.

5.1.2 Mesh generation

Once lumen geometries were obtained, we proceeded to generate unstructured tetrahedral meshes. For this purpose we used the code *fsimeshgeneratorbis.py* [42], a python code able to extrapolate two types of mesh: a mesh of the internal vessel, called fluid mesh, and the mesh of the lumen, called structure mesh. We did not performed Fluid Structure Interaction simulations, since we considered the stent-graft in the aorta as a rigid body, hence we only generated the fluid mesh for each of the reconstructed lumens. VMTK provided the interface of the python code we used. By following instructions appearing on the screen, we chose parameters to generate the mesh grid. We decided to performe a constant remesh, therefore we set a precise value, called edge length (h), for a representative value of the space discretization parameter, i.e. of the dimension of the tetrahedra. In addition, we introduced three boundary layers to better capture viscous effects near the wall. Total thickness of the boundary layer (τ) is constant everywhere and required to be 0.1 of the edge length. The thickness ratio (ρ), i.e. ratio between the thickness of two successive boundary layers, has been set equal to 0.7. Imposing these parameters, we created six tetrahedral meshes suitable for CFD simulations. In Table 5.1 we reported all details concerning tetrahedral meshes we generate for the two patients and for each follow-up. Mesh sizes varied case-by-case but we chose the edge length parameter h so to obtain a mesh of about 300k elements.

Table 5.1: Parameters of the generated meshes: N is the number of tetrahedra; h is a representative value of the space discretization parameter, i.e. of the dimension of the tetrahedra; n stands for the number of boundary layers introduced; τ is the total thickness of the boundary layer; ρ is the thickness ratio between two consecutive boundary layers.

	<i>PI-T1</i>	<i>PI-T12</i>	<i>PI-T48</i>	<i>PIII-T1</i>	<i>PIII-T12</i>	<i>PIII-T60</i>
N	370k	375k	381k	214k	229k	318k
h	0.15cm	0.15cm	0.15cm	0.2cm	0.2cm	0.2cm
n	3	3	3	3	3	3
τ	0.1	0.1	0.1	0.1	0.1	0.1
ρ	0.7	0.7	0.7	0.7	0.7	0.7

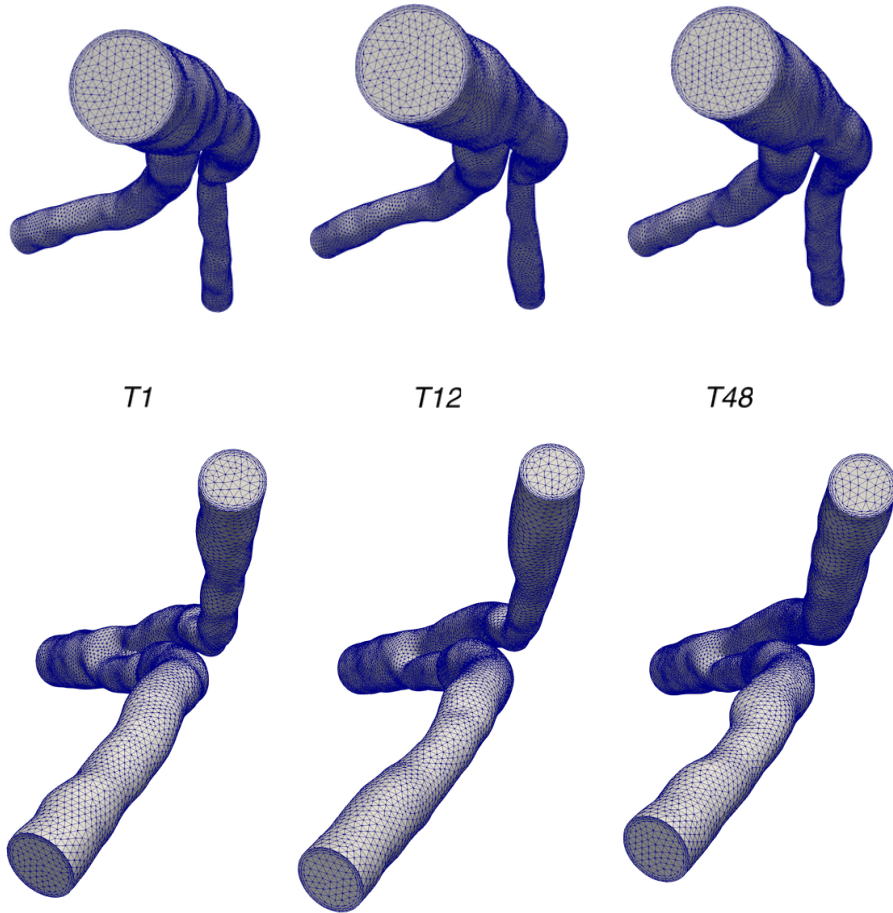


Figure 5.4: Meshes of Patient I at time T1, T12 and T48 from top and bottom view.

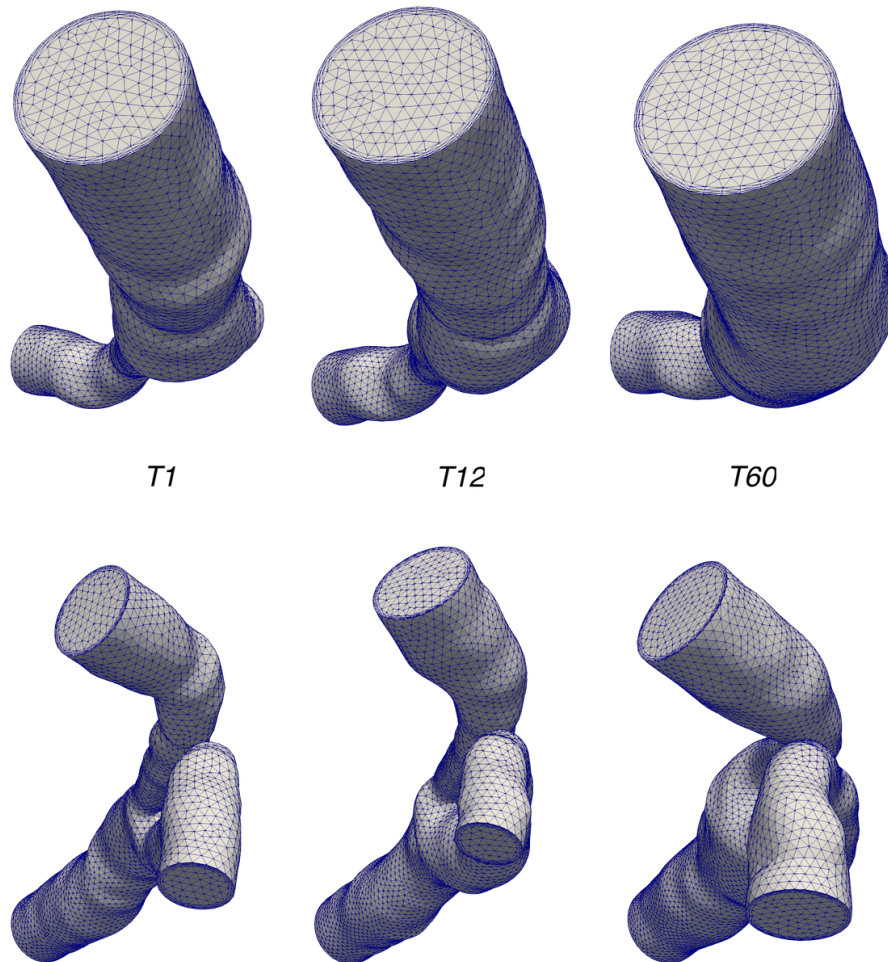


Figure 5.5: Meshes of Patient III at time T1, T12 and T60 from top and bottom view.

5.2 LifeV

To perform the simulations, we used the open-source C++ library LifeV (www.lifev.org), a collaborative project including MOX laboratory of the Department of Mathematics of the Politecnico in Milano, the Ecole Polytechnique Fédérale of Lausanne in Switzerland, the INRIA, Paris in France and the Emory University in the U.S.A. It has been actually used in computational hemodynamics, in fluid-structure interaction problems, in porous media, ice sheets dynamics for both forward and inverse problems. One of the main field of application is cardiovascular mathematics. LifeV is a parallel library for the approximation of Partial Differential Equations (PDEs) by the finite element method in one, two and three dimensions. In order to simulate blood flow through out patient specific stent-graft lumens, we changed some input parameters of a pre-existing code available in LifeV. To this purpose we worked on two files, file *data* and file *cylinder.cpp*.

Data file consists in the physical characterisation of the fluid, the time and space discretization, velocity profile, the mesh file and the choices about the solver and the preconditioner. In particular, in order to find the solution of the linear system we gained in Section 4.5 we used the GMRes solver available in the package Ifpack of Trilinos of LifeV. Boundary conditions are set in the file *cylinder.cpp*. In the following subsection we will describe our choices concerning these parameters.

5.3 Details on the numerical experiments

5.3.1 Boundary conditions

The Navier-Stokes equations are partial differential equations and so they need to be equipped by suitable boundary conditions to solve the problem. Boundaries of our domain are the following (see Figure 5.6):

- Γ_{in} : inlet section of the stent-graft lumen
- Γ_{wall} : lumen wall
- Γ_{out1} and Γ_{out2} : iliac outlet sections

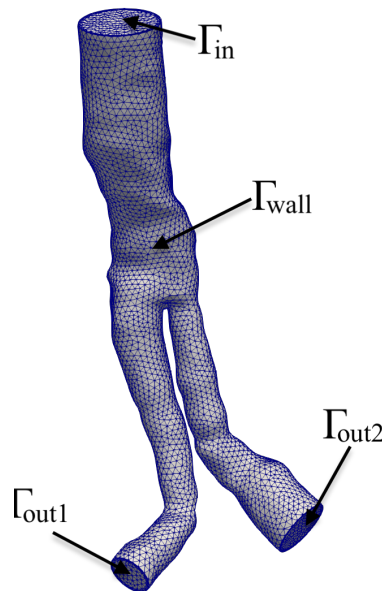


Figure 5.6: Boundaries of the computational domain.

We imposed:

- Dirichlet boundary condition with parabolic velocity profile, also known as *Poiseuille profile*, on inlet section

$$\mathbf{u}(\mathbf{x}, t) = -u_{parab}(\mathbf{x}, t)\mathbf{n}_{in} \quad \forall \mathbf{x} \in \Gamma_{in}, t \in (0, T]$$

where:

- $u_{parab} = 2Q/A_{in} \cdot (1 - r^2/R^2)$ with $Q = Q(t)$ the inlet flow rate waveform, A_{in} the inlet section area, R is half of the inlet diameter, $r = \sqrt{(x - x_0)^2 + (y - y_0)^2 + (z - z_0)^2}$ with (x_0, y_0, z_0) coordinates of the center of inlet section. $Q(t)$ has a physiological waveform, as shown in Figure 5.7 where the systolic phase, in which the flow is positive, and the diastolic phase, with negative flow, can be detected.

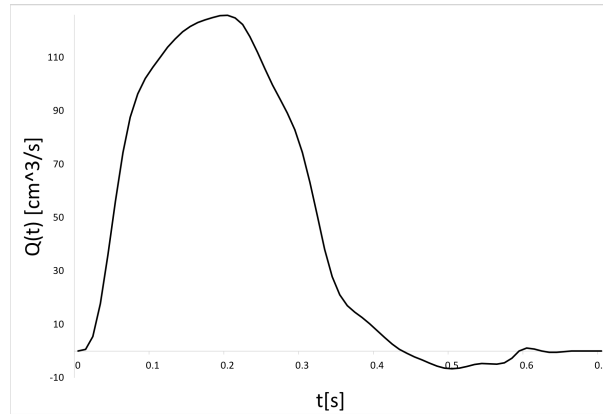


Figure 5.7: Physiological inlet flow rate $Q(t)$.

- \mathbf{n}_{in} in the outward normal at the inlet.
- no-slip boundary condition on the lumen wall

$$\mathbf{u}(\mathbf{x}, t) = \mathbf{0} \quad \forall \mathbf{x} \in \Gamma_{wall}, t \in (0, T]$$

- Robin non-linear boundary condition on the outlet surfaces. We decided to impose a Robin boundary condition on the outlets of the domain in order to avoid backflow instabilities. These kind of instabilities takes place when flow entirely (or partially) reverses through an outlet. Retrograde flow may occur during diastolic phase or can be induced by recirculations and vortices near outlet boundaries. In order to avoid numerical instabilities, a stabilization term is added to the Neumann boundary condition, as proposed by [43] and [44]. This approach is based on the idea to suppress the last term in the following energy balance of Navier Stokes

formulation:

$$\int_{\Omega} \frac{1}{2} \|\mathbf{u}\|_2 = - \int_{\Omega} \nu \nabla \mathbf{u} : \nabla \mathbf{u} - \int_{\Gamma_{out}} \frac{1}{2} \|\mathbf{u}\|_2 \mathbf{u} \cdot \mathbf{n} \quad (5.3.1)$$

where the term on the left is the total energy of the 3D fluid in a domain Ω while the first term on right hand side denotes the dissipative effects, always positive. Backflow occurs when $\mathbf{u} \cdot \mathbf{n} < 0$ hence during backflow the last term on the right hand side could lead to an uncontrolled energy increase. Suppression of such unstable term is equivalent to adding the stabilization term to the Neumann boundary condition as follows:

$$-p\mathbf{n} + \nu \frac{\partial \mathbf{u}}{\partial \mathbf{n}} = \beta \int_{\Gamma_{out}} \frac{1}{2} \|\mathbf{u} \cdot \mathbf{n}\|_-$$

with $\beta \in (0, 1]$.

To sum up, boundary conditions will be:

$$\begin{cases} u(x, t) = -u_{parab}(x, t)n_{in} & \text{on } \Gamma_{in} \\ u(x, t) = 0 & \text{on } \Gamma_{wall} \\ -p\mathbf{n} + \nu \frac{\partial \mathbf{u}}{\partial \mathbf{n}} = \beta \int_{\Gamma_{out}} \frac{1}{2} \|\mathbf{u} \cdot \mathbf{n}\|_- & \text{on } \Gamma_{out1} \text{ and } \Gamma_{out2} \end{cases} \quad (5.3.2)$$

5.3.2 Simulation parameters

In this subsection we give details about how we modified file *data* we introduced in Section 1.2, for each case. Some parameters were the same for all simulations we performed, in particular:

- blood density: $\rho = 1.06 \text{ g/cm}$;
- blood dynamic viscosity $\mu = 0.035 \text{ g/(cms)}$;
- blood kinematic viscosity: $\nu = \frac{\mu}{\rho} = 0.033 \text{ cm/s}^2$;
- systolic inlet flow rate: $Q(t)_{syst} = 125 \text{ cm}^3/\text{s}$;
- $\mathbb{P}_2 \mathbb{P}_2$ Finite Elements spaces;
- SUPG-PSPG stabilization with coefficient $\delta = 0.1$;
- backflow stabilization term: $\beta = 0.5$;
- two cardiac cycles, each of period $t_{hb} = 0.7 \text{ s}$, for a total time $T = 2 \cdot t_{hb} = 1.4 \text{ s}$;
- time step: $\Delta t = 0.01\text{s}$;

Inlet radius is calculated for each specific geometry. Since inlet velocity and Reynolds number are radius dependent quantities (see Eq. 5.3.3 and 5.3.4), they assume different values case by case.

$$\mathbf{u}_{in}(t) = \frac{Q(t)}{A_{in}} \quad A_{in} = \pi \cdot R_{in}^2 \quad (5.3.3)$$

Table 5.2: Radius measures of the inlet section of all the meshes and the maximum velocity and Reynold’s number reached at the systolic peak, i.e. $t=0.2$ s.

	PI-T1	PI-T12	PI-T48	PIII-T1	PIII-T12	PIII-T60
R (mm)	0.833	0.836	0.822	1.032	1.033	1.173
u_{syst} (cm/s)	114.59	113.86	117.77	74.72	74.57	57.83
Re_{syst} (-)	2892.08	2884.50	2933.62	2336.67	2334.40	2055.79

$$Re = \frac{uD_{in}\rho}{\mu} \quad D_{in} = 2R_{in} \quad (5.3.4)$$

In Table 5.2 radius, inlet velocity and Reynolds number at systolic peak are reported.

5.4 Description of blood dynamics for each patient and case

In this section we want to describe results of numerical simulations. We investigated two of the three clinical cases at our disposal: we selected Patient I and Patient III since they had the same number of follow-up examinations, i.e. three, and because both of them presented interesting displacements behaviours (see Chapter 3). One simulation for each follow-up has been performed for both cases: PI-T1, PI-T12 and PI-T48 for Patient I and PIII-T1, PIII-T12 and PIII-T60 for Patient III. Visualization of simulation results has been performed with Paraview (www.paraview.org), a software useful to visualize and post-process the results of the numerical experiments. By the use of such software it is possible to analyze the data using qualitative and quantitative techniques.

We always analysed fluid-dynamics resulting from the second cardiac cycle. This choice was made since first cycle is affected by the transient effect of the initial condition of velocity equal to zero in all the domain.

5.4.1 Patient I

Velocity fields

In order to analyse the velocity field, we obtained longitudinal and transversal slices. Axial evolution of blood flow could be detected by extracting slices which cut the domain in two longitudinal halves. The figures are taken at different moments of the cardiac cycle, in particular at pre-systolic peak $t = 0.1$ s (first column), systolic peak $t = 0.2$ s (second column), mid-deceleration point $t = 0.31$ s (third column). See Figure 5.8 to visualize such time instants. Pre-systolic point has been chosen since it shows the entering wave velocity in the domain.

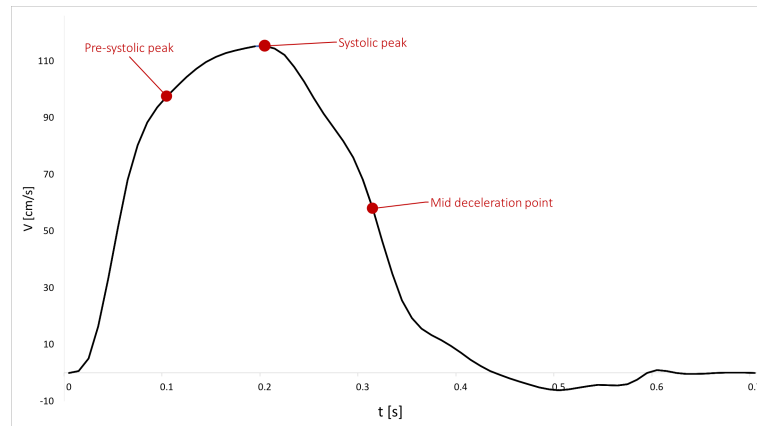


Figure 5.8: Physiological inlet velocity waveform.

We noticed that the geometry of the stent-graft makes the level of bifurcation a crucial point where blood flow splits in two separated flows. By observing in Figure 5.9, in the three different cases PI-T1, PI-T12 and PIT48, the velocity field features similar trends before the device bifurcation. After this point the asymmetrical configuration of the two legs of the graft leads to two different velocity fields. It is worth noting that the right branch visibly showed a change in flow pattern from PI-T1 to PI-T48 since the dilation of the diameter at the level of the actual iliac bifurcation (where the branches of the device effectively divert), discussed in Chapter 3, led to a decrease in velocity. At the systolic peak, left branch exhibited a flow which is highly skewed towards internal side of the branch due to its curvature. Both at systolic peak and at mid-deceleration point, secondary flows and vortex formations could be observed. In order to further analyse and compare these phenomena we decided to consider six sections: at the inlet (A), at level of stent bifurcation (B), in the middle (C), at actual bifurcation of iliac branches (D), at distal legs (right E and left F), as Figure 5.10 shows, for each of the three follow-up simulations and at systolic peak and mid-deceleration point. We superimposed velocity contour maps over velocity streamlines projected on the cross sections in order to better evaluate secondary flows, recirculations and vortex formations. In Figure 5.10 velocity contours at systolic peak are illustrated. We observed that at section B flow splitted in two velocity fields due to the physical division of the lumen. In particular, section B of PI-T48 exhibited the presence of additional vortices. Cross sections below the bifurcations are characterised by highly complex velocity patterns. Recirculation zones are visible at section C on the external side of the left branch in case of PI-T12 and PI-T48 which match with the fact that bifurcation point skews flow towards the inner wall downstream of the bifurcation, as previously observed. Right branch did not highlight particular complex behaviours, except for section E in TI-T1 and TI-T12 where secondary flows occurred. Figure 5.11 illustrates velocity contour

maps overlapped on projection of the velocity streamlines at mid-deceleration point where recirculations are expected to develop because of the deceleration experienced by blood at the specific time instance of the cardiac cycle. In fact, in all the examined sections recirculations are present. Section B exhibits in all the three cases the typical shape of Dean vortices at both left and right side. In opposition with systolic peak analysis, in this case the right branch shows the creation of recirculation zones (section C) and secondary flows (section D).

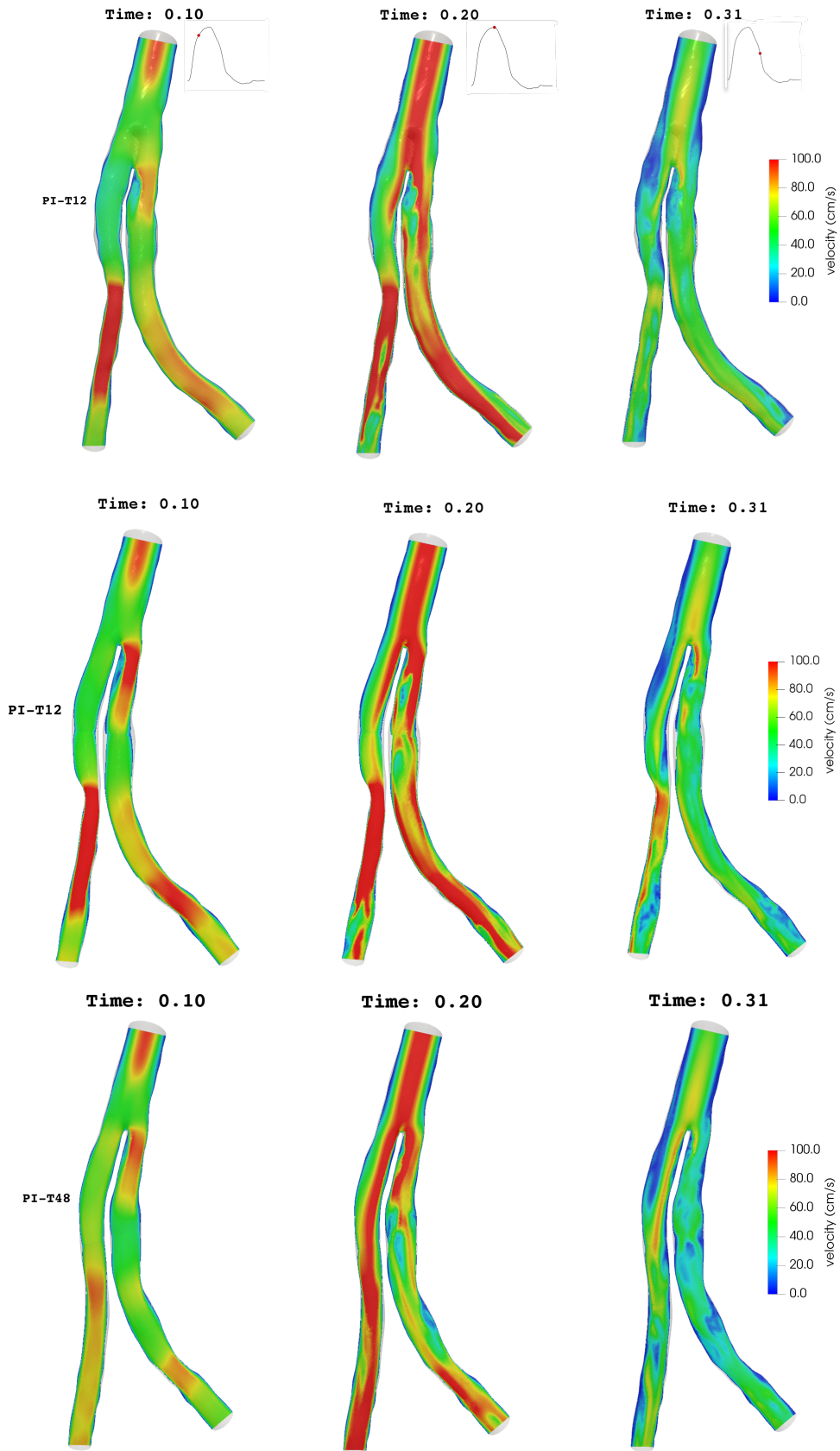


Figure 5.9: Velocity field on longitudinal plane from the inlet to the outlets of PI-T1 (first row), PI-T12 (second row) and PI-T48 (third row) at the pre-systolic peak (on the left), systolic peak (in the centre) and mid deceleration point (on the right).

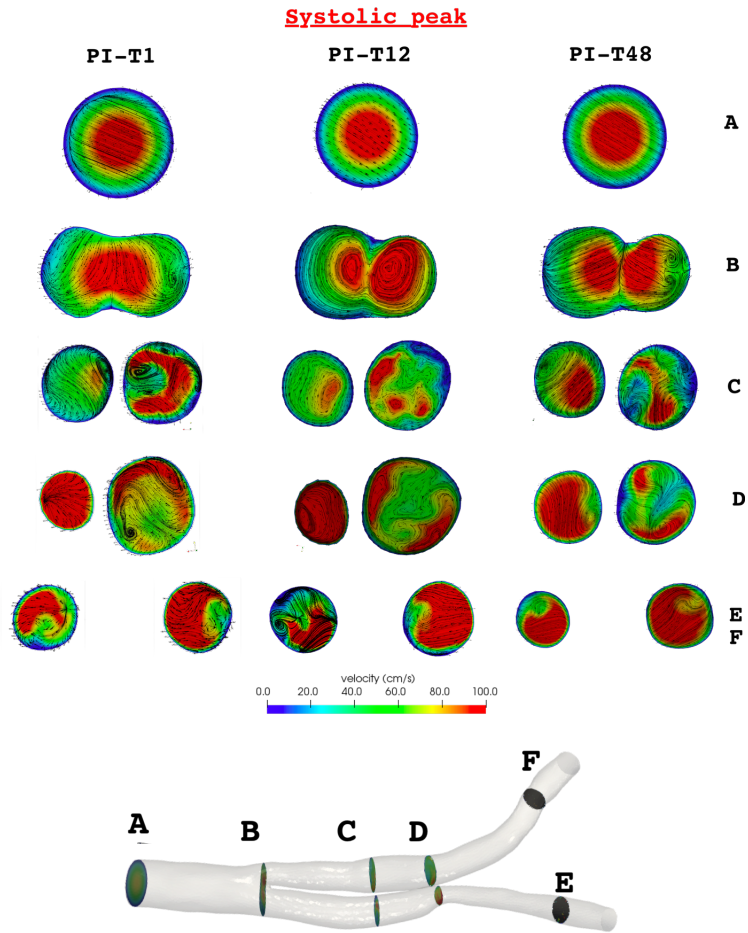


Figure 5.10: Velocity contour color maps and surface streamlines projected on the cross-sections A, B, C, D, E and F, defined at the bottom, at systolic peak for PI-T1 (first column), PI-T12 (second column) and PI-T48 (third column)..

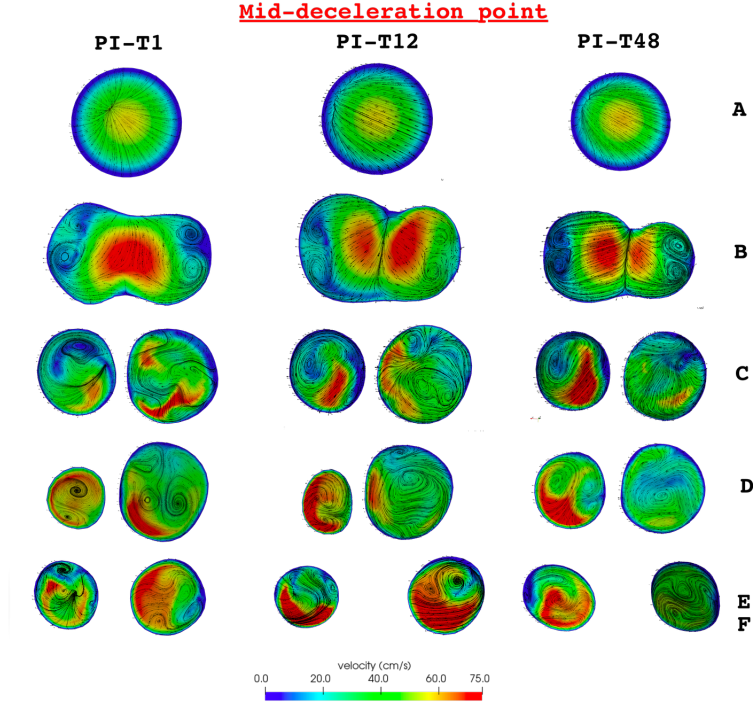


Figure 5.11: Velocity contour color maps and surface streamlines projected on the cross-sections A, B, C, D, E and F (defined in Figure 5.10) at mid-deceleration point for PI-T1 (first column), PI-T12 (second column) and PI-T48 (third column).

WSS

An important quantity used to evaluate the impact of the fluid dynamics in the lumen wall is the Wall Shear Stress (WSS). To define WSS we first introduce the vector $\boldsymbol{\tau}$ as :

$$\boldsymbol{\tau} = \boldsymbol{\sigma} \cdot \mathbf{n} - (\mathbf{n} \cdot \boldsymbol{\sigma} \cdot \mathbf{n}) \cdot \mathbf{n}, \quad \boldsymbol{\sigma} := \mu(\nabla \mathbf{u} + \nabla \mathbf{u}^T) \quad (5.4.1)$$

We then call WSS the Euclidean norm of $\boldsymbol{\tau}$ in \mathbb{R}^3 :

$$WSS = |\boldsymbol{\tau}| = \sqrt{\tau_x^2 + \tau_y^2 + \tau_z^2} \quad (5.4.2)$$

A WSS-related index is the Time Averaged Wall Shear Stress (TAWSS). Since we consider the second cardiac cycle, i.e. the time interval $[T; 2T]$, we can say:

$$TAWSS = \frac{1}{T} \int_T^{2T} WSS dt \quad (5.4.3)$$

In Figure 5.12 WSS color maps for all the three follow-up at systolic peak and TAWSS color maps are depicted. We noticed that spikes of WSS values are reached by the right branch at the level of bifurcation of the the iliac arteries, where the stent-graft has a

narrower diameter. In this point WSS is equal to 17.7 Pa for PI-T1, 23.5 Pa for PI-T12 and 14.8 Pa for PI-T48. In general, right leg of the device experiences high level of WSS, particularly at systolic peak of PI-T1 and PI-T12. Since in PI-T48 the diameter of the endograft in this point increased, the overall region of the right side exhibits lower WSS values. At bifurcation of the device, slightly on the left side, peaks of shear stress on the wall are visible. Similar observations could be applied to the mid-deceleration case, in which remarkable region are the right branch at the level of its narrowing and at bifurcation of the device. TAWSS patterns are similar to the WSS ones. High values of TAWSS are visible in the bifurcation zone, particularly on the right side of the device. Reduction of TAWSS from PI-T1 to PI-T48 occurred on the left branch and we observed a general more uniform distribution.

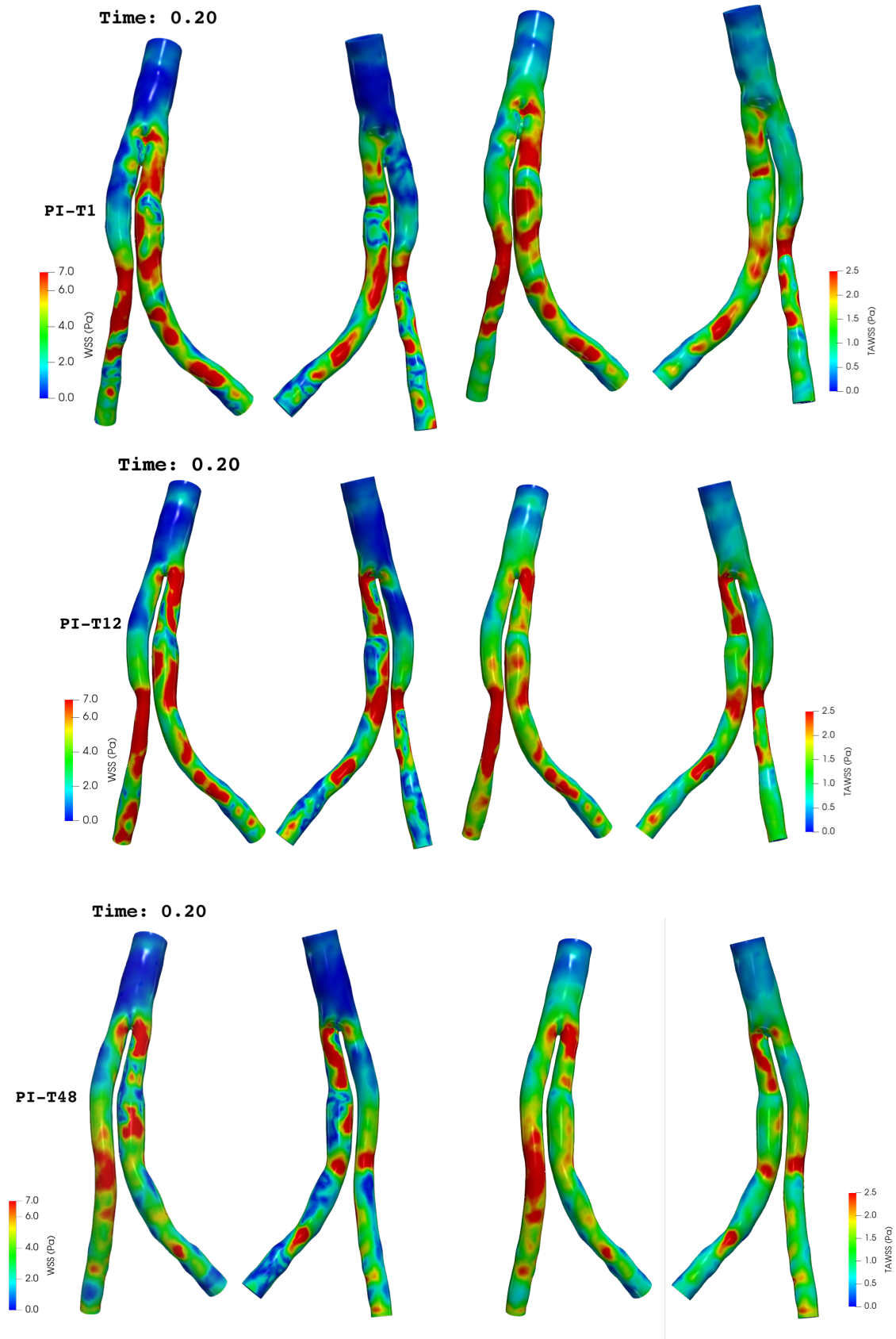


Figure 5.12: On the left, Wall Shear Stress for PI-T1 (first row), PI-T12 (second row) and PI-T48 (third row) at systolic peak. On the right, Time Average Wall Shear Stress.

5.4.2 Patient III

The reason we selected this clinical case consists in the particular outcomes post-EVAR he experienced. As we discussed in Chapter 3, Patient III endograft underwent to a significant dilation of the central metal wire at the posterior side, i.e. at the level of the stent curvature. In this section we therefore illustrate the results of fluid-dynamic simulations with particular attention to the region where the stent experienced this kind of consequence.

Velocity fields

In order to perform a first analysis of the velocity fields, we considered internal longitudinal slices which axially cut the domain in two halves, posterior and anterior, as we did for Patient I, see Figure 5.13. It is worthy noting that velocity reaches higher values along right branch since the diameter is smaller on this side with respect to the left one. In addition, both legs are characterised by a high curvature below the actual bifurcation of the iliac branches which skews the flow towards the inner sides of the device. Effect of this phenomenon is the formation of recirculation and vortical zone on the external sides. It is evident the influence of the increased diameter in PIII-T60 where the entering wave velocity reaches lower values. Comparison among velocity fields at mid-deceleration point (column on the right in Figure 5.13) leads to say that the overall dilation of PIII-T60 lumen prevents recirculations and vortices which are visible along the right leg in PIII-T1 and PIII-T12.

We now want to focus on the dilation portion of the lumen. To this aim we reported the velocity field at an additional sliced planes including the inlet and the dilated area, as Figure 5.14 shows. In this way we are able to visualize the propagation of the blood wave velocity in relation with the part of the domain of our interest. It is worthy noting that in PIII-T1 the jet propagates parallel with respect to the walls, then it impinges the wall of the graft just below its curvature. At the opposite side of this impingement area, i.e. where the stent-graft dilation occurred, a large area of ricirculation is present. Similar considerations may be applied to TIII-T12, while in TIII-T60 the analysed region exhibits a dilation such that at both systolic peak and mid-deceleration point large zones have null velocity.

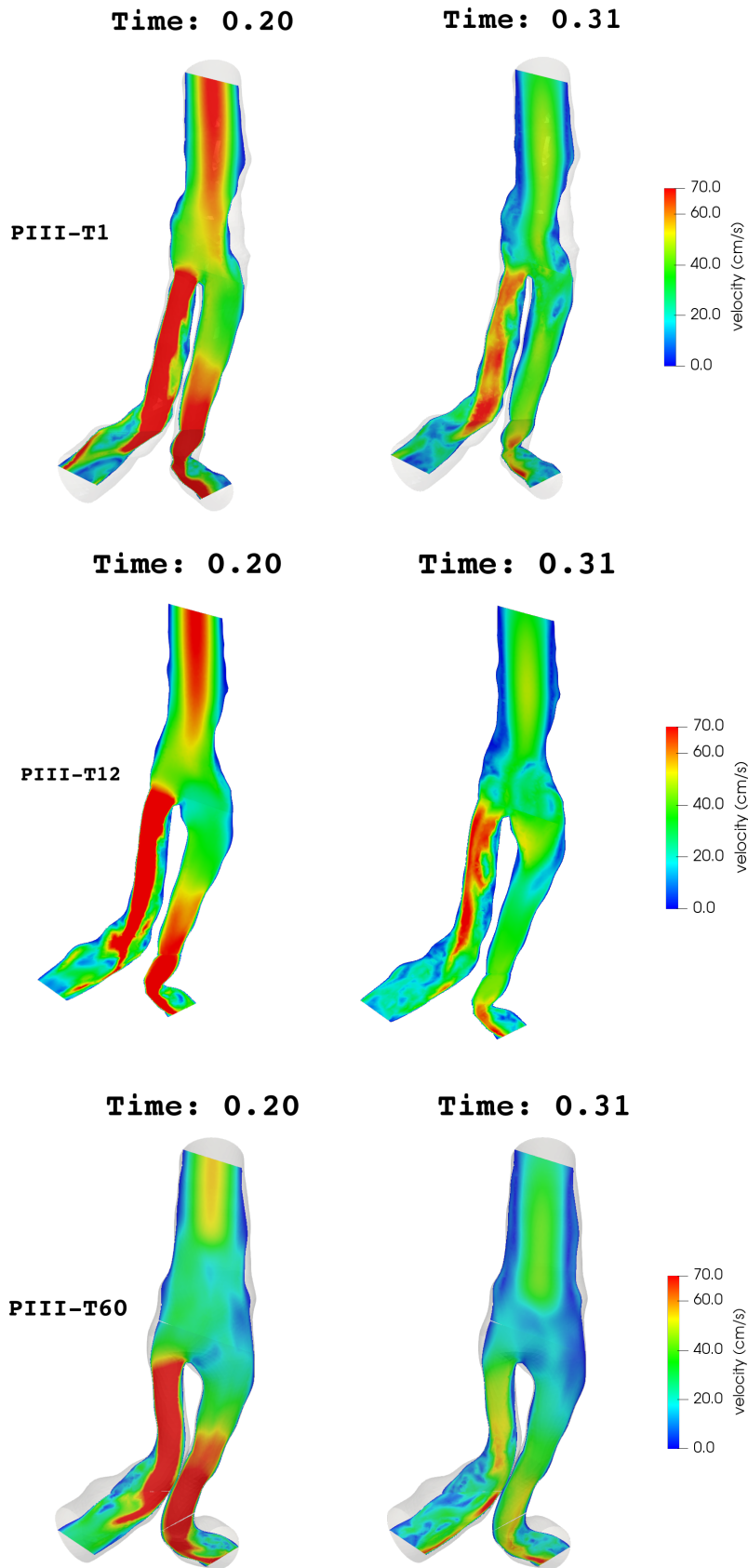


Figure 5.13: Velocity field on longitudinal plane from the inlet to the outlets of PIII-T1 (first row), PIII-T12 (second row) and PIII-T60 (third row) at systolic peak (on the left) and mid deceleration point (on the right).⁸⁷

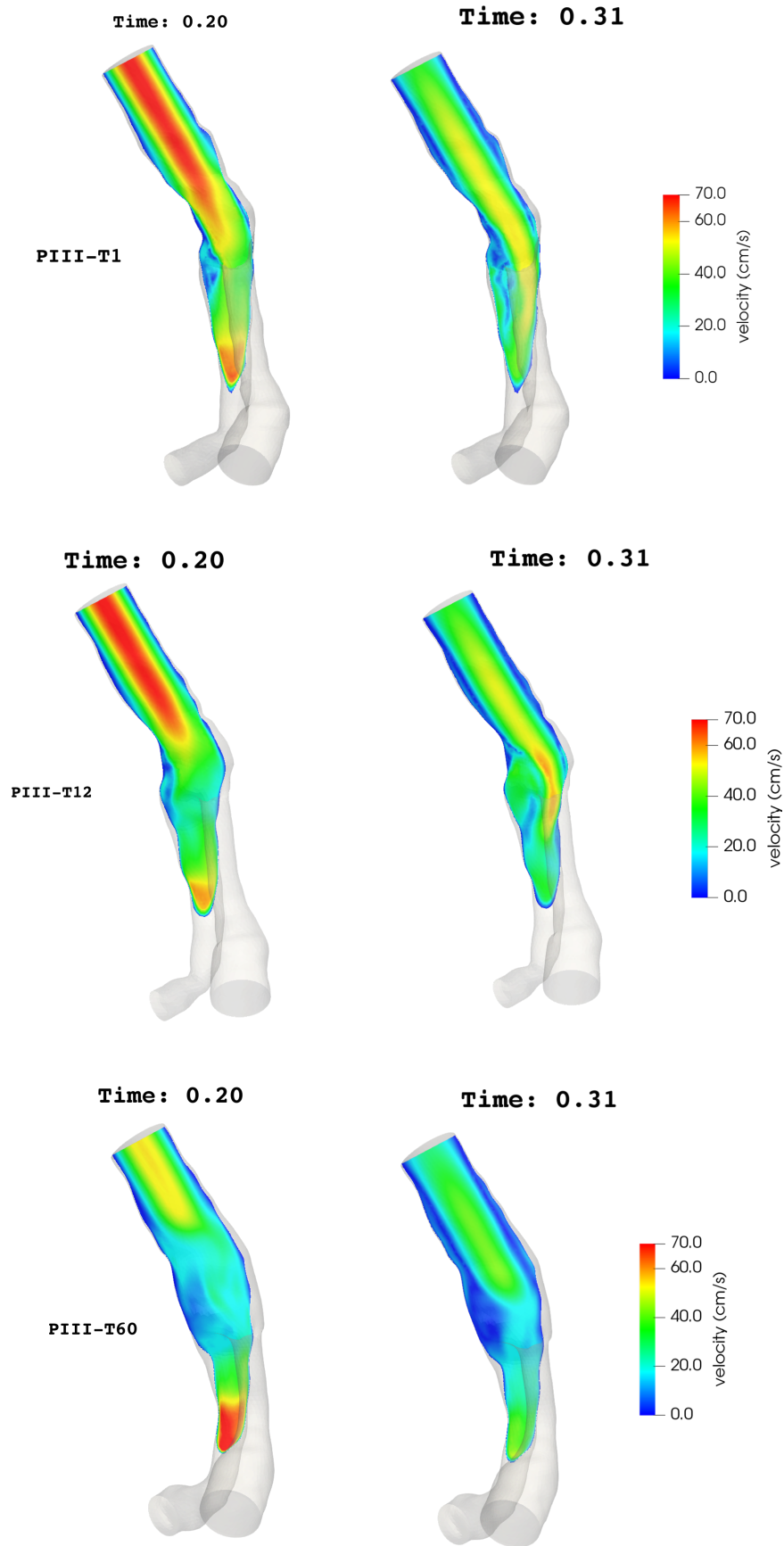


Figure 5.14: Velocity field on plane from the inlet to the dilation area of PIII-T1 (first row), PIII-T12 (second row) and PIII-T60 (third row) at systolic peak (first column) and mid deceleration point (second column).

WSS

We computed Wall Shear Stress at the systolic peak and Time Averaged Wall Shear Stress, as Figure 5.15 illustrates. Maximum values are reached at systolic peak. We observed large values in the right leg region, mostly in PIII-T12 and PIII-T60 and in particular in the portion just below the stent bifurcation. Distal areas of the device, below actual bifurcation of the iliac branches, experience high WSS due to the angulated configuration of both legs. We also noticed that no spikes are visible in the area of stent curvature, where the dilation occurred. Therefore, as we did not expected, we did not experienced high values of WSS in this region where jet strongly impinges on this part of the wall.

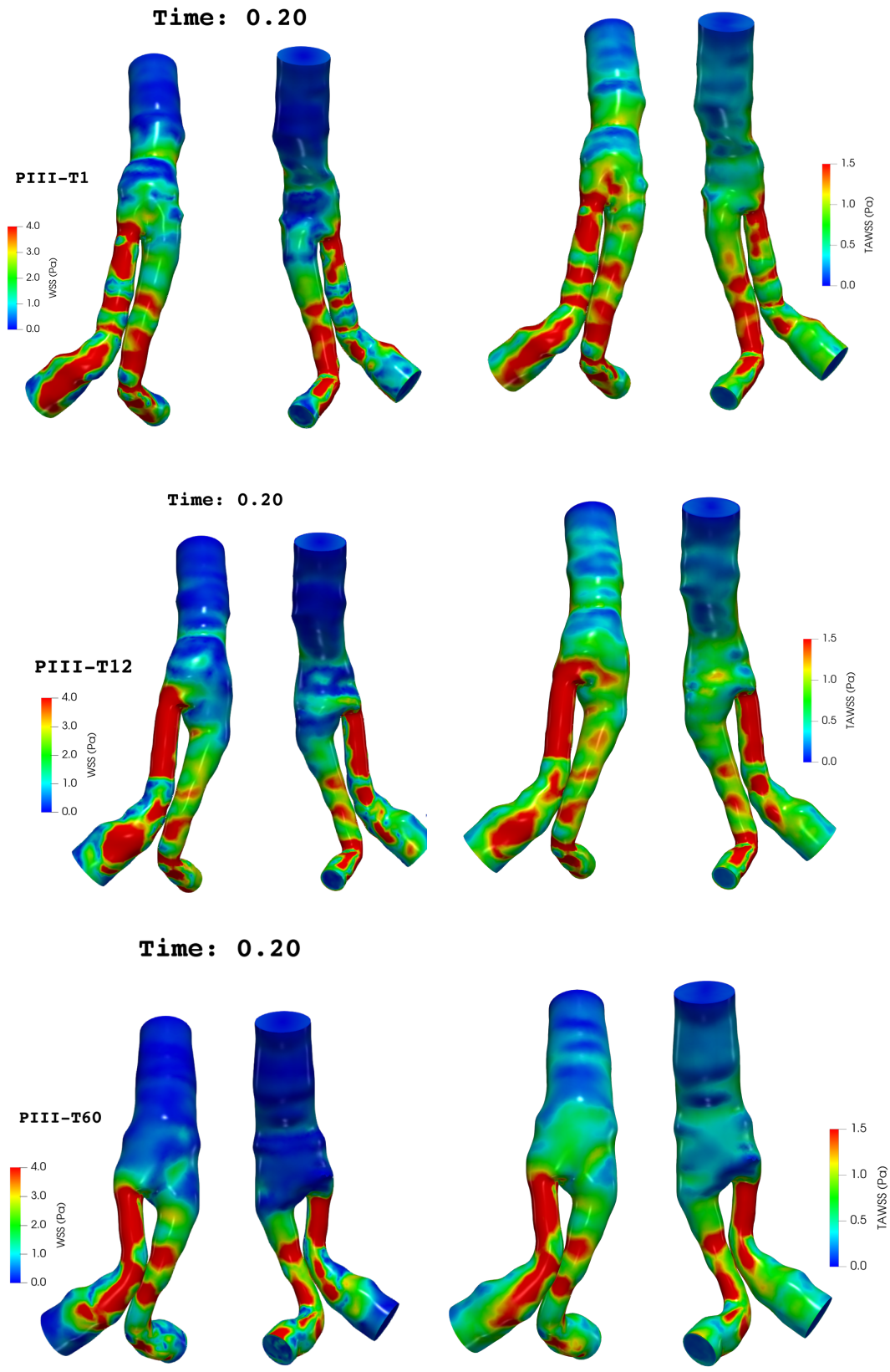


Figure 5.15: On the left, Wall Shear Stress for PIII-T1 (first row), PIII-T12 (second row) and PIII-T60 (third row) at systolic peak (on the left) and mid deceleration point (on the right). On the right, Time Average Wall Shear Stress.

Chapter 6

Relationships between blood dynamics and stent displacements

In this chapter we want to discuss the relationship between the displacements of the stent-grafts we analysed in Chapter 3 and the fluid-dynamics resulting from the CFD simulations examined in Chapter 5. Therefore, we are going to discuss the effects that the blood flow may have on the stent-graft migration, both within the cardiac-cycle and among follow-ups.

6.1 Patient I

6.1.1 WSS-Displacements within the cardiac-cycle

In Chapter 3 we illustrated stent-graft behaviours during the cardiac cycle. We observed that the overall changes in position of the device can be considered a rigid translation of the whole device in the lateral direction, in particular towards the right. Eventually, we examined the endograft hemodynamics which resulted to exhibit several peculiarities in terms of WSS on the right side of the graft, at the level of its bifurcation. By merging these findings (see Figure 6.1 where the postero-anterior views of WSS distribution at the systolic peak and of the displacements occurred between diastolic and systolic peak are shown) we could attempt to correlate the two phenomena and understand the overall stent-graft behaviour. In fact, the comprehensive rigid translation towards the right could be explained by considering the WSS peak (occurred at the right leg where the two iliac branches bifurcate, see Figure 6.2) as a driving force of the overall endograft motion which do not suddenly deform in a specific point due to its rigid conformation. At the right part of the bifurcation, WSS reaches values significantly higher with respect to the rest of the graft due to the stenosis-like conformation of the

right leg at this level which, accordingly, features a higher velocity field. Therefore, the resulting total change in position during the cardiac cycle could be thought as an effect of the stent-graft geometry which looks like a stenosed vessel. This assumption may be confirmed by: the substantial reduction of the stenosis in PI-T48 device; by the fact that stent-graft displacements occurring during cardiac cycle in PI-T48 are not an apparent rigid translation towards the right; and by the fact that values of displacements are much lower compared to PI-T1 and PI-T12 together with lower values of WSS (see Figure 6.1(c)). These combining events confirm that the right branch stricture present in PI-T1 and PI-T12 strongly impacts the stent-graft behaviour during the cardiac cycle.

Finally, it is interesting to observe a further correlation between WSS and stent-graft displacements at the left leg where the bifurcation of the iliac legs occurs, as the arrows in Figure 6.2 show. In particular high values of both WSS and displacements are located at the inner side of the bifurcation, i.e. the right side of the left leg. This is coherent with: the blood flow impinging this side of the lumen wall because of the left leg curvature; the overall translation of the device towards the right.

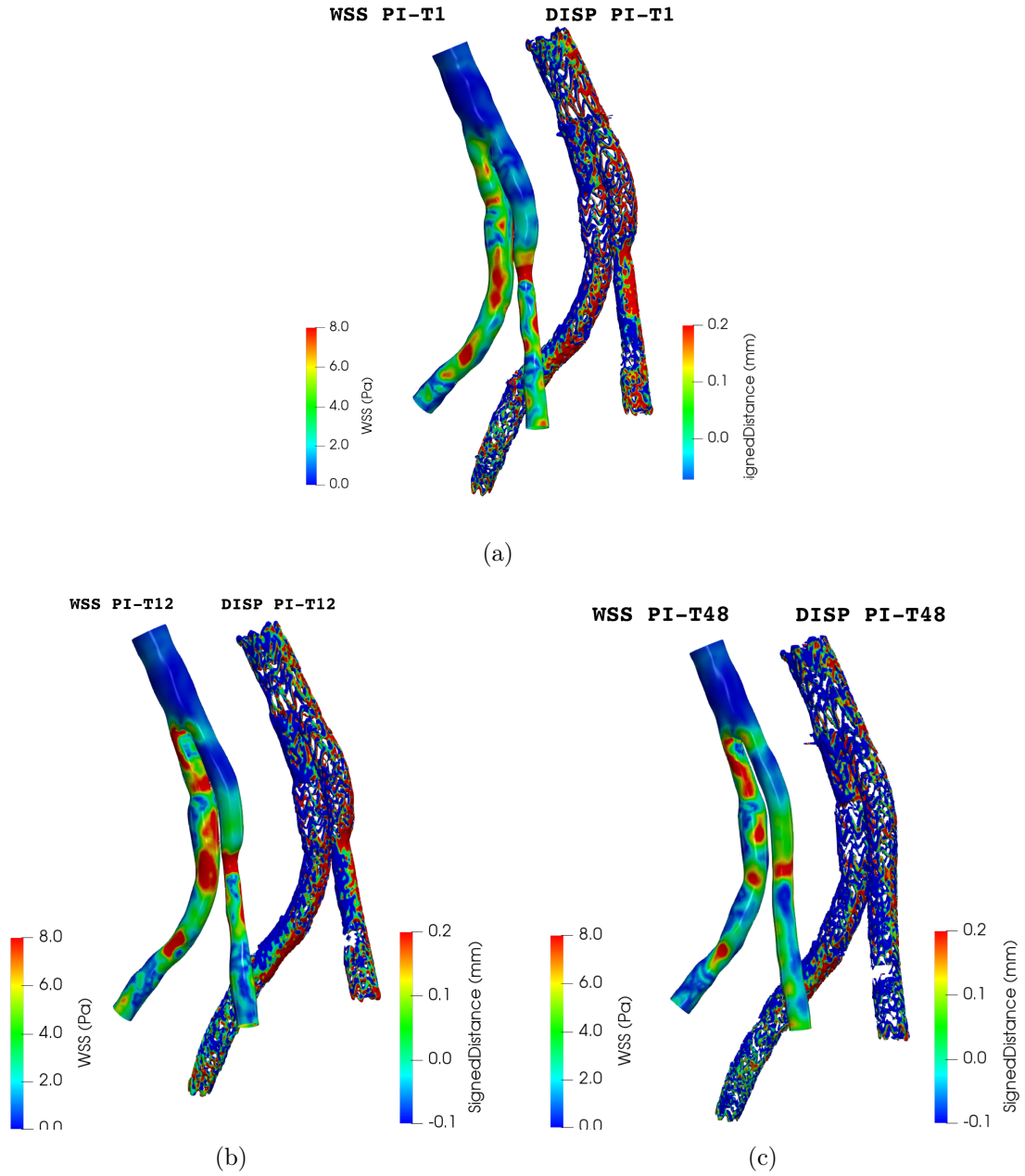


Figure 6.1: Comparison between WSS distribution at the systolic peak (left) and stent-graft displacements between diastole and systole (right): (a) PI-T1; (b) PI-T12; (c) PI-T48.

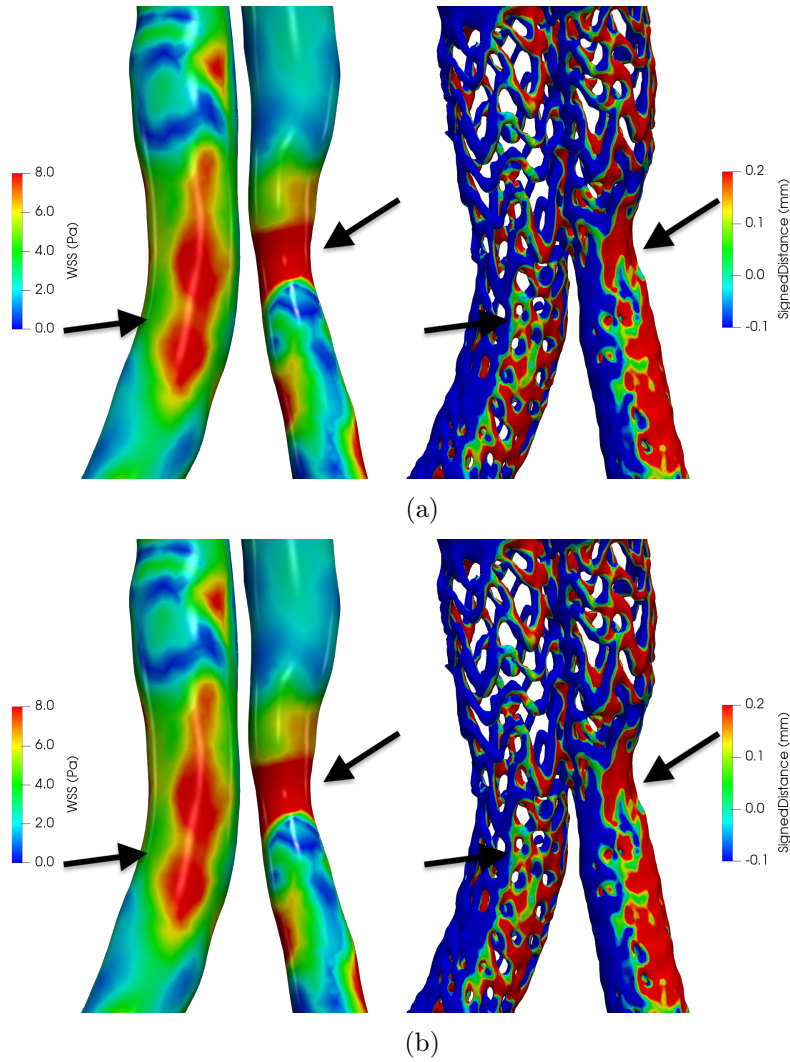


Figure 6.2: Zoomed views on the stenotic right leg of the WSS at systolic peak (left) and stent-graft displacements between diastole and systole (right): (a) PI-T1; (b) PI-T12.

6.1.2 TAWSS-Displacements between follow-ups

In this section we evaluate the possible relationship between the displacements occurred between two follow-ups and the fluid-dynamic results we obtained in Chapter 5. In Chapter 3 we observed that the changes in position of the stent-graft are not comparable to a rigid translation as in the case of displacements within the cardiac cycle. In fact, in this case we do not deal with the changes in position due to the pulsatility of blood flow, instead we examine effects of the hemodynamics on the device after a long time period, i.e. one year between PI-T1 and PI-T12, three year between PI-T12 and PI-T48 for an overall period of four years post-EVAR. For this reason we decided to compare the displacements with TAWSS (Figure 6.3) which takes account of the WSS occurring within the whole cardiac cycle. As we discussed in Chapter 3, the peculiar aspect

we noticed about device motion was the dilation of the stent-graft at the level of the bifurcation of the iliac legs, on the right side. As Figure 6.4 shows, peaks of displacements in this region qualitatively well correlates with the peaks of TAWSS. This findings could explain why the dilation occurs in this portion of the device. It is worthy noting that the stent-graft material is more rigid and much less compliant than the wall of the human abdominal aorta, so that it is not able to exhibit elastic deformation during the blood flow pulsatility, as we observed in the previous section, but it underwent a permanent deformation. The cyclic loading condition, in fact, is the first factor affecting stent lifetime. This fatigue issue is of particular importance since it could lead to a fatal risk of rupture in the long term.

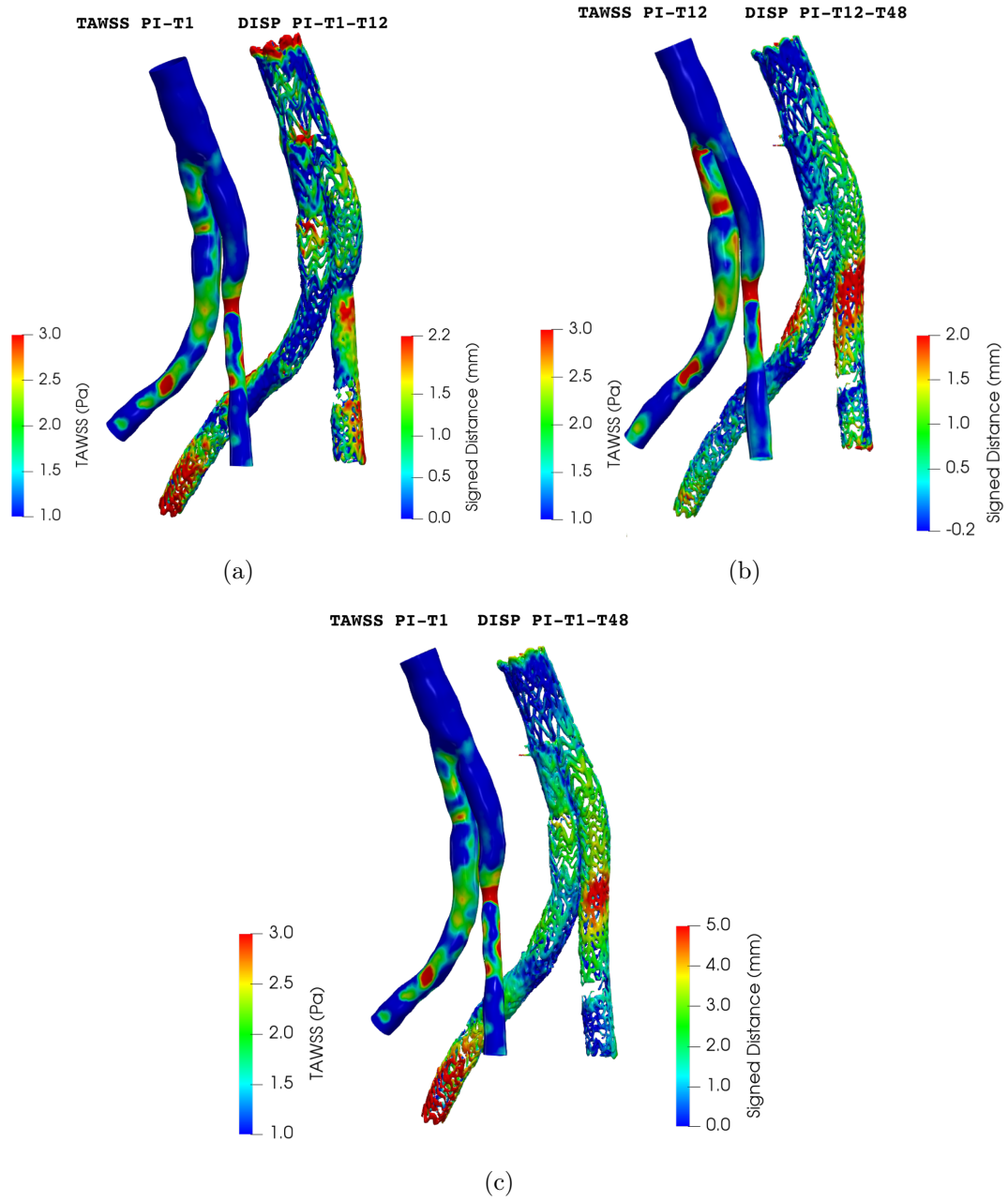


Figure 6.3: Comparison between TAWSS distribution (left) and stent-graft displacements among follow-ups: (a) PI-T1-T12; (b) PI-T12-T48; (c) PI-T1-T48.

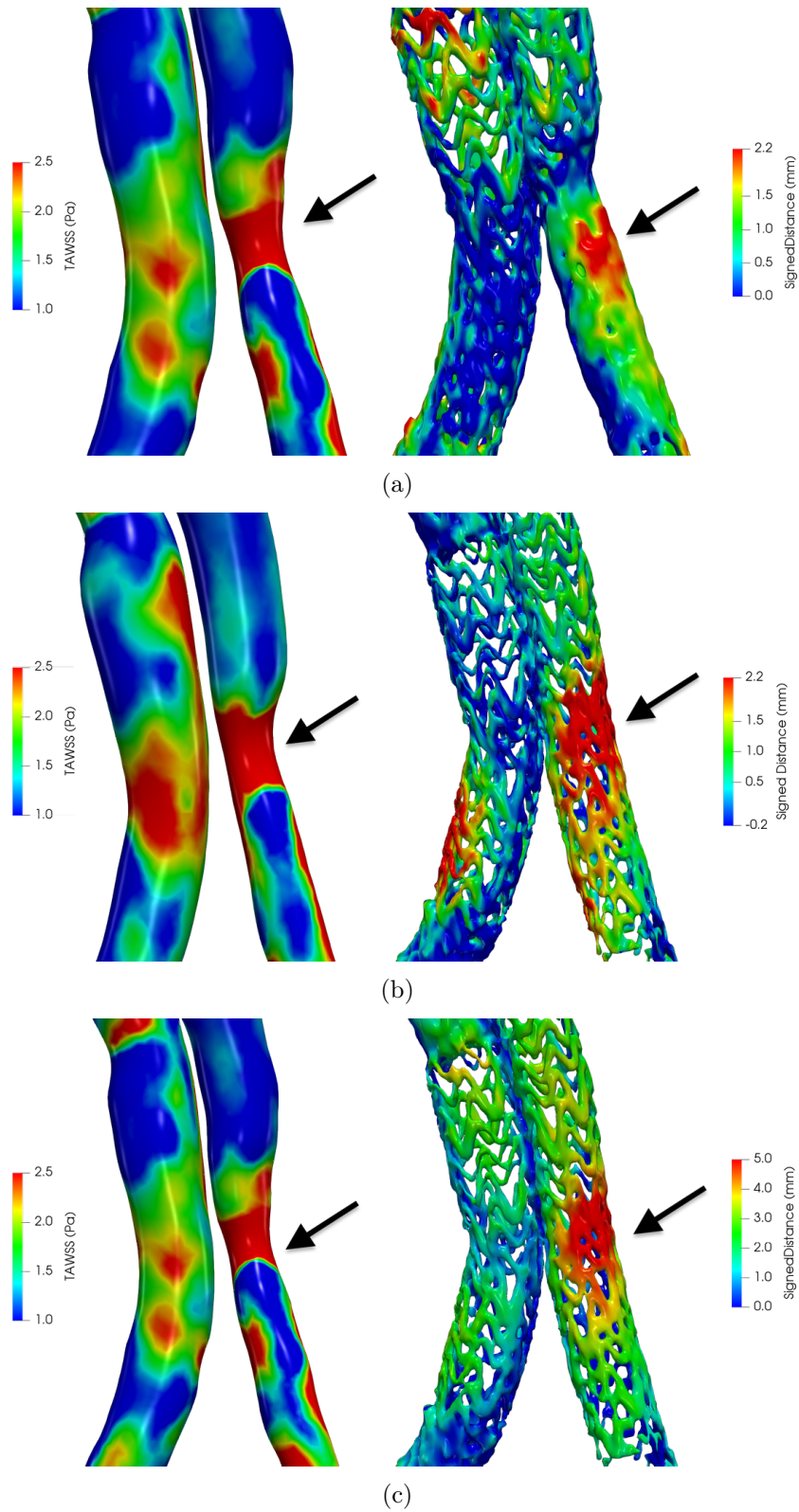


Figure 6.4: Zoomed views on the stenotic right leg of the TAWSS (left) and stent-graft displacements among the follow-ups (right): (a) PI-T1-T12; (b) PI-T12-T48; (c) P-T1-T48.

6.2 Patient III

Patient III represents an interesting clinical case study since his stent-graft underwent a significant eccentric deformation in the central region over the years, as we discussed in Chapter 3. By performing the computational fluid-dynamics simulations on Patient III specific geometry (see Chapter 5) we also examined the blood flow behaviour which resulted to be highly disturbed in the same central portion of the device. In this section we want try to find a reasonable matching between these two phenomena. First of all, it should be noted that the morphology of the device is severely angulated. Therefore, blood initially flows in caudal and slightly anterior direction until it impinges the lumen wall at the bending point, where low velocity is found. The reduction in velocity causes the flow to become unstable, leading to flow separation and recirculation. As Figure 6.5 shows, the expansion of the stent-graft wire is located exactly where such flow disturbances takes place. We observed that TAWSS exhibits lower values with respect to surrounding areas, coherently with the decrease in velocity. In addition, as we mentioned in Chapter 5, blood flow velocity decreases over time from PIII-T1 to PIII-T60 due to the expanding proximal aortic diameter. This make the flow impinging the lumen wall at the angulation later in the cardiac cycle, as the time annotation in Figure 6.5 shows. What we may assume is that, due to this ricirculations, this region may be prone to thrombus formation which gradually grows and makes the stent-graft wires deform and expand. Accordingly with [45], endograft thrombus accumulation is found to be a multifactorial process, resulting from complex interaction of systemic and local hemodynamic factors and geometrical characteristics of the device. Chong et al [46] demonstrated that the stent-graft angulation may produced complex turbulent flow and recirculation patterns within abdominal aortic endografts which leads to the possibility of thrombus formation. We believe that our clinical case could demonstrate this association.

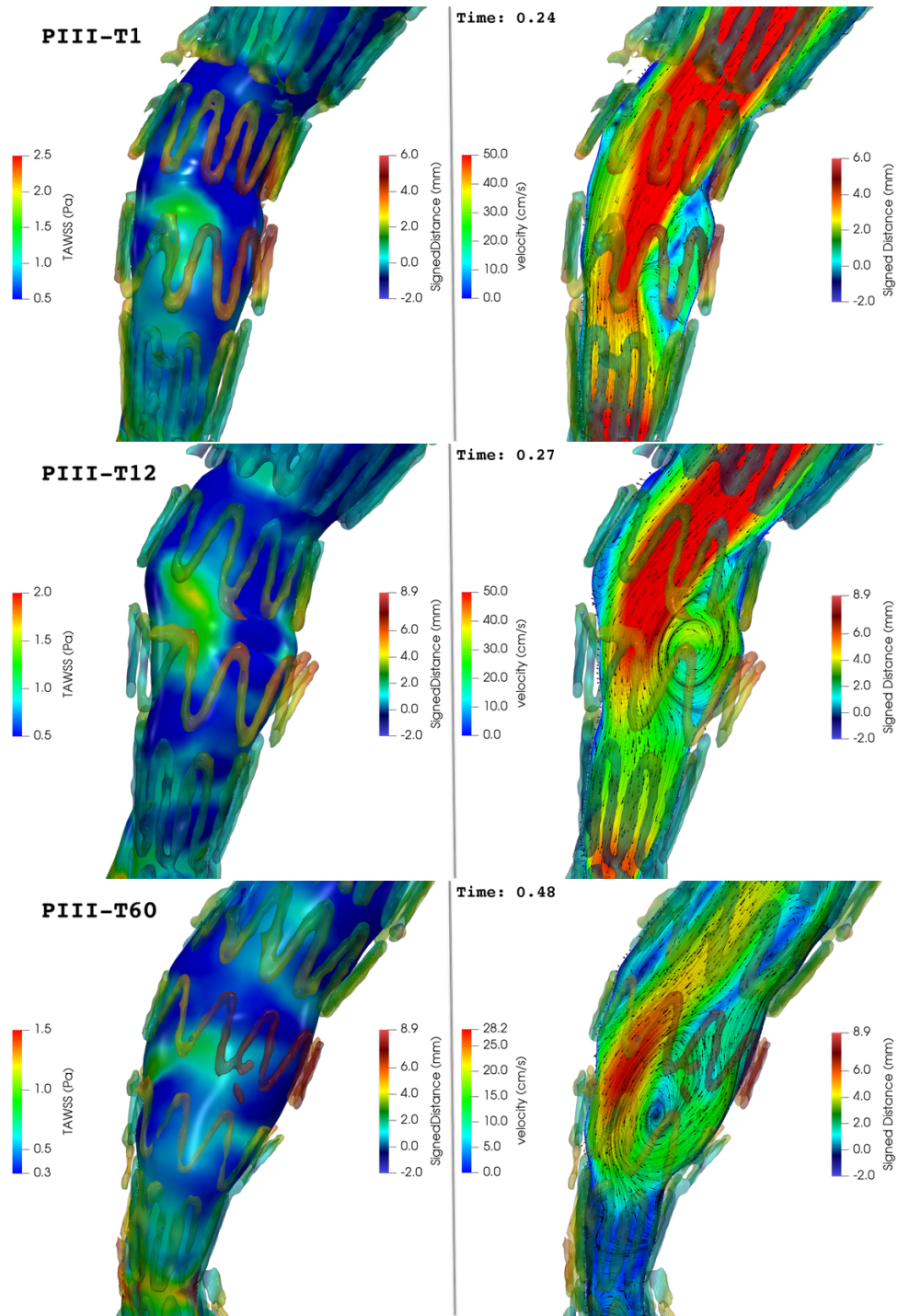


Figure 6.5: Comparison between TAWSS distribution (left) and velocity fields at the impingement point (right): Top: PIII-T1; Centre: PIII-T12; Bottom: PIII-T60. Stent-graft displacements color maps are included: Top: PIII-T1-T12 in PIII-T1 configuration; Centre: PIII-T1-T12 in PIII-T12 configuration; Bottom: PIII-T12-T60 in PIII-T48 configuration.

List of Figures

1.1	Graphic depiction of the aorta.	2
1.2	Segmental division of the aorta: aortic root, ascending aorta, aortic arch, descending thoracic aorta and abdominal aorta.	3
1.3	The anatomy of the human aorta.	3
1.4	Scheme of the branches of the abdominal aorta.	4
1.5	Histologic section of the aorta showing the three layers: tunica intima, media and adventitia.	5
1.6	An example of AAA.	6
1.7	The figure shows a schematic overview of an Intraluminal Thrombus (ILT).	8
1.8	Open aortic aneurysm repair procedure.	9
1.9	Endovascular aneurysm repair procedure.	10
1.10	In the picture the five types of endoleaks are graphically depicted.	11
1.11	In the picture the five types of endoleaks are graphically depicted.	13
2.1	Illustration of how CT works: the scanner consists of an X-ray emitter situated opposite the detectors. As the scan begins, the patients bed slowly moves through the tunnel and stops; the scanner then circles the patient, emitting X-rays, which are beamed through the patient and detected along the circumference of the tunnel; each time the bed moves the scanner circles again. After the area of interest has been scanned, a computer analyses the information received and constructs a transverse image of the body.	18
2.2	Examples of single CT scans of each patient at the first follow-up examination, i.e. T1. Top, left: PI-T1; top, right: PII-T1; bottom: PIII-T1.	20
2.3	Fastmarching initialization of Patient II aneurysm: (a) selection of source seed, (b) selection of target seeds, (c) resulting initial level set.	24
2.4	Colliding fronts initialization of part of Patient II aorta. Two seeds are located in two points along the vessel and level set algorithm reconstructs the surface.	25

2.5	Stent-graft is easy to detect in our CT images since it is characterised by significantly higher values of radiodensity.	26
2.6	Example of 3D geometrical reconstruction of the stent by using threshold level set initialization. (a) Since intensity level of vertebrae is similar to the one of stent-graft's wires, resulting output of level set procedure revealed both structures. (b) If surface connectivity algorithm is used, only stent-graft geometry can be obtained.	27
2.7	Reconstruction of stent-graft of Patient III by using threshold level set initialisation. (a) Artifacts and vertebral bones are segmented in addition to our wanted surface. (b) By applying <code>vmtksurfaceconnectivity</code> command for each of the separated circular wires and <code>vmtksurfaceappend</code> to create a single surface, the whole clean stent-graft is correctly segmented.	27
2.8	By applying ICP algorithm to endograft of Patient I we obtained PI-T1 and PI-T12 graft surfaces translated into PI-T48 coordinate system. . . .	29
2.9	Result of registration procedure applied to stent graft of Patient II in order to translate PII-T12 surface into coordinate system of PII-T60. . .	30
2.10	On the left segmentations PIII-T1 (white), PIII-T12 (blue) and PIII-T60 (red) have different coordinate systems. On the right the result of Iterative Closest Point registration: PIII-T1 surface and PIII-T12 are set, in separately procedures, as source point clouds while PIII-T60 surface is the reference one, so that PIII-T1 and PIII-T12 surfaces are rigidly transformed to have the same coordinate system of PIII-T60.	30
3.1	Comparison between 3D rendering of PI-T1 stent-graft from CT scans in RadiAnt and PI-T1 stent-graft segmentation we performed.	32
3.2	PI-T1 stent-graft segmentation.	32
3.3	PI-T12 segmented stent-graft A detail of the missing wires of the device is shown in the box.	33
3.4	PI-T48 segmented stent-graft. As in case of PI-T12, missing metal structs are zoomed in the box.	34
3.5	Metal artifacts arising from hip prostheses of Patient I. Red arrow denotes region where stent-graft falls in a blind zone so that it can be segmented.	34
3.6	PII-T12 segmented stent-graft. Reconstruction shows a surface not properly similar to a metal stent, as we should expected. Zoomed portions of the surface allow a detailed detection to these artifacts.	35
3.7	PII-T60 segmented stent-graft.	36
3.8	Patient II CT images were characterised by a low resolution.	36
3.9	PIII-T1 segmented stent-graft.	37

3.10	PIII-T12 segmented stent-graft.	38
3.11	PIII-T60 segmented stent-graft.	38
3.12	Nine displacements maps of Patient I endograft. Reference position is the seventh time-step corresponding to diastolic peak. We highlighted that third time-step is the systolic peak. Red color means that current surface is outer with respect to reference one, blue color represents inward surface motion.	40
3.13	Dynamic motion of Patient I stent-graft during one heart beat.	41
3.14	Nine color maps of PI-T48 graft displacements.	41
3.15	Definition of regions where we calculated displacements peaks.	42
3.16	Dotted color map of PII-T12 displacements occurred between systolic and diastolic peak.	43
3.17	Dotted color map of PIII-T1 displacements occurred between systolic and diastolic peak.	44
3.18	Comparison between PIII-T1 surfaces graft before and after remeshing and smoothing procedure. Number of cells increased from 280k to 447k, but color map did not significantly change.	45
3.19	On the left, different views of the Patient I stent-graft showing the displacements occurred between PI-T1 and PI-T12 (antero-posterior and left views at the top, postero-anterior and right views on the bottom). Displacements were computed by using the Signed Surface Distance algorithm of VMTK. We considered PI-T12 as current surface and PI-T1 as reference surface. On the right, PI-T1 (white) and PI-T12 (blue) surfaces are overlapped in order to visualize both the endografts in the two follow-up analysis. Boxes enable a better observation of portions where displacements are higher.	46
3.20	On the left, different views of the displacements occurred between PI-T12 and PI-T48 (antero-posterior and left views at the top, postero-anterior and right views on the bottom). Surface in PI-T48 configuration is shown and colors describe graft movement with respect to PI-T12 surface. On the right, overlapped surfaces, PI-T12 in blue and PI-T48 in red, enable to visualize at one blank both surfaces where color maps revealed peculiarities.	47

3.21	Overall displacements of endograft after four years from its deployment, namely displacements between PI-T1 and PI-T48. On the left, different views of the color mapped stent -graft (antero-posterior and left views at the top, postero-anterior and right views on the bottom), while on the right lateral views of PI-T1 (in white) overlapped over PI-T48 (in red) in order to better visualize the regions where the largest displacements occurred.	48
3.22	Different views of Patient II color mapped device revealing the distance computed from each point of PII-T12 surface to corresponding points of PII-T60. On the right we highlighted the regions where displacements are higher by overlapping PII-T12 surface (blue) and PII-T60 surface (red) in order to easily visualize changes in position.	49
3.23	Stent-graft showing displacements occurred from PIII-T1 to PIII-T12. On the left, colour mapped surfaces, represented from different points of view (postero-anterior and right views at the top, antero-posterior and left views on the bottom), result from Surface Distance algorithm of VMTK, while on the right PIII-T1 (white) and PIII-T12 (blue) surfaces are overlapped in order to visualize both of the endografts in the two follow-up analysis.	51
3.24	Displacements of stent-graft between second and third follow-up, i.e. between PIII-T12 and PIII-T60. On the left, coloured surfaces represent stent-graft in PIII-T60 configurations from different points of view (postero-anterior and right views at the top, antero-posterior and left views on the bottom), and describe displacements computed with respect to PIII-T12 surface. On the right, overlap of both configurations, PIII-T12 in blue and PIII-T60 in red, enables to analyse stent-graft portions which resulted to be critical in the coloured visualization.	52
3.25	Overall displacements stent-graft between PIII-T1 and PIII-T60. Coloured surfaces represent stent-graft in PIII-T60 configurations from different points of view (postero-anterior and right views at the top, antero-posterior and left views on the bottom) and describe displacements computed with respect to PIII-T1 surface.	53
4.1	The shear stress-shear rate relations of Newtonian, dilatant, pseudoplastic and Bingham pseudoplastic fluids.	56

5.1	ITK-Snap software was used to segment stent-graft lumens. Manual segmentation allowed to reconstruct, slice by slice, geometric lumen contours. Here an example concerning Patient III at T1.	70
5.2	Patient I lumen reconstructions. From left to right, lumen from T1, T12 and T48 follow-up images.	71
5.3	Patient III lumen reconstructions. From left to right, lumen from T1, T12 and T60 follow-up images.	72
5.4	Meshes of Patient I at time T1, T12 and T48 from top and bottom view.	73
5.5	Meshes of Patient III at time T1, T12 and T60 from top and bottom view.	74
5.6	Boundaries of the computational domain.	75
5.7	Physiological inlet flow rate $Q(t)$	76
5.8	Physiological inlet velocity waveform.	79
5.9	Velocity field on longitudinal plane from the inlet to the outlets of PI-T1 (first row), PI-T12 (second row) and PI-T48 (third row) at the pre-systolic peak (on the left), systolic peak (in the centre) and mid deceleration point (on the right).	81
5.10	Velocity contour color maps and surface streamlines projected on the cross-sections A, B, C, D, E and F, defined at the bottom, at systolic peak for PI-T1 (first column), PI-T12 (second column) and PI-T48 (third column)..	82
5.11	Velocity contour color maps and surface streamlines projected on the cross-sections A, B, C, D, E and F (defined in Figure 5.10) at mid-deceleratio point for PI-T1 (first column), PI-T12 (second column) and PI-T48 (third column).	83
5.12	On the left, Wall Shear Stress for PI-T1 (first row), PI-T12 (second row) and PI-T48 (third row) at systolic peak. On the right, Time Average Wall Shear Stress.	85
5.13	Velocity field on longitudinal plane from the inlet to the outkets of PIII-T1 (first row), PIII-T12 (second row) and PIII-T60 (third row) at systolic peak (on the left) and mid deceleration point (on the right).	87
5.14	Velocity field on plane from the inlet to the dilation area of PIII-T1 (first row), PIII-T12 (second row) and PIII-T60 (third row) at systolic peak (first column) and mid deceleration point (second column).	88
5.15	On the left, Wall Shear Stress for PIII-T1 (first row), PIII-T12 (second row) and PIII-T60 (third row) at systolic peak (on the left) and mid deceleration point (on the right). On the right, Time Average Wall Shear Stress.	90

6.1	Comparison between WSS distribution at the systolic peak (left) and stent-graft displacements between diastole and systole (right): (a) PI-T1; (b) PI-T12; (c) PI-T48.	93
6.2	Zoomed views on the stenotic right leg of the WSS at systolic peak (left) and stent-graft displacements between diastole and systole (right): (a) PI-T1; (b) PI-T12.	94
6.3	Comparison between TAWSS distribution (left) and stent-graft displacements among follow-ups: (a) PI-T1-T12; (b) PI-T12-T48; (c) PI-T1-T48.	96
6.4	Zoomed views on the stenotic right leg of the TAWSS (left) and stent-graft displacements among the follow-ups (right): (a) PI-T1-T12; (b) PI-T12-T48; (c) P-T1-T48.	97
6.5	Comparison between TAWSS distribution (left) and velocity fields at the impingement point (right): Top: PIII-T1; Centre: PIII-T12; Bottom: PIII-T60. Stent-graft displacements color maps are included: Top: PIII-T1-T12 in PIII-T1 configuration; Centre: PIII-T1-T12 in PIII-T12 configuration; Bottom: PIII-T12-T60 in PIII-T48 configuration.	99

List of Tables

3.1	Measurements of displacements peaks at four stent-graft portions.	42
3.2	Measurements of displacements peaks at four stent-graft portions, defined in Figure 3.19.	47
3.3	Measurements of displacements peaks at three Patient I stent-graft portions for PII-T12-T60 time interval. Location of <i>Top</i> , <i>Bif</i> and <i>Li</i> are visualized in Figure 3.22	49
3.4	Measurements of displacements peaks at three Patient III stent-graft portions for each follow-up, defined in Figure 3.23.	50
5.1	Parameters of the generated meshes: N is the number of tetrahedra; h is a representative value of the space discretization parameter, i.e. of the dimension of the tetrahedra; n stands for the number of boundary layers introduced; τ is the total thickness of the boundary layer; ρ is the thickness ratio between two consecutive boundary layers.	73
5.2	Radius measures of the inlet section of all the meshes and the maximum velocity and Reynold's number reached at the systolic peak, i.e. $t=0.2$ s.	78

Bibliography

- [1] Mrkvicka R Dobrin PB. “Failure of elastin or collagen as possible critical connective tissue alterations underlying aneurysmal dilatation”. In: *Cardiovasc Surg* 2 (1994), pp. 484–88.
- [2] Helena Kuivaniemi, Chris D Platsoucas, and 3rd Tilson M David. “Aortic aneurysms: an immune disease with a strong genetic component”. In: *Circulation* 117.2 (Jan. 2008), pp. 242–252.
- [3] Byron A. Zambrano et al. “Association of Intraluminal Thrombus, Hemodynamic Forces, and Abdominal Aortic Aneurysm Expansion Using Longitudinal CT Images”. In: *Annals of Biomedical Engineering* (2015).
- [4] Marshall W. Webster MD David A.VorpPhD M.L.Raghavan BS. “Mechanical wall stress in abdominal aortic aneurysm: Influence of diameter and asymmetry”. In: *Journal of Vascular Surgery* (1998).
- [5] Clement Kleinstreuer and Zhonghua Li. “Analysis and computer program for rupture-risk prediction of abdominal aortic aneurysms”. In: *BioMedical Engineering OnLine* (2006).
- [6] Powell JT Greenhalgh RM Patel R Sweeting MJ. “Endovascular versus open repair of abdominal aortic aneurysm in 15-years’ follow-up of the UK endovascular aneurysm repair trial 1 (EVAR trial 1): a randomised controlled trial”. In: *Lancet* (2016).
- [7] Abilez OJ Crabtree T Bloch DA Zarins CK Benharash P Lee JT. “Iliac fixation inhibits migration of both suprarenal and infrarenal aortic endografts”. In: *J Vasc Surg* (2007).
- [8] M. Walsha T. McGloughlin L. Morrissa P. Delassusb. “A mathematical model to predict the in vivo pulsatile drag forces acting on bifurcated stent grafts used in endovascular treatment of abdominal aortic aneurysms (AAA)”. In: *Journal of Biomechanics* (2004).

- [9] D.S. Molony et al. “A Computational Study of the Magnitude and Direction of Migration Forces in Patient-specific Abdominal Aortic Aneurysm Stent-Grafts”. In: *European Journal of Vascular and Endovascular Surgery* (2010).
- [10] Richard Nolz et al. “Stent graft Surface Movement after Infrarenal Abdominal Aortic Aneurysm Repair: Comparison of Patients with and without a Type 2 Endoleak”. In: *European journal of vascular and endovascular surgery : the official journal of the European Society for Vascular Surgery* (2015).
- [11] Yeh V Chiou AJ Gorrepati ML Zarins CK Figueroa CA Taylor CA. “Preliminary 3D computational analysis of the relationship between aortic displacement force and direction of endograft movement”. In: *J Vasc Surg* (2010).
- [12] Vasileios Saleptsis Konstantinos Spanos Christos Karathanos and Athanasios D Giannoukas. “Systematic review and meta-analysis of migration after endovascular abdominal aortic aneurysm repair”. In: *Vascular* (2015).
- [13] Stegher S et al Nano G Mazzaccaro D. “Early experience with Ovation endograft system in abdominal aortic disease”. In: *J Cardiothorac Surg* (2014).
- [14] de Donato G Galzerano G Messina G Guerrini S Mazzei MA-Setacci C Setacci F1 Sirignano P. “Two-year-results of Endurant stent-graft in challenging aortic neck morphologies versus standard anatomies”. In: *J Cardiovasc Surg* (2014).
- [15] Desgranges P. Laheij R. J. F. Harris P. L. Becquemin J.-P Fransen G. A. J. “Frequency, Predictive Factors, and Consequences of Stent-Graft Kink Following Endovascular AAA Repair”. In: *Journal of Endovascular Therapy* (2003).
- [16] T. Umscheid and W. J. Stelter. “Time-Related Alterations in Shape, Position, and Structure of Self-Expanding, Modular Aortic Stent-Grafts: A 4-year Single-Center Follow-up”. In: *Journal of Endovascular Therapy* (1999).
- [17] Botti L Ene-Iordache B Remuzzi A Steinman DA Antiga L Piccinelli M. “An image-based modeling framework for patient-specific computational hemodynamics”. In: *Medical Biological Engineering Computing* (2008).
- [18] Brunkwall J Nyman U Malina M Lindblad B. Resch T Ivancev K. “Distal migration of stent-grafts after endovascular repair of abdominal aortic aneurysms”. In: *J Vasc Interv Radiol* (1999).
- [19] Crabtree T Matsumoto AH White RA Fogarty TJ Zarins CK Bloch DA. “Stent graft migration after endovascular aneurysm repair: importance of proximal fixation”. In: *J Vasc Surg* (2003).

- [20] Benharash P Zarins CK Rafii BY Abilez OJ. “Lateral movement of endografts within the aneurysm sac is an indicator of stent-graft instability”. In: *J Endovasc* (2008).
- [21] Youkou Nemoto et al. “Morphological Changes and Device Migration After Stent Graft Insertion — Clinical Application of an Image-Based Modeling System and Analysis With Geometric Parameters —”. In: *Circulation Journal* 82 (2017).
- [22] Anastasios Raptis et al. “Comparison of physiological and post-endovascular aneurysm repair infrarenal blood flow”. In: *Computer Methods in Biomechanics and Biomedical Engineering* (2016).
- [23] Delassus P Morris L Stefanov F McGloughlin T. “Hemodynamic variations due to spiral blood flow through four patient-specific bifurcated stent graft configurations for the treatment of abdominal aortic aneurysms”. In: *Int J Numer Method Biomed Eng* (2012).
- [24] Boehm T Wildermuth S Frauenfelder T Lotfey M. “Computational Fluid Dynamics: Hemodynamic Changes in Abdominal Aortic Aneurysm After Stent-Graft Implantation”. In: *Cardiovascular and Interventional Radiology* (2006).
- [25] B.J.B.M. Wolters et al. “Computational modelling of endoleak after endovascular repair of abdominal aortic aneurysms”. In: *International Journal for Numerical Methods in Biomedical Engineering* 26.3 (2010), pp. 322–335.
- [26] Yueh-hsun Lu et al. “Endoleak Assessment Using Computational Fluid Dynamics and Image Processing Methods in Stented Abdominal Aortic Aneurysm Models”. In: *Computational and Mathematical Methods in Medicine* vol. 2016 (Sept. 2016). DOI: 10.1155/2016/9567294..
- [27] Joseph D. Bronzino. *Biomedical Engineering Handbook*. Springer Science and Business Media, 2000.
- [28] Vincken KL Bartels LW Cornelissen SA van Herwaarden JA Prokop M-Moll FL Verhagen HJ Teutelink A Muhs BE. “Use of dynamic computed tomography to evaluate pre- and postoperative aortic changes in AAA patients undergoing endovascular aneurysm repair”. In: *J Endovasc Ther* (2007).
- [29] Senthilkumaran N and Vaithegi S. “IMAGE SEGMENTATION BY USING THRESHOLDING TECHNIQUES FOR MEDICAL IMAGES”. In: *Computer Science and Engineering: An International Journal* (2016).
- [30] Chakarvarti Sunanda Gupta Charu Gupta S.K. “Image Edge Detection: A Review”. In: *International Journal of Advanced Research in Computer Engineering and Technology* (2013).

- [31] Juan Cardelino Haldo Spont on. “A Review of Classic Edge Detectors”. In: *Image Processing On Line* (2015).
- [32] Luca Antiga, Bogdan Ene-Iordache, and Andrea Remuzzi. “Computational geometry for patient-specific reconstruction and meshing of blood vessels from MR and CT angiography”. In: *IEEE Transactions on Medical Imaging* 22 (2003), pp. 674–684.
- [33] Dominik Fritz Rüdiger Dillmann Thomas Beck Christina Biermann. “Robust model-based centerline extraction of vessels in CTA data”. In: *Medical Imaging* (2009).
- [34] Georg Langs et al. “Learning deformation and structure simultaneously: In situ endograft deformation analysis”. In: *Medical image analysis* 15 (2011), pp. 12–21.
- [35] Almar Klein. “Segmentation and motion estimation of stent grafts in abdominal aortic aneurysms”. PhD thesis. Universiteit Twente, 2011.
- [36] An automatic tool for thoracic aorta segmentation and 3D geometric analysis. “C. Trentin and E. Faggiano and M. Conti and F. Auricchio”. In: *9th International Symposium on Image and Signal Processing and Analysis* (2015).
- [37] Paul Besl and H.D. McKay. “A method for registration of 3-D shapes. IEEE Trans Pattern Anal Mach Intell”. In: *Pattern Analysis and Machine Intelligence, IEEE Transactions on* 14 (Mar. 1992), pp. 239–256.
- [38] Christian Vergara et al. “Large eddy simulations of blood dynamics in abdominal aortic aneurysms.” In: *Medical engineering and physics* 47 (2017), pp. 38–46.
- [39] C.A. Taylor, T.J.R. Hughes, and C.K. Zarins. “Finite element analysis of pulsatile flow in the abdominal aorta under resting and exercise conditions”. In: 33 (Jan. 1996), pp. 81–82.
- [40] A. Quarteroni. *Modellistica numerica per problemi differenziali*. Vol. volume 2. Springer Science Business Media, 2009.
- [41] Gabriel Taubin, Tong Zhang, and Gene Golub. “Optimal surface smoothing as filter design”. In: *Computer Vision — ECCV ’96*. Ed. by Bernard Buxton and Roberto Cipolla. Berlin, Heidelberg: Springer Berlin Heidelberg, 1996, pp. 283–292. ISBN: 978-3-540-49949-7.
- [42] Elena Faggiano, Luca Formaggia, Luca Antiga, et al. “An open-source tool for patient-specific fluid-structure vessel mesh generation”. In: (2013).
- [43] C. Bertoglio and A. Caiazzo. “A tangential regularization method for backow stabilization in hemodynamics”. In: *Journal of Computational Physics* 261:162171 (2014).

- [44] C. Bertoglio and A. Caiazzo. “A Stokes-residual backow stabilization method applied to physiological flows”. In: *Journal of Computational Physics* 313:260278 (2016).
- [45] Nelson F.G. Oliveira et al. “Clinical outcome and morphologic determinants of mural thrombus in abdominal aortic endografts”. In: *Journal of Vascular Surgery* 61.6 (2015), pp. 1391 –1398.
- [46] Chuh K. Chong, Thien V. How, and Peter L. Harris. “Flow Visualization in a Model of a Bifurcated Stent-Graft”. In: *Journal of Endovascular Therapy* 12.4 (2005), pp. 435–445.